

The XENON1T Spin-Independent WIMP Dark Matter Search Results and a Model
to Characterize the Reduction of Electronegative Impurities in its 3.2 Tonne Liquid
Xenon Detector

Zachary Schuyler Greene

Submitted in partial fulfillment of the
requirements for the degree of
Doctor of Philosophy
in the Graduate School of Arts and Sciences

COLUMBIA UNIVERSITY

2018

© 2018
Zachary Schuyler Greene
All rights reserved

ABSTRACT

The XENON1T Spin-Independent WIMP Dark Matter Search Results and a Model to Characterize the Reduction of Electronegative Impurities in its 3.2 Tonne Liquid Xenon Detector

Zachary Schuyler Greene

Over much of the last century evidence has been building for a new component of our universe that interacts primarily through gravitation. Known as cold dark matter, this non-luminous source is predicted to constitute 83% of matter and 26% of mass-energy in the universe. Experiments are currently searching for dark matter via its possible creation in particle colliders, annihilation in high-density regions of the universe, and interactions with Standard Model particles. So far dark matter has eluded direct detection so its composition and properties remain a mystery.

Weakly interacting massive particles (WIMPs) are hypothetical elementary particles that interact on the scale of the weak nuclear force. They naturally satisfy predictions from extensions of the Standard Model and are one of the most favored dark matter candidates. A number of direct detection experiments dedicated to observing their predicted interactions with atomic nuclei have been constructed over the last 25 years.

Liquid xenon dual phase time projection chambers (TPCs) have led the field for spin-independent WIMP searches at $> 10 \text{ GeV}/c^2$ for most of the last decade. XENON1T is the first tonne-scale TPC.

Electronegative impurities in liquid xenon attenuate light and charge, decreasing the signals in our detector. A physics model is presented that describes the behavior of the electronegative impurities over the lifetime of XENON1T.

Contents

| | |
|---|------------|
| Contents | i |
| List of Figures | iii |
| Acknowledgements | xii |
| 1 Purity and the Electron Lifetime | 1 |
| 1.1 Effects of Electronegative Impurities | 1 |
| 1.1.1 Photon Attenuation | 2 |
| 1.1.2 Charge Depletion | 3 |
| 1.2 Measuring the Electron Lifetime | 8 |
| 1.2.1 S ₂ /S ₁ | 8 |
| 1.2.2 α -decays | 9 |
| 1.2.3 ^{83m} Kr | 12 |
| 1.2.4 γ -rays | 14 |
| 1.2.5 ²²² Rn vs. ^{83m} Kr | 18 |
| 1.3 Electron Lifetime Model | 20 |
| 1.3.1 Columbia Demonstrator | 21 |
| 1.3.2 Impurity Removal | 22 |
| 1.3.3 Vaporization and Condensation | 26 |
| 1.3.4 GXe Purification | 28 |
| 1.3.5 Outgassing and Leak | 31 |
| 1.3.5.1 Outgassing Sources | 32 |

| | | |
|---------|---|-----------|
| 1.3.5.2 | Outgassing Model | 36 |
| 1.3.5.3 | Time-Invariant Impurity Sources | 38 |
| 1.3.5.4 | Leak Model | 40 |
| 1.3.6 | Getter Defficiencies | 41 |
| 1.3.7 | Impurity Spikes | 43 |
| 1.3.8 | Hardware Upgrades | 47 |
| 1.3.9 | Field Dependence | 50 |
| 1.4 | Electron Lifetime Fit | 51 |
| 1.4.1 | Statistical Inference | 52 |
| 1.4.2 | Markov Chain Monte Carlo | 52 |
| 1.4.3 | Results | 55 |
| 1.4.4 | ^{83m}Kr Evolution | 56 |
| | Bibliography | 63 |

List of Figures

- 1.1 Absorption coefficient for photons at 1 ppm H₂O vapor (solid red) and O₂ (dashed green). The Xe scintillation spectrum is overlaid for comparison (dashed blue). H₂O impacts Xe scintillation considerably more than O₂ when at the same concentration. Image credit: [233], H₂O data from [234]. 3
- 1.2 Fraction of initial intensity of xenon scintillation with distance for various concentrations of H₂O (left) and O₂ (right). Image credit: [233]. 4
- 1.3 Drift velocity (here defined as W) dependence on reduced electric field E_d/N where N is the number of molecules per volume. Points are from experimental data [236]–[239] and curves are from calculations. 1 Td = 10^{-17} V cm². LXe has a higher drift velocity than GXe at $E_d/N \lesssim 1$ Td (1 Td = 10^{-17} V cm²). Image credit: [240]. 5
- 1.4 Temperature-dependent drift mobility for holes in LXe. Data is shown as empty triangles. A fit using Eq. 1.6 is shown as the solid line. Image credit: [246] (redrawn from [241]). 7
- 1.5 cS1 (left) and α -corrected cS1 (right) dependence on z . The large α -decay S1s deep in the TPC saturate the bottom PMTs, causing an under-corrected cS1, which results in the distortion seen in the left panel. Near the top ($z \gtrsim -5$ cm) a similar effect is observed from top PMT saturation. The distortion is corrected in the right panel where the effect is much less significant. The red and blue boxes highlight the events selected to calculate τ_e . The colors of data markers correspond to S2_b. 11

| | |
|--|----|
| 1.6 Electron lifetime measurements using ^{222}Rn (left) and ^{218}Po (right) from October 29-31, 2017. The red and blue lines correspond to ^{222}Rn and ^{218}Po , respectively, and are drawn in the drift time region that was used for the fit (see text for event selection). They are each drawn in both panels to show the S2_b overlap, highlighting the need for the α -corrected cS1 cut. The pink dashed lines mark the boundaries derived from the preliminary fit outside of which events were not considered for the final fit. The electron lifetime measurements agree within uncertainty. | 12 |
| 1.7 cS1s for $^{83\text{m}}\text{Kr}$ during final Science Run 1 calibration (left). The S1 delay time cut is remarkably efficient at selecting $^{83\text{m}}\text{Kr}$ and rejecting background. S1 delay time cut dependence of events from 500-2000 ns (right). A fit with an exponential gives a half-life of 158 ± 12.6 ns, which is in agreement with the accepted value of 154.4 ns. | 13 |
| 1.8 Electron lifetime measurement using $^{83\text{m}}\text{Kr}$ from January 23-25, 2018. . . | 14 |
| 1.9 cS1 vs. cS2_b for $r_{\text{rec}} < 36.94$ cm, $-6 < z < -85$ cm for dark matter search data from April 1-7, 2017 following the SR1 $^{241}\text{AmBe}$ calibration. $^{129\text{m}}\text{Xe}$ and $^{131\text{m}}\text{Xe}$ photopeaks are fit with a 2-dimensional gaussian to reject other background. The red contours mark the 4σ lines. | 15 |
| 1.10 $^{129\text{m}}\text{Xe}$ and $^{131\text{m}}\text{Xe}$ events following the SR0 $^{241}\text{AmBe}$ calibration. Data is omitted during $^{83\text{m}}\text{Kr}$ and ^{220}Rn calibrations. Fits using $R(t) = R_0 \exp(-t/t_{1/2}) + C$ give half-lives of 8.66 ± 0.26 and 11.51 ± 0.43 days, respectively, which match the known values of 8.88 and 11.93 days. | 16 |
| 1.11 Electron lifetimes for $^{131\text{m}}\text{Xe}$ (left) and $^{129\text{m}}\text{Xe}$ (right) for April 1-7, 2017 (same as in Fig. 1.9). The red lines mark the region of the fit - $70 < t_d < 710 \mu\text{s}$ and $100 < t_d < 710 \mu\text{s}$ for $^{131\text{m}}\text{Xe}$ and $^{129\text{m}}\text{Xe}$, respectively. The change in fit boundary is to remove higher energy events from detector materials that reach deeper inside the LXe, visible at $t_d \lesssim 50 \mu\text{s}$ in the right panel. The electron lifetimes agree with one another. | 16 |

- 1.16 Electron lifetime dependence on flow rate through getter for the Columbia Demonstrator. Measurements are done for 5 (pink circles), 20 (blue squares), 30 (blue triangles), 41 (green triangles), 50 (red squares), and 80 (black circles) slpm. With exception of 5 slpm, the lifetimes increase at roughly the same rate per cycle for the first $\lesssim 7$ cycles. From 0 to 50 slpm an increase in flow produces a higher final electron lifetime. At 80 slpm τ_e drops below that at 50 slpm. An explanation may be that at high speeds impurities cannot be removed as efficiently due to the short time spent in the getter. Image credit: [255] 22
- 1.17 Schematic for purification system from slow control. LXe and GXe enter the purification system and pass through the top or bottom branch. They reunite before returning through the heat exchanger or as pressurized gas to the TPC Bell. QDrives (yellow), flow controls FC201 and FC202 (purple), getters (green), bypass valves (pink) and the HALO monitor (red) are highlighted. The path of xenon during ordinary operations is shown in red. 25
- 1.18 Heater power \dot{Q}_H (red) and purification flow (blue) from May 2-8, 2016. On May 4th circulation is stopped, decreasing the heat load in the GXe. \dot{Q}_H rises to ~ 120 W, so to satisfy Eq. 1.16 $\dot{Q}_{GXe} \sim 140$ W. When purification resumes on May 6th there is a sharp drop in \dot{Q}_H while the heat exchanger and other materials equilibrate before returning to a stable value. 27
- 1.19 \dot{Q}_H over the lifetime of XENON1T. Sudden spikes and sporadic behavior result from compensating for rapid increases or decreases in heat from the GXe. Long-term downward trend is caused by the PTR cooling power decreasing over time. The corrected trend used in the fit is shown. 29

| | |
|---|----|
| 1.24 Periods of getter defficiencies for November 26 - December 5, 2016 (left) and October 25-30, 2017 (right). ^{222}Rn - ^{218}Po combined (green), ^{222}Rn , (yellow triangles), ^{218}Po (turquoise), and ^{212}Bi (red) electron lifetimes are shown. $^{83\text{m}}\text{Kr}$ (shaded orange), ^{220}Rn (purple), and $^{241}\text{AmBe}$ (green) calibrations are highlighted. The cause of the first defficiency in 2016 is not understood, as detector parameters are stable during this period. The getter defficiency in October 2017 is likely caused by an excess of impurities that were released from the ^{220}Rn calibration. Each resulted in a total drop of $\lesssim 10 \mu\text{s}$. The power glitch on November 21, 2016 causes a sudden purity decrease (Sec. 1.3.7). | 42 |
| 1.25 Installation of the third QDrive in the purification system from September 29 - October 5, 2016. Lifetimes are measured with ^{222}Rn - ^{218}Po combined data (green). ^{220}Rn and $^{241}\text{AmBe}$ calibrations are shaded purple and turquoise, respectively. | 48 |
| 1.26 Electron lifetime measurements following the end of SR1. Initial drops in purity are due to a power disruption, blackout, and gate washings. Subsequent changes are caused by upgrades to the purification system. | 48 |
| 1.27 Figure out what schematic this is for. | 49 |
| 1.28 ^{222}Rn concentration before and after the magnetic pump upgrade. A drop from 12.5 ± 0.2 to $6.8 \pm 0.2 \mu\text{Bq kg}^{-1}$ is observed. Preliminary plot. | 49 |
| 1.29 Field-dependent attachment rates for O_2 , N_2O , and SF_6 . Because is analysis uses O_2 to model all impurities the attachment rate will decrease with electric field. Image credit: [175]. | 51 |

| | |
|--|----|
| 1.30 Examples of θ_p using DEMC (left) and DEMC snooker update (right) in two dimensions. Example of normal DEMC proposal (item 3a). The difference between two randomly selected walkers $\theta_{r_1}, \theta_{r_2}$ is used to propose an update to the i^{th} walker using Eq. 1.36 in two dimensions. θ_p and $\theta_{r_1} - \theta_{r_2}$ are at a slight tilt with respect one another due to \mathbf{z} . Example of DEMC snooker update proposal (item 3b). An update is proposed using difference of projections of $\theta_{r_1}, \theta_{r_2}$ along $\theta_{r_3} - \theta_i$ where θ_{r_3} is a third randomly drawn walker using Eq. 1.40. | 55 |
| 1.31 Electron lifetime model and data over the lifetime of XENON1T. | 59 |
| 1.32 Adjustment of the electron lifetime fit to match $^{83\text{m}}\text{Kr}$. The left panel shows the $\Delta\tau_e (\tau_e^{83\text{m}\text{Kr}} - \tau_e^\alpha)$ dependence on $\tau_e^{83\text{m}\text{Kr}}$ where τ_e^α is the electron lifetime of the trend. Values from $^{83\text{m}}\text{Kr}$ measurements are marked in blue and the best-fit trend is shown in orange. The right panel shows the residuals of the left. | 60 |
| 1.33 Combined energy spectrum over z for 0-1500 keV using the α -decay (top) and $^{83\text{m}}\text{Kr}$ (bottom) S2 _b corrections. For the α -corrected spectrum the mono-energetic peaks curve towards higher E deeper in the detector, indicating they are overcorrected. This occurs to an extent with the $^{83\text{m}}\text{Kr}$ -corrected spectrum at higher energy, but can be explained by the effects of an inhomogeneous electric field. Events near the top of the detector may saturate PMTs in the top array. | 61 |

Acknowledgements

First and foremost, I would like to thank my advisor, Elena Aprile, who welcomed me into her research group in 2014. I owe this dissertation and my remarkable research experience over the past four years to your guidance and encouragement. You exemplify scientific excellence and innovation, and are a role model for young academics.

I would like to give a special thanks to Qing Lin, Patrick de Perio, and Fei Gao. You committed your time and energy to helping me grow as a graduate student. So much of what I have learned over the years is thanks to you. I feel fortunate to have had you as mentors.

I would also like to thank postdoctoral fellows and research scientists Guillaume Plante, Marc Weber, Luke Goetzke, Marcello Messina, and Alfio Rizzo. Your patience and encouragement over the years, especially at the beginning, shaped my four years in the group.

I have had a lot of fun working alongside graduate students Matt Anthony, Yun Zhang, Joey Howlett, and Tianyu Zhu. The experiments, analyses, and trips I've shared with you were among the most memorable of my time at Columbia. I am also happy to have had the opportunity to get to know Damon Daw, who worked in our group for a couple of years.

I am grateful to Marcela Stern. You are one of the kindest and most diligent people I know. You made my life easier on so many occasions. It has been such a pleasure knowing you.

I feel extremely fortunate to have gotten to know Jeremy Dodd these last six years. You are both a mentor and friend, and were there for me in times of uncertainty. You

had a remarkable impact on my time at Columbia, and I am forever grateful.

I am especially thankful to my friends and fellow PhD students Felix Clark, Matt Anthony, Laura Havener, Ryne Carbone, Geoff Iwata, and Russell Smith. I feel privileged to have made such long-lasting friends during this experience. Your support during difficult times, both personally and professionally, has been indispensable. I especially want to thank Felix Clark, who was my roommate, along with Rex Brown.

I am eternally grateful to my family, who has supported and believed in me my entire life. My parents, Pam and Brock, give me the confidence and love that motivates me. My brother, Spencer, is the bravest and most inspiring person I know. I also want to thank my aunt, Diana, uncle, Mark, and cousins, Marissa and Tyler for their encouragement. I consider myself very lucky to have such strong relationships with you.

My family has been through some difficult times. Your love and support gave me the courage and confidence to face these challenges. You continue to teach me the importance of kindness, hard work, and *joie de vivre*, and most important of all, family. You have made me who I am. I love you.

To my parents, Pam and Brock, and brother, Spencer

Here I stand because of you

Chapter 1

Purity and the Electron Lifetime

In a noble element dark matter detection experiment the purity of the target mass is an essential consideration and must be consistently measured. The effects of electronegative impurities - which attenuate light and charge - are easily measured through the electron lifetime. However, a reliable model for the evolution of the impurities does not exist to explain and predict the behavior.

This chapter focuses on the effects of impurities (Sec. 1.1), electron lifetime measurements (Sec. 1.2), the derivation of the electron lifetime model (Sec. 1.3), and the results (Sec. 1.4).

1.1 Effects of Electronegative Impurities

Electronegative impurities mainly come from outgassing from detector materials.

Purity usually refers to two distinct but correlated group, though the degree of the correlation can depend on the experiment. The first is background contamination from radioactive elements of other noble elements inside the TPC. For xenon the primary challenges are ^{85}Kr (Sec. ??) and ^{222}Rn (Sec. ??) as they have low-energy decays that can reach our region of interest.

The second type is the density of electronegative impurities such as O_2 or N_2 , which attach to drifting electrons, lowering or even eliminating the S2. This can have the largest impact at low energies since the number of e^- is much fewer. To

1. PURITY AND THE ELECTRON LIFETIME

correct for the expected initial number of electrons we can use the electron lifetime τ_e . Of course, if the entire cloud of electrons is removed by these impurities we cannot apply a correction since we have no knowledge of where in the detector it occurred or the energy deposition. Even if some electrons make it to the surface a low electron lifetime creates more uncertainty when correcting the S2. This chapter is focused electronegative impurities, though its examination necessitates consideration of the radioactive background concentration.

1.1.1 Photon Attenuation

Xe scintillation (178 nm with \sim 14 nm spectral FWHM) is absorbed by a number of electronegative impurities [230], [231]. At concentrations of ppm or higher the fraction of VUV photons that reach the PMTs can be considerably decreased - especially for large detectors where longer travel distances are required. The intensity drop due to photon attenuation is given by

$$I(x) = I_0 e^{-x/\lambda_{\text{att}}} \quad (1.1)$$

where I_0 is initial intensity, x is distance, and λ_{att} is the attenuation length, and $1/\lambda_{\text{att}} = 1/\lambda_{\text{abs}} + 1/\lambda_{\text{scatt}}$ where λ_{abs} and λ_{scatt} are the absorption and scattering lengths, respectively. The absorption length describes loss of photons due to absorption by an element or molecule while the scattering length describes the elastic scattering of photons. For perfectly pure xenon $\lambda_{\text{abs}} \sim \infty$ ([232] found $\lambda_{\text{abs}} > 100$ cm at 90% confidence level).

High levels of impurities, however, can shorten the absorption length. Fig. 1.1 shows the absorption coefficients ($\lambda_{\text{abs}}^{-1}$) for 1 ppm H₂O and O₂ from 130-200 nm. They overlap with shorter wavelengths of the xenon spectrum (included for comparison), meaning light detected by PMTs will have an asymmetric distribution. With a nearly 1-meter tall detector a 1 ppm concentration of H₂O would have at 10% effect or more at $\lesssim 180$ nm.

The relative intensities for different H₂O/Xe and O₂/Xe concentrations from 0-60 cm are shown in Fig. 1.2. At the level of $\mathcal{O}(100)$ ppb of oxygen $I/I_0 > 0.8$

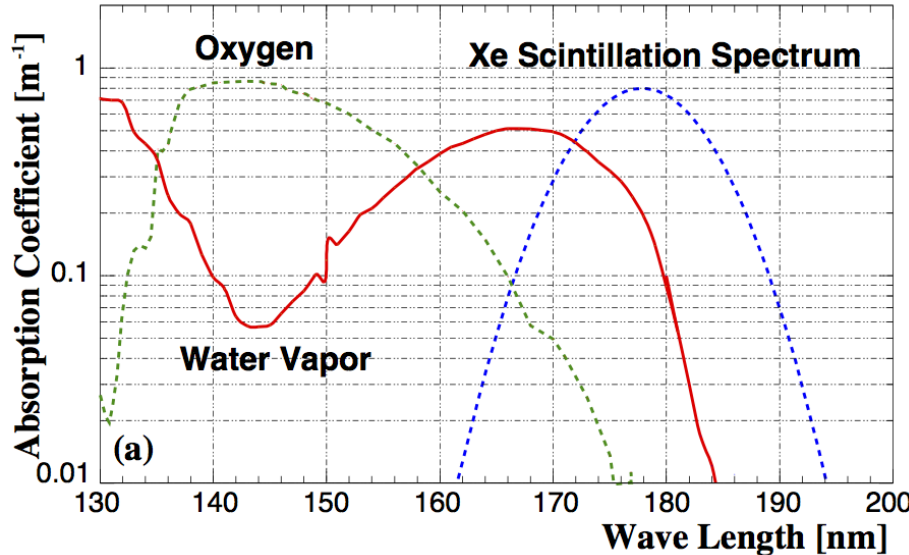


Figure 1.1: Absorption coefficient for photons at 1 ppm H₂O vapor (solid red) and O₂ (dashed green). The Xe scintillation spectrum is overlaid for comparison (dashed blue). H₂O impacts Xe scintillation considerably more than O₂ when at the same concentration. Image credit: [233], H₂O data from [234].

at 60 cm. The effect of water is substantially worse with $I/I_0 < 0.3$, highlighting the need for significant reduction LXe experiments. Even with a LXe purity that is appreciably better than Fig. 1.2 $\lambda_{\text{att}} \approx \lambda_{\text{abs}}$ since the effects of scattering are subdominant with respect to absorption.

Photon attenuation ultimately increases our energy threshold as we are less sensitive to lower energies as few photons are measured.

1.1.2 Charge Depletion

As the electron cloud following a recoil drifts it diffuses longitudinally (in the direction of E_d) and transversely (perpendicular to E_d). The diffusion coefficients D_L and D_T depend on the electric field with $D_T/D_L \sim 10$. The electron spread is $\sigma_{D_T} = \sqrt{D_T t_d}$ where $t_d = d/v_d$ is the drift time and d is the drift distance.

The behavior of electrons can be classified according to their mobility in the limit of $E \rightarrow 0$, μ_0 . When LXe is polarized by electrons its high polarizability ($4.0 \times 10^{-24} \text{ cm}^3$, highest for among noble gases) make it attract e^- and interact with

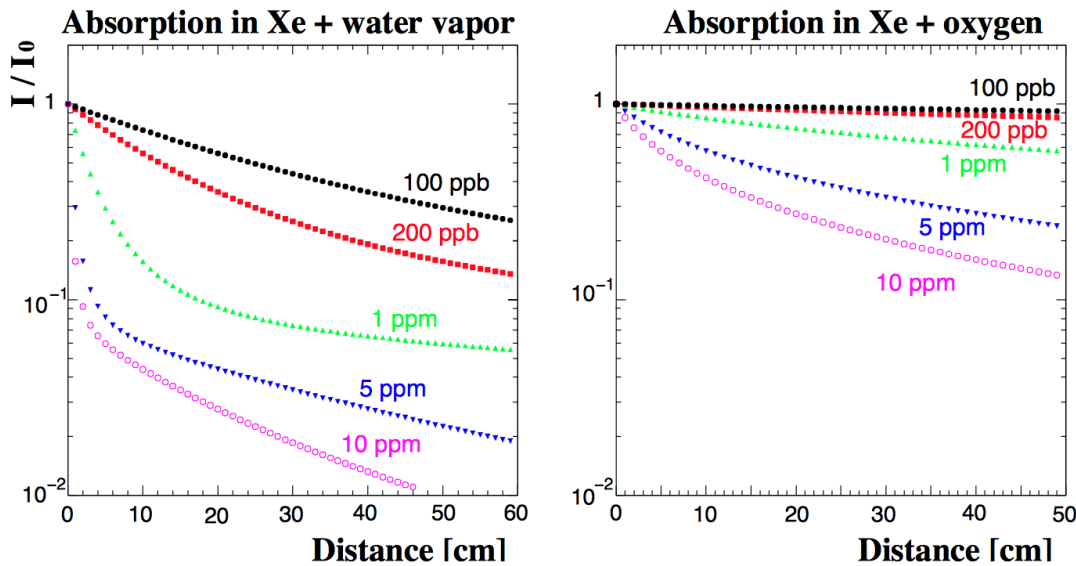


Figure 1.2: Fraction of initial intensity of xenon scintillation with distance for various concentrations of H_2O (left) and O_2 (right). Image credit: [233].

nearby Xe atoms through dipole-dipole interactions. The equilibrium of these two effects determines the potential energy of the ground state of electrons V_0 , which is anti-correlated with μ_0 . For LXe these have been measured to be $V_0 = -0.61 \pm 0.05$ K [235] and $\mu_0 = 2200 \pm 200$ $\text{cm}^2 \text{V}^{-1} \text{s}^{-1}$ [149] at 165 K (in addition μ_0 was found to be 1900 and 2200 $\text{cm}^2 \text{V}^{-1} \text{s}^{-1}$ at 163 K by [149] and [141], respectively). The large electron mobilities indicate the electrons are *quasifree*, and have drift velocities that can exceed even those of GXe, as shown in Fig. 1.3.

Ions exhibit significantly lower mobility than electrons. Their mobilities are parameterized as $\mu \approx \eta^{-\alpha}$ where η is the liquid viscosity and $\alpha = 1\text{-}2$. The diffusion coefficients can be calculated with the Nernst-Einstein equation

$$\frac{eD(E)}{\mu(E)} = \mathcal{F}\langle E \rangle \quad (1.2)$$

where $\mathcal{F} = 0.5\text{-}1$ depends on the electron distribution function (e.g. $\mathcal{F} = 2/3$ for a Maxwellian distribution).

The mobilities for holes, TMSi^+ , O_2^- , ^{226}Th , ^{208}Tl , and Xe_2^+ in LXe are listed in Tab. 1.1. They are $\sim 10^6$ times smaller than the electron mobility.

Hole mobility can be described by the hopping model of charge carrier transport.

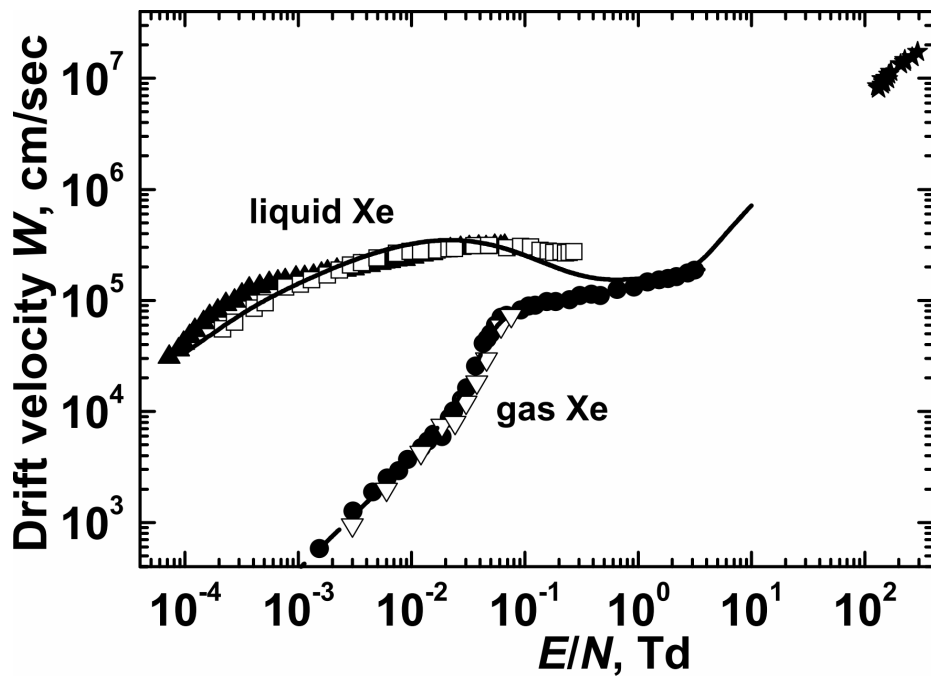


Figure 1.3: Drift velocity (here defined as W) dependence on reduced electric field E_d/N where N is the number of molecules per volume. Points are from experimental data [236]–[239] and curves are from calculations. 1 Td = 10^{-17} V cm 2 . LXe has a higher drift velocity than GXe at $E_d/N \lesssim 1$ Td (1 Td = 10^{-17} V cm 2). Image credit: [240].

| Ion | T [K] | μ [10^{-4} cm 2 V $^{-1}$ s $^{-1}$] | Ref. |
|---------------------|-------|---|-------|
| holes | 161 | 35 | [241] |
| holes | 230 | 46 | [241] |
| TMSi $^+$ | 162 | 2 | [242] |
| TMSi $^+$ | 192 | 3 | [242] |
| O $_2^-$ | 162 | 6 | [242] |
| O $_2^-$ | 192 | 10 | [242] |
| $^{226}\text{Th}^+$ | 162 | 2.4 | [243] |
| $^{208}\text{Tl}^+$ | 163 | 1.33 | [244] |
| Xe $_2^+$ | 184.2 | 2.85 | [245] |
| Xe $_2^+$ | 192.1 | 3.17 | [245] |

Table 1.1: Ion mobilities in LXe. All ions listed are positive with the exception of O $_2^-$. Positive holes have mobilities that are ~ 10 times larger than ions. Summarized data is given in [246].

1. PURITY AND THE ELECTRON LIFETIME

In this temperature-dependent model charge is propagated through jumps between traps yielding

$$\mu = \frac{eb^2}{k_B T} \omega \quad (1.3)$$

where b is the average jump distance and ω is the jumping frequency, parameterized as

$$\omega = P\left(\frac{\omega_0}{2\pi}\right) e^{-E_a/k_B T} \quad (1.4)$$

where ω_0 is the phonon frequency and $P(\omega_0/2\pi)$ is the tunneling probability between adjacent holes with activation energy E_a . Fig. 1.4 shows hole mobility in LXe. The solid curve represents a model that parameterizes Eq. 1.3 as

$$b^3(T) = \sqrt{2M/\rho(T)} \quad (1.5)$$

where M is the atomic mass of xenon and $\rho(T)$ is the temperature-dependent density [241]. It additionally assumes the hole is self-trapped between two rare atoms in a potential well, forming a polaron. It gives a hole mobility of

$$\mu(T) = \frac{eb^2(T)}{k_B} \frac{2\pi}{h} \sqrt{\frac{\pi}{4E_a k_B T}} J_0^2 e^{-2\alpha b(T)} e^{-E_a/k_B T} \quad (1.6)$$

where h is Planck's constant and $J(T) = J_0 e^{-\alpha b(t)}$ is the transfer integral.

As the electron cloud drifts electronegative impurities bond to e^-



where S refers to the impurity (e.g. $e^- + O_2 \rightarrow O_2^-$).

1. Radiative attachment is given by



where XY is some atom or molecule.

2. Dissociative electron attachment (DEA) is when a low-energy electron bonds to a molecule causing it to fracture. The process is given by

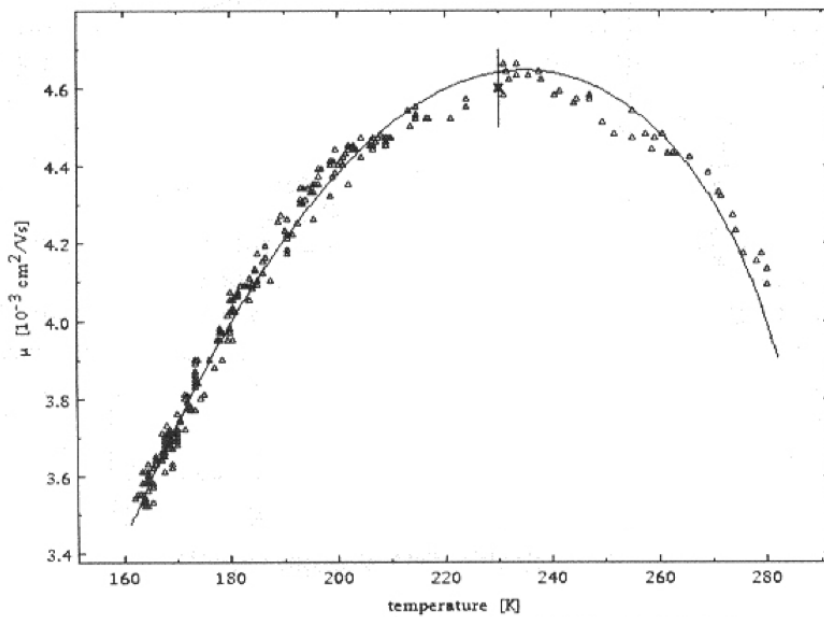
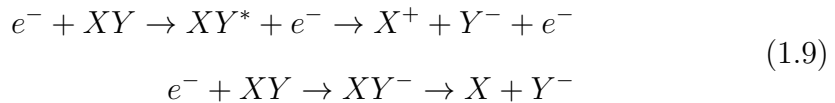
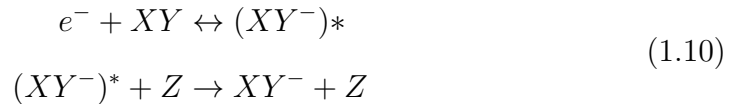


Figure 1.4: Temperature-dependent drift mobility for holes in LXe. Data is shown as empty triangles. A fit using Eq. 1.6 is shown as the solid line. Image credit: [246] (redrawn from [241]).



where molecule XY is separated into components X and Y . O_2 has 5.116 eV dissociation energy (the energy needed to separate the oxygen) and O^- has electron affinity (energy released in forming ion) of 1.461 eV.

3. Three-body attachment proceeds via the two-stage Bloch-Bradbury reaction [247], [248]



where Z is an atom or molecule from the majority gas population. It carries out the bonding energy between the e^- and electronegative XY . Oxygen was studied [249]–[251].

1.2 Measuring the Electron Lifetime

Mono-energetic radioactive decays are used to measure the electron lifetime. For XENON1T electron lifetimes were calculated using elements distributed in the xenon, since external γ -ray sources such as ^{137}Cs and wall events could not reach the FV. This was done primarily with $^{83\text{m}}\text{Kr}$, $^{129\text{m}}\text{Xe}$, $^{131\text{m}}\text{Xe}$, ^{212}Bi , ^{218}Po , and ^{222}Rn (other lines such as the 39.6 keV of ^{129}Xe and 80.2 keV of ^{131}Xe during nuclear recoil calibrations were used but the short half-lives made measurements difficult). Information for each element is listed in Tab. 1.2. An additional method of minimizing the $S_{2\text{b}}$ width of the ^{212}Pb electronic recoil band to address a discrepancy between $^{83\text{m}}\text{Kr}$ and α -decays (Sec. 1.2.5) was tried but the uncertainty was too large to draw any conclusions.

1.2.1 S2/S1

In the period immediately following XENON1T coming online the electron lifetime was ~ 0 since purification began at roughly the same time. The first in-situ calibration was not performed until almost three months later and mono-energetic background decays had not yet been investigated, though ^{222}Rn and ^{218}Po would have had too few events in the top of the detector to be reliable anyways. However, S2/S1 - though not energy-independent - was enough so to give reasonable estimates. It was too early to have official cuts but the ones used were sufficient and based on a history of knowledge of TPC detectors.

S1 (S2) single scatter cuts required that the second largest S1 (S2) be < 0.2 that of the first. The purpose of these cuts was to prevent S1-S2 mismatching: the S1 cut would remove the possibility that we do not observe the S2 of a scatter deep in the TPC, while the S2 eliminated any ambiguity in matching a single S1 with two potential S2s.

To reject noise at least three PMTs were required to observe the S1. This is the same cut that was used in the dark matter analysis. Finally, the fraction of light seen on the top PMT array must fall between 0.2-0.6 for S1s and 0.5-0.9 for S2s.

On a few occasions a ^{137}Cs was placed outside the detector. While the water and

| Isotope | Decay | Energy | $t_{1/2}$ | Section | Notes |
|--------------------|----------|-----------|-----------|------------|-------------------------------|
| ^{83m}Kr | IC | 32.2 keV | 1.83 h | Sec. 1.2.3 | Calibration |
| ^{129m}Xe | γ | 236.2 keV | 8.88 d | Sec. 1.2.4 | Background following NR cal. |
| ^{131m}Xe | γ | 163.9 keV | 11.93 d | Sec. 1.2.4 | Background following NR cal. |
| ^{212}Bi | α | 6.207 MeV | 60.55 m | Sec. 1.2.2 | ^{220}Rn calibration |
| ^{218}Po | α | 6.115 MeV | 3.10 m | Sec. 1.2.2 | Background |
| ^{222}Rn | α | 5.590 MeV | 3.82 d | Sec. 1.2.2 | Background |

Table 1.2: Isotopes used for electron lifetime analysis. Background ^{222}Rn and ^{218}Po α -decays allow continual monitoring but have relatively low statistics. ^{83m}Kr and ^{212}Bi have high statistics but are only available during calibrations. Excited nuclear states ^{131m}Xe and ^{129m}Xe are present in background after nuclear recoil calibrations but their half-lives limit their viability after several weeks.

LXe self-shielding limited the fraction of radiation that made it inside the TPC, there were enough events for measurements. This method was used until early August 2016.

1.2.2 α -decays

The high energy and substantial stopping power (Fig. ??) of α interactions causes a large fraction of electrons to recombine with their parent or nearby Xe^+ atoms. Their S1s are significantly higher than electronic or nuclear recoils so are easily distinguishable. Because they are so recognizable and do not scatter many of the cuts developed for the science run analysis are not necessary (some may not be reliable since they were developed using low-energy electronic recoils). Therefore, just a small number of cuts are used.

Events must have $r_{\text{rec}} < 36.94$ cm. This is in part for consistency with the First Results FV [132], but also because the greatest inhomogeneities in the electric field are expected to be largest at the top, bottom, and sides of the TPC as seen in Fig. ???. Changes in field will produce different light and charge yields (Sec. ??), so the number of photons and electrons would vary according to position. In addition, the impurity attachment rate dependence on field will cause the rate of electron removal to change inside the TPC (Sec. 1.3.9). Finally, the radial cut removes α -decays near the wall that would lose drifting e^- to the PTFE.

The fraction of light seen by the top PMTs from electroluminescence is tightly

1. PURITY AND THE ELECTRON LIFETIME

constrained by stable detector conditions (Eq. ??). The percentage of events that fail this cut is small but it is important to remove any “fake” or gas events (a cut on the S1 fraction seen by the top PMTs will also remove GXe events).

In addition data acquisition quality cuts are used in data selection. The first is the high energy veto, which is triggered by a very large S2. The second is produced by one or more digitizers nearly filling its memory buffer, and is called a busy veto. The third is a busy type check, which removes events that have a busy signal anywhere in the waveform. The final is an end of run check, which disqualifies the last 21 seconds per run (each run is 1 hour). Details for each are given in Sec. ??.

Fig. 1.5 shows cS1 dependence on z for the α -decays of ^{222}Rn ($\sim 5.1 \times 10^4$ PE) and ^{218}Po ($\sim 5.6 \times 10^4$ PE) after these cuts. The large S1s from events deep in the detector saturate PMTs in the bottom array, which leads to under-corrected cS1s as shown in the left panel. To correct for this the data are split into slices in z and fit in cS1 with gaussians. Fits in the region $-40 \lesssim z \lesssim -10$ cm, where saturation is not present, are used to define the correct cS1 distribution, which is extrapolated across the entire length of the TPC. Differences in fit parameters are used to relocate events deeper in the detector into the proper cS1 band. The α -corrected cS1 distribution is shown in the right panel of Fig. 1.5.

Even with the α -corrected cS1s there is saturation near the very bottom of the TPC. The saturation is so great here that events from ^{222}Rn and ^{218}Po cannot be distinguished from one another. This is generally not a problem since it lays outside the fiducial volume. There is also some distortion at $z \gtrsim -5$ cm from events near the LXe surface, whose light is tightly concentrated in the top PMT array.

Selected ^{222}Rn and ^{218}Po events are indicated by red and blue boxes, respectively. Events with $-89 < z < -9$ cm and $4.9 \times 10^4 < \alpha\text{-corrected cS1} < 5.3 \times 10^4$ PE (^{222}Rn) and $5.35 \times 10^4 < \alpha\text{-corrected cS1} < 5.8 \times 10^4$ PE (^{218}Po) are used. The electron lifetimes are calculated independently, which provides a nice cross-check. Because the decay of ^{222}Rn can leave ^{218}Po in a charged state it has slightly fewer (5-10%) events. Electron lifetimes are calculated using 48 hours of data in order to get sufficient statistics.

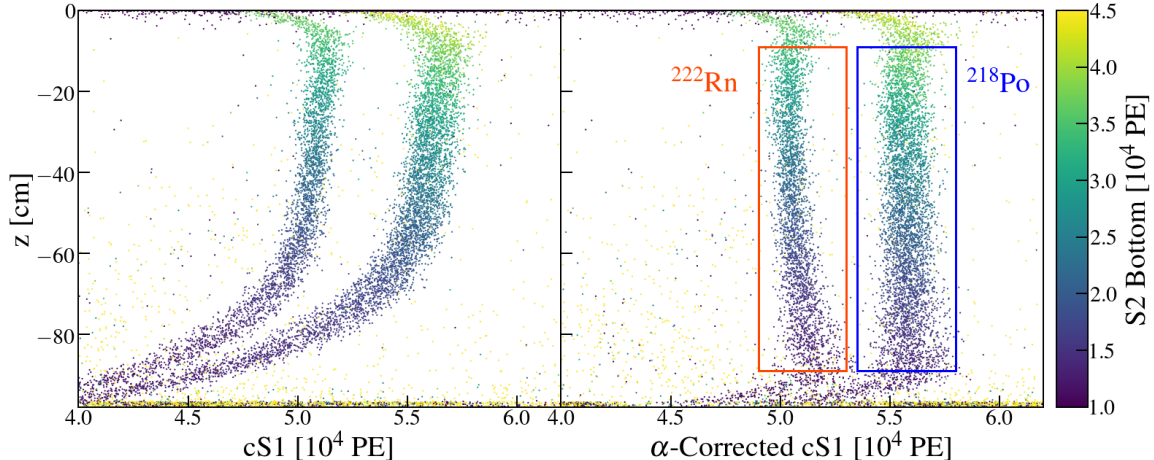


Figure 1.5: cS1 (left) and α -corrected cS1 (right) dependence on z . The large α -decay S1s deep in the TPC saturate the bottom PMTs, causing an under-corrected cS1, which results in the distortion seen in the left panel. Near the top ($z \gtrsim -5$ cm) a similar effect is observed from top PMT saturation. The distortion is corrected in the right panel where the effect is much less significant. The red and blue boxes highlight the events selected to calculate τ_e . The colors of data markers correspond to $S2_b$.

The data is binned in drift time slices Δt_d and an initial fit is performed on the 50th percentiles of the $S2_b$ distributions from each slice. The purpose of this preliminary electron lifetime $\tau_e^{(p)}$ is to remove events that are far from the distribution. The data in each Δt_d slice is binned in cS1 and fit with a gaussian. The means and standard deviations are then fit with an exponential to give the final electron lifetime τ_e . An example can be seen in Fig. 1.6. The pink dashed lines define the boundaries above and below which events were cut using the preliminary fit. ^{222}Rn (left) and ^{218}Po (right) have good agreement.

In Fig. 1.6 the results of both fits are plotted in each panel for comparison. It is clear that without the α -corrected cS1 cut the overlap in $S2_b$ would make it impossible to decouple the ^{222}Rn from ^{218}Po events. Originally a cS1 α -correction map did not exist so ^{222}Rn and ^{218}Po were fit together. This turned out to give slightly lower electron lifetimes than independent fits. Once the α -correction was developed $\tau_{e\text{fit}}$ was re-computed; however, this was not possible for some of the pre-SR0 data that had been deleted.

This method can in principle be used for any α -emitting element distributed

1. PURITY AND THE ELECTRON LIFETIME

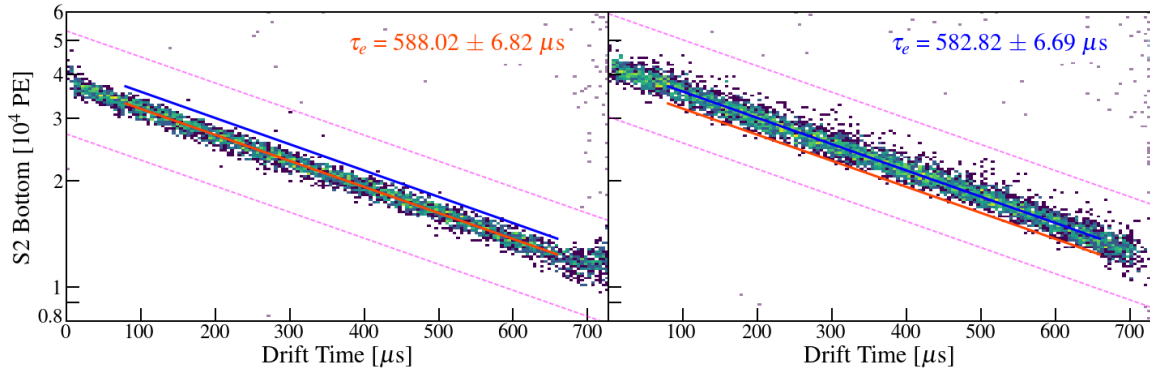


Figure 1.6: Electron lifetime measurements using ^{222}Rn (left) and ^{218}Po (right) from October 29-31, 2017. The red and blue lines correspond to ^{222}Rn and ^{218}Po , respectively, and are drawn in the drift time region that was used for the fit (see text for event selection). They are each drawn in both panels to show the S2_b overlap, highlighting the need for the α -corrected cS1 cut. The pink dashed lines mark the boundaries derived from the preliminary fit outside of which events were not considered for the final fit. The electron lifetime measurements agree within uncertainty.

throughout the FV of the detector and is done so for ^{212}Bi during ^{220}Rn calibrations. Despite ^{220}Rn and ^{216}Po also being α -emitters their short half-lives (55.6 s and 145 ms, respectively) exclude them from consideration. ^{220}Rn and ^{216}Po are also α -emitters and are visible when the source valve is open. However, between the requirement that the source valve be closed and the time it takes to see the rate stabilize and switch to good data taking their short half-lives (55.6 s and 145 ms, respectively) exclude them from observation. Even if this were not the case the α -corrected cS1s of ^{220}Rn (6.405 MeV) and ^{212}Bi (6.207 MeV) overlap, so a joint measurement is likely to lead to a biased τ_e . Due to the enormous number of events there is also some small overlap between ^{220}Rn and ^{216}Po (6.906 MeV).

1.2.3 $^{83\text{m}}\text{Kr}$

^{83}Rb electron capture produces $^{83\text{m}}\text{Kr}$ with a 74.8% branching ratio. The delayed coincidence between the 32.2 and 9.4 keV conversion electrons differentiate $^{83\text{m}}\text{Kr}$ from background. With $t_{1/2} = 154.4$ ns for the 9.4 keV a large fraction of the S1s will overlap. To select events that should always have distinguishable S1s a cut requires the time between S1s Δt_{S1} to be between 500 and 2000 ns ($< 3 \times 10^{-4}\%$ of events

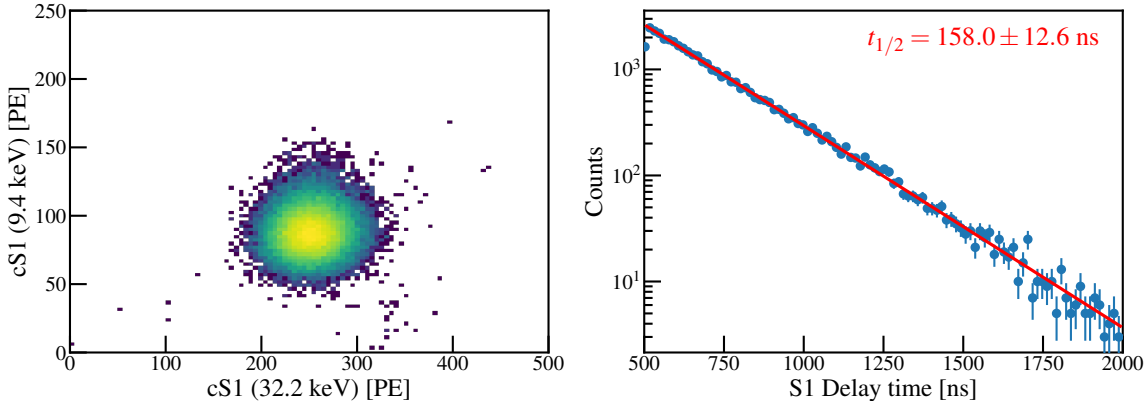


Figure 1.7: cS1s for $^{83\text{m}}\text{Kr}$ during final Science Run 1 calibration (left). The S1 delay time cut is remarkably efficient at selecting $^{83\text{m}}\text{Kr}$ and rejecting background. S1 delay time cut dependence of events from 500-2000 ns (right). A fit with an exponential gives a half-life of 158 ± 12.6 ns, which is in agreement with the accepted value of 154.4 ns.

have $\Delta t_{\text{S}1} > 2000$ ns). This cut eliminates more than 96% of $^{83\text{m}}\text{Kr}$ events, but the remaining events are high enough that τ_e measurements (and other studies, Sec. ??) can be done. To avoid PMT noise coincidence that might mimic the 9.4 keV S1 the number of PMTs that see the low-energy peak must be ≥ 3 . However, to ensure the coincidence is from $^{83\text{m}}\text{Kr}$ events it is also required to be ≤ 30 .

The S1 and S2 from each decay are matched by size of signal. With such a short half-life z cannot change much between decays so τ_e does not have an important role at this stage. Once the position coordinates are calculated from the S2 the S1s are corrected. The left panel of Fig. 1.7 shows the cS1s for both peaks inside the 1 t FV. From the almost entirely empty background it is clear how effective the $\Delta t_{\text{S}1}$ cut is. The number of events vs. $\Delta t_{\text{S}1}$ is shown in the right panel. A fit to an exponential gives $t_{1/2} = 158 \pm 12.6$ ns, which agrees with the accepted value.

The electron lifetime is calculated using the 32.2 keV decay with a procedure similar to that of α -decays Sec. 1.2.2. An preliminary fit is performed using the median $S2_b$ in each drift time slice. However, the high statistics and near-total background removal by the $\Delta t_{\text{S}1}$ cut removes the need to exclude events far from the true $^{83\text{m}}\text{Kr}$ (events farther than pink dashed lines in Fig. 1.6). Each slice in drift time is fit with a gaussian, and an exponential is fit to the results.

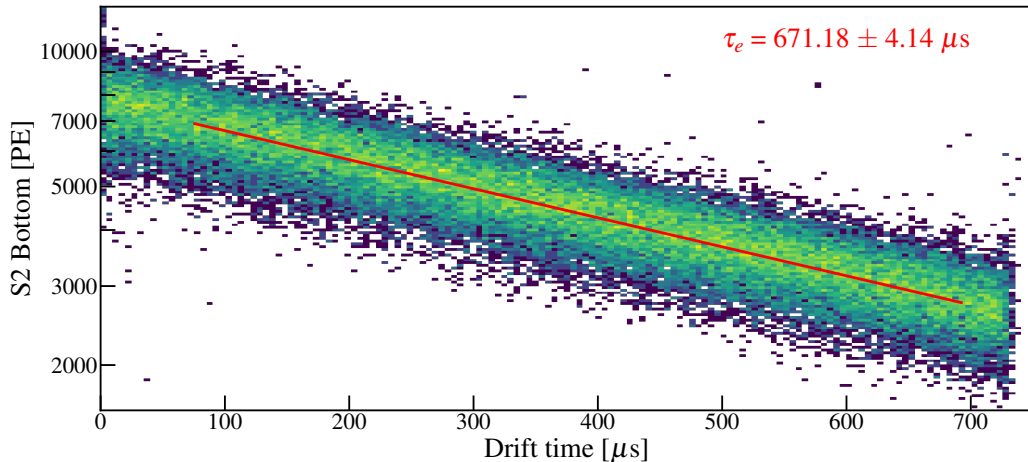


Figure 1.8: Electron lifetime measurement using ^{83m}Kr from January 23-25, 2018.

The large statistics provide τ_e measurements with precision that is only rivaled by ^{212}Bi . Unfortunately, unlike α -decays there are no other electronic recoil τ_e measurements performed regularly to corroborate these results, aside from ^{129m}Xe and ^{131m}Xe following $^{241}\text{AmBe}$ and NG calibrations. Sec. 1.2.5 discusses the reason for the discrepancy between α -decays and ^{83m}Kr and which to use when correcting data.

1.2.4 γ -rays

The full absorption peak of γ -rays make them great candidates for electron lifetime measurements. Unfortunately nearly all γ -rays in the TPC come from elements in detector materials or external sources placed inside the water tank (e.g. ^{137}Cs). However, nuclear recoils can excite ^{129}Xe and ^{131}Xe nuclei to metastable states with half-lives of 8.88 and 11.93 days, respectively. These metastable states serve as an in-situ calibration that are used to measure a number of detector parameters including light and charge yield (Sec. ??), g_1/g_{2b} (Sec. ??), and electron lifetime. While these evaluations can validate electronic recoil measurements from ^{83m}Kr , their short half-lives limit them to the few weeks following an $^{241}\text{AmBe}$ or NG calibration.

Selecting ^{129m}Xe and ^{131m}Xe events is trickier than α or ^{83}Kr . This is in part because they sit on top of an ER background (see Fig. ?? for background energy spectrum), have a relatively low event rate, and do not have properties that allow

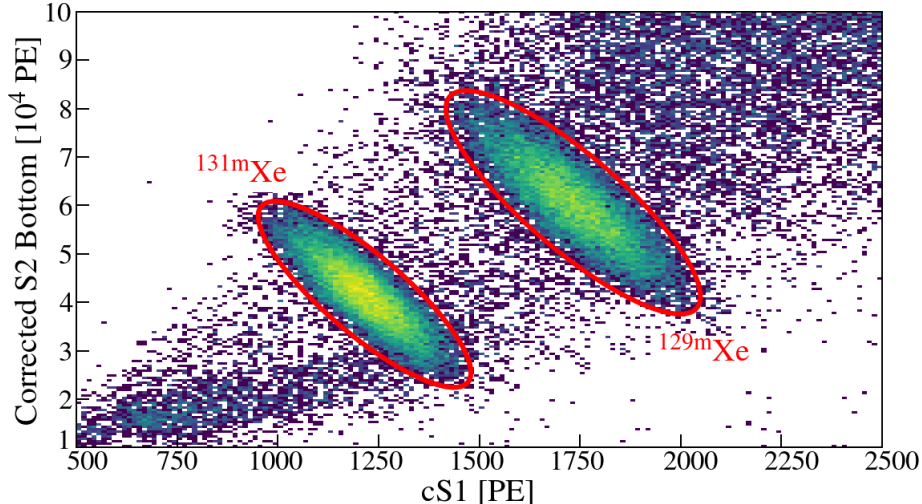


Figure 1.9: cS1 vs. cS2_b for $r_{\text{rec}} < 36.94$ cm, $-6 < z < -85$ cm for dark matter search data from April 1-7, 2017 following the SR1 $^{241}\text{AmBe}$ calibration. $^{129\text{m}}\text{Xe}$ and $^{131\text{m}}\text{Xe}$ photopeaks are fit with a 2-dimensional gaussian to reject other background. The red contours mark the 4σ lines.

a high-percentage cut efficiency (e.g. ^{83}Kr delayed coincidence or high α -decay S1). Instead a number of cuts are required to remove unwanted data before the fit.

To select the 163.9 and 236.2 keV peaks an S2 single scatter cut (same as in nuclear recoil band fitting, Sec. ??) is used to remove much of the underlying background. Additional data quality cuts include ensuring the fraction of the S2 seen by the top PMTs and the width of the S2 fall within expected distributions. For the FV the usual $r_{\text{rec}} < 36.94$ cm is applied but we require $-85 < z < -10$ cm to remove γ -rays of the same energy from materials that penetrate deeper into the detector.

Because cS1 is known (from position reconstruction) fitting the γ peaks is reasonably simple, especially if the electron lifetime can be roughly estimated. In Fig. 1.9 the peaks are surrounded by contours from two-dimension gaussian fits. The y-axis is labeled as cS2_b because for this data τ_e is known within a small uncertainty - however, in general this may not be the case. The final cut removes data outside some number of σ .

To verify the data we've selected is mostly $^{129\text{m}}\text{Xe}$ and $^{131\text{m}}\text{Xe}$ the event rate is fit. Fig. 1.10 shows the number of decays in the two months following the SR0 $^{241}\text{AmBe}$ calibration. The fits give half-lifes that agree with the accepted values. A constant

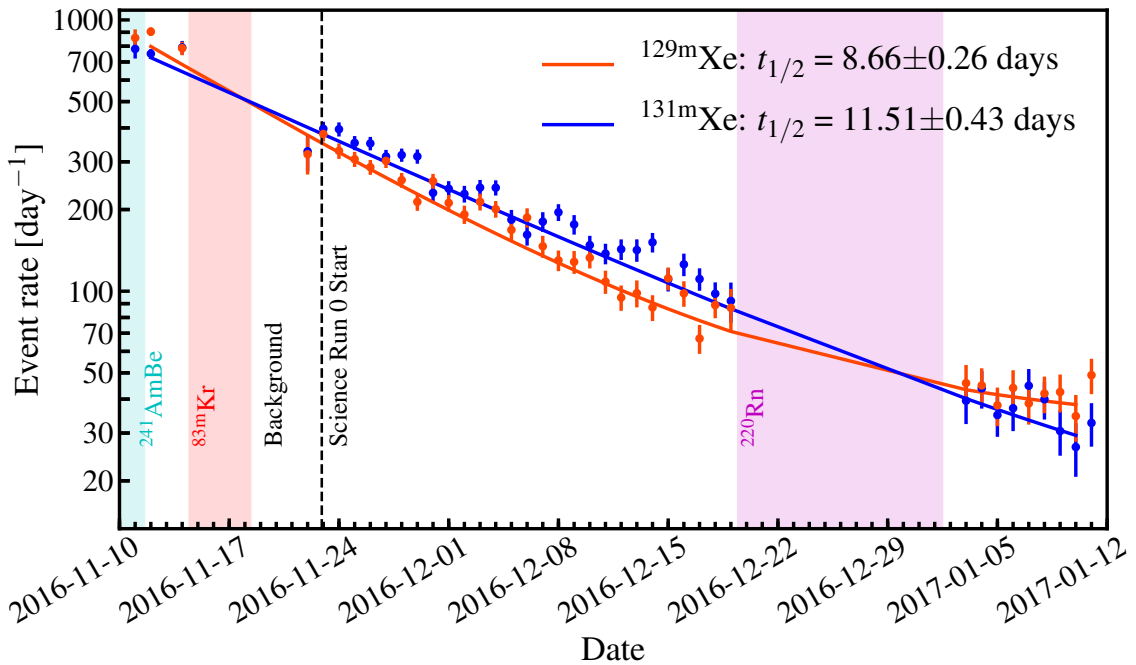


Figure 1.10: ^{129m}Xe and ^{131m}Xe events following the SR0 $^{241}\text{AmBe}$ calibration. Data is omitted during ^{83m}Kr and ^{220}Rn calibrations. Fits using $R(t) = R_0 \exp(-t/t_{1/2}) + C$ give half-lives of 8.66 ± 0.26 and 11.51 ± 0.43 days, respectively, which match the known values of 8.88 and 11.93 days.

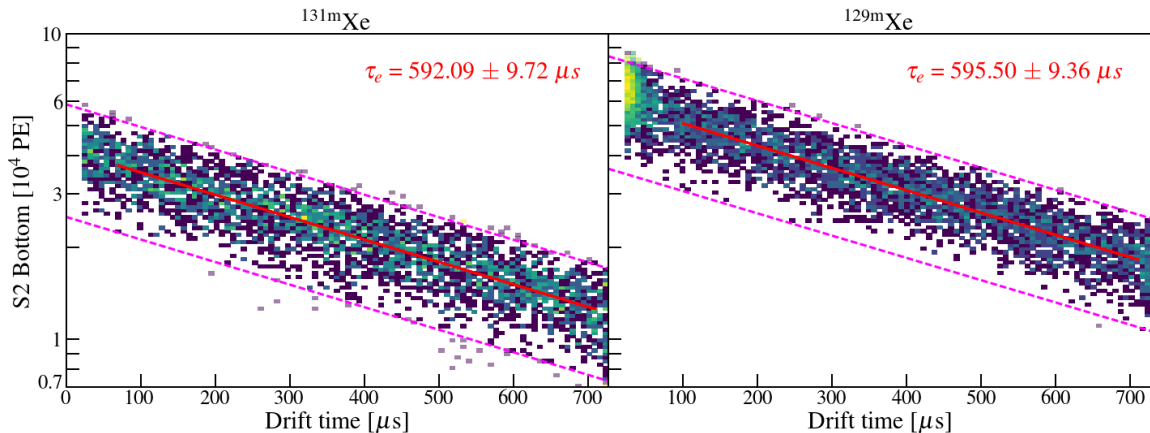


Figure 1.11: Electron lifetimes for ^{131m}Xe (left) and ^{129m}Xe (right) for April 1-7, 2017 (same as in Fig. 1.9). The red lines mark the region of the fit - $70 < t_d < 710 \mu\text{s}$ and $100 < t_d < 710 \mu\text{s}$ for ^{131m}Xe and ^{129m}Xe , respectively. The change in fit boundary is to remove higher energy events from detector materials that reach deeper inside the LXe, visible at $t_d \lesssim 50 \mu\text{s}$ in the right panel. The electron lifetimes agree with one another.

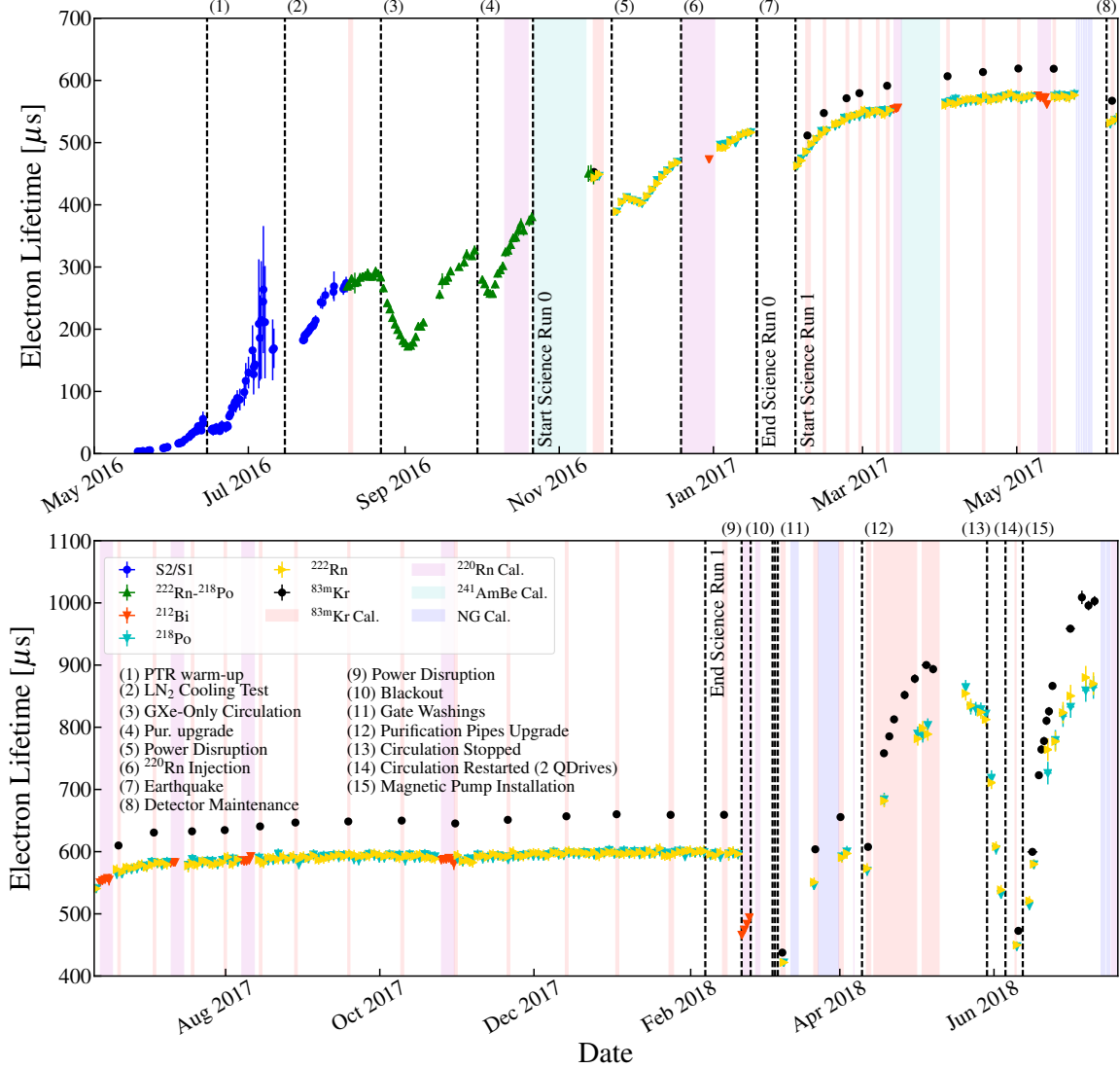


Figure 1.12: Electron lifetime measurements from S2/S1 (blue circles), combined ^{222}Rn - ^{218}Po (green triangles), ^{222}Rn (yellow triangles), ^{220}Rn (red triangles), ^{218}Po (turquoise triangles), and $^{83\text{m}}\text{Kr}$ (black circles). $^{83\text{m}}\text{Kr}$ (orange shaded), ^{220}Rn (red), $^{241}\text{AmBe}$ (green), and NG (blue) calibrations are shown as highlighted regions. Events that disrupt the electron lifetime evolution are marked by numbers at the top of each panel.

is included to account for underlying background.

The procedure to calculate τ_e is the same as in Sec. 1.2.2. The result for the 7 days following the SR1 $^{241}\text{AmBe}$ data in Fig. 1.10 (April 1-7, 2017) is shown in Fig. 1.11.

1.2.5 ^{222}Rn vs. $^{83\text{m}}\text{Kr}$

Fig. 1.12 shows a clear disagreement in electron lifetimes between α -emitters and $^{83\text{m}}\text{Kr}$ at $\tau_e \gtrsim 400 \mu\text{s}$. This presents a challenge in knowing how to properly correct S2_b for signals in the TPC.

The discrepancy is the result of field non-uniformity in the TPC (Fig. ??). Because the change in recombination of α -decays with respect to field differs from that of electronic recoils (Fig. ??) the ratio of the charge yields vary inhomogeneously across the detector. Thus two issues are apparent. The first is bias will be present between any two events of equal energy and type (ER, NR, α) that occur at different fields in the detector. Therefore we cannot expect electron lifetime measurements to accurately report the xenon purity unless field distortion is accounted for. The second is two events whose e^- yield changes with respect to electric field dE/de^- are dissimilar require independent lifetime corrections. LUX also observed a disparity between $^{83\text{m}}\text{Kr}$ and ^{222}Rn lifetimes as well as field inhomogeneity, though the effects were not as stark [252], [253].

In Fig. 1.13 the electron yields for $^{129\text{m}}\text{Xe}$ and ^{222}Rn are shown throughout the TPC according to NEST assuming azimuthal symmetry [254]. The yields are normalized to the region $[-90 \leq z \leq -85 \text{ cm}, r < 36.94 \text{ cm}]$. The 1 t fiducial volume is marked by the black line. Both have decreasing yields in the $-z$ direction, with the deviation for ^{222}Rn being more than twice as large as $^{129\text{m}}\text{Xe}$. This means while τ_e is biased towards smaller values for both elements, the effect is more significant for ^{222}Rn and other α -emitters.

S1 below 10 keV has minimal field dependence because recombination is minimal. Over 10 keV recombination increases.

The z -dependence of electron yields for $^{129\text{m}}\text{Xe}$, $^{131\text{m}}\text{Xe}$, ^{60}Co , ^{208}Tl , and ^{222}Rn is plotted in Fig. 1.14 (averaged over $r < 36.94 \text{ cm}$). The NEST results are normalized to the same region as Fig. 1.13. ^{60}Co and ^{208}Tl (1173.2 and 2614.5 keV, respectively) are shown for comparison with $^{131\text{m}}\text{Xe}$. The difference in relative yields is small - though because in reality the distribution of these detector material-driven events

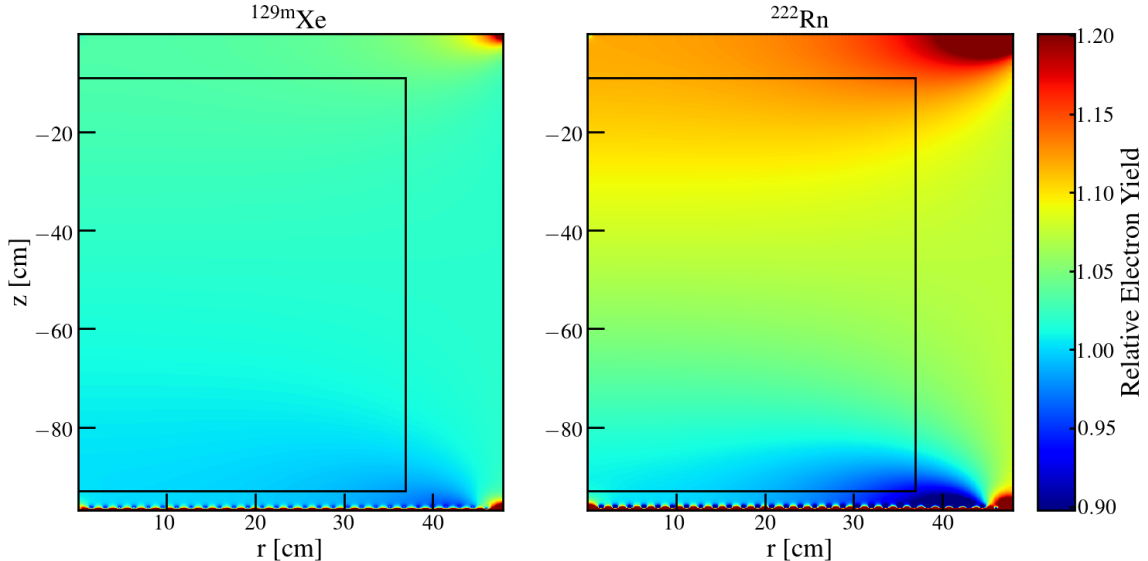


Figure 1.13: Relative electron yield with respect to $[-90 \leq z \leq -85 \text{ cm}, r < 36.94 \text{ cm}]$ for $^{129\text{m}}\text{Xe}$ (left) and ^{222}Rn (right) for $V_c = 8 \text{ kV}$ ($\sim 80 \text{ V cm}^{-1}$) inside the 1T FV (black line). A decline in yield in the $-z$ direction leads to the incorrect observation that the electron lifetime is lower than its true value. The imbalance between the top and bottom of the TPC is $\gtrsim 2\times$ larger for ^{222}Rn , causing its τ_e to appear lower than its γ counterparts.

is more condensed at larger r where there is moderately more z -dependent variation they may be higher. Nonetheless, in either case this would explain the inconsistencies at higher energies in the combined energy spectrum (Fig. ??). The effect of ^{222}Rn is more substantial and demonstrates that calculations of τ_e - which depend on slices in z - suffer from greater bias as a result of change in recombination with respect to field. The higher sensitivity of α -decays in part explains the lower measured lifetime. A separate field-dependent effect is discussed in Sec. 1.3.9.

We expect nuclear recoils to have a different bias than electronic or α -decays. In the dark matter analysis all science run and calibration data were corrected using the $^{83\text{m}}\text{Kr}$ electron lifetime. Nuclear recoil cS2_b were then incorrect and had some bias with respect to ER. However, the disparity between NR and ER should be much smaller than α so we can expect this effect to be small if not negligible.

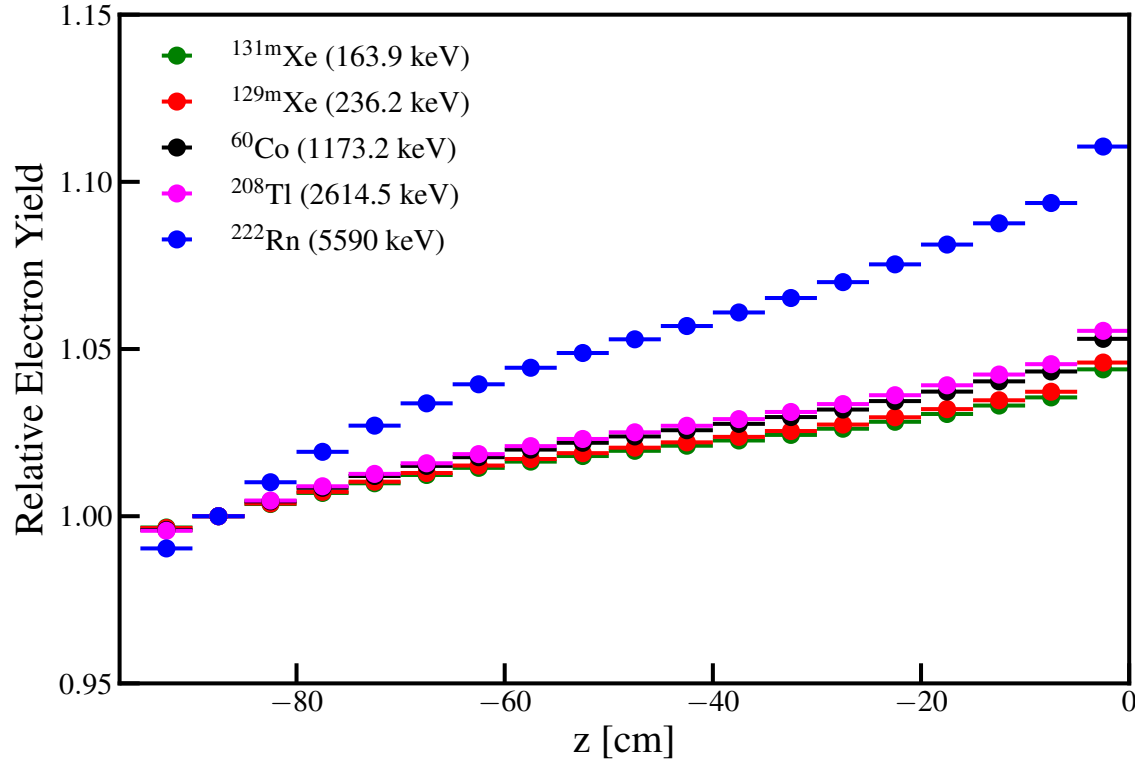


Figure 1.14: Relative electron yield dependence on z with respect to the region $-90 \leq z \leq -85$ cm and $r < 36.94$ cm at $V_c = 8$ kV (~ 80 V cm $^{-1}$) using NEST [254]. Internal γ sources $^{131\text{m}}\text{Xe}$ (green) and $^{129\text{m}}\text{Xe}$ (red) are shown, with higher energies ^{60}Co (black) and ^{208}Tl (pink) plotted for comparison. Their relative light yields vary by $\sim 5\%$, with the higher-energy lines having only $\sim 1\%$ greater difference than $^{131\text{m}}\text{Xe}$ and $^{129\text{m}}\text{Xe}$. ^{222}Rn (blue) changes by $> 10\%$. The disproportionate growth demonstrates the ratio between α and γ electron yields is largest at the top of the detector, causing the fewer e^- from deep α -decays to mimic a smaller τ_e . $^{83\text{m}}\text{Kr}$ cannot be compared as the NEST version is only for high-energy.

1.3 Electron Lifetime Model

To construct the electron lifetime model a number of factors were considered. The model was fit to the ^{222}Rn α -emissions because they could continually monitor the electron lifetime. The best-fit trend was then scaled to match the $^{83\text{m}}\text{Kr}$ data using a “scaling function” and applied to science data to account for the discrepancy between α -decays and $^{83\text{m}}\text{Kr}$ (Sec. 1.2.5).

The model tracks the impurity concentration in LXe (I_L) and GXe (I_G) - the latter of which is necessary because of the exchange of atoms and molecules through

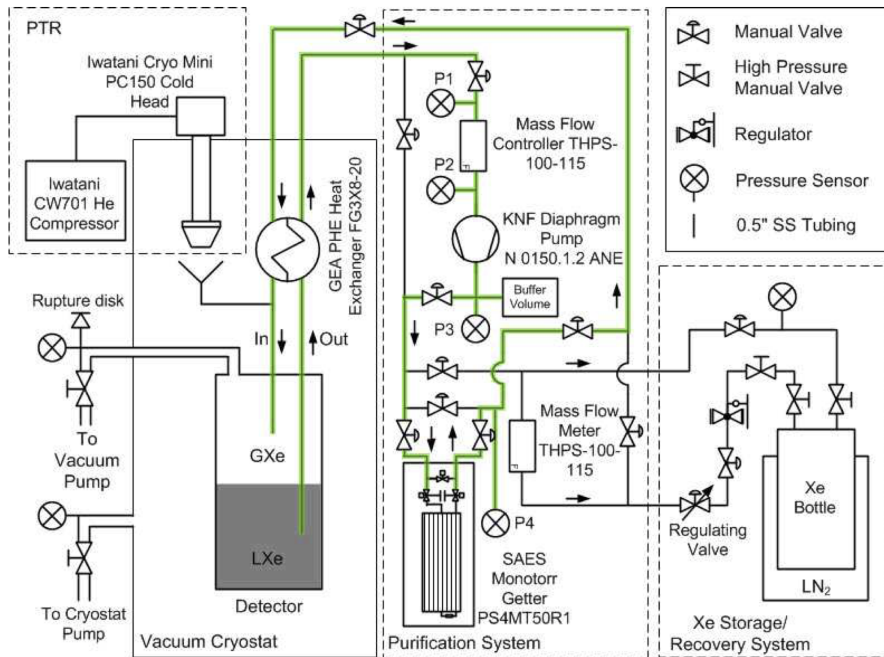


Figure 1.15: Schematic of the Columbia Demonstrator in its initial state. The connection from the GXe to the getter was not yet installed at the time of publication (Sec. 1.3.4). The path of xenon to and from the getter is marked in green. Image credit: [191].

vaporization and condensation (Sec. 1.3.3).

1.3.1 Columbia Demonstrator

To address new challenges in upgrading to a ton-scale detector a prototype was constructed at Columbia. While much smaller in total volume (~ 26 kg total, ~ 4 kg active volume) one of the goals was to assess the feasibility of a 1 meter drift length, which required a significant improvement in xenon purification compared to the ~ 5 slpm of XENON100 [189].

Fig. 1.15 shows a schematic of the Demonstrator. LXe passes through the heat exchanger on its way to the getter and again upon its return as GXe. The getter is a SAES PS4-MT50-R-1, the same model that was chosen for XENON1T. A KNF diaphragm pump, common among LXe experiments, was initially set up and planned for XENON1T but was eventually replaced by a QDrive (Sec. ??). Pipes for GXe circulation were not installed until later so they are not shown.

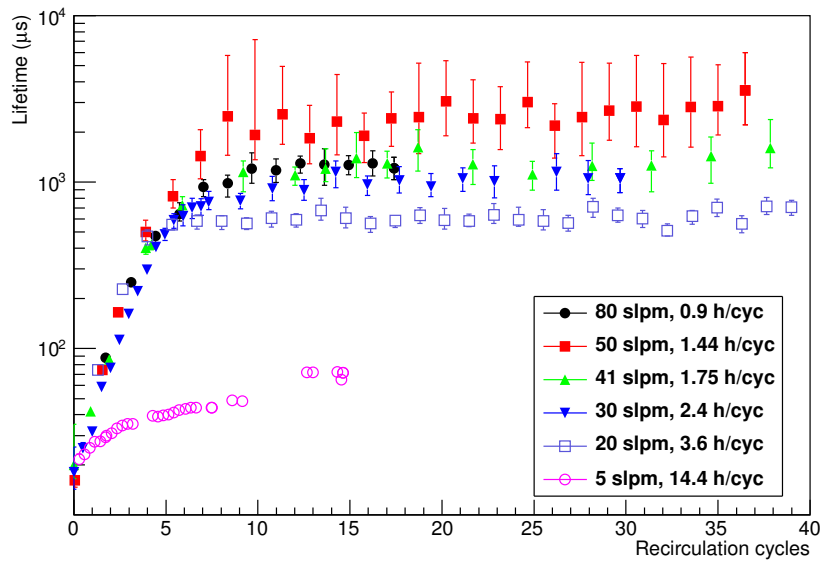


Figure 1.16: Electron lifetime dependence on flow rate through getter for the Columbia Demonstrator. Measurements are done for 5 (pink circles), 20 (blue squares), 30 (blue triangles), 41 (green triangles), 50 (red squares), and 80 (black circles) slpm. With exception of 5 slpm, the lifetimes increase at roughly the same rate per cycle for the first $\lesssim 7$ cycles. From 0 to 50 slpm an increase in flow produces a higher final electron lifetime. At 80 slpm τ_e drops below that at 50 slpm. An explanation may be that at high speeds impurities cannot be removed as efficiently due to the short time spent in the getter. Image credit: [255].

1.3.2 Impurity Removal

Impurities are removed in the purification system (Sec. ??) by two SAES PS4-MT50-R getters. They operate between 5-100 slpm and uses heated zirconium (400°C nominal operating temperature) to form irreversible chemical bonds with O₂, CO, CO₂, H₂O, H₂, N₂, and CH₄, and is capable of achieving levels of < 1 ppb.

Fig. 1.16 shows electron lifetimes using flow speeds of 5-80 slpm in the Demonstrator. For flows larger of 20 slpm and greater the rate of increase per cycle is approximately the same in the beginning (the rate with respect to time depends on the circulation speed). This indicates the influx of new impurities per time is small compared to the rate of removal by the getter, except for in the 5 slpm case. For 20-50 slpm the final value for τ_e increases with flow speed - however, it drops at 80 slpm. This is thought to result from gas passing through the getter too quickly to

remove the impurities completely.

For XENON1T the two getters cleaned a combined flow of $\lesssim 50$ slpm until after SR1. This was only half of the design value and was largely the result of the 1/2" outer diameter pipes connecting the cryogenic system to the purification system producing higher than expected resistance. A series of upgrades were performed in April-June 2018 that increased flows to ~ 80 slpm (Sec. 1.3.8). Because in both cases the flow through each getter never exceeded 50 slpm the electron lifetime model assumes 100% of contaminants are absorbed by the zirconium, though we cannot know if this is truly the case. However, including a variable in the model to reflect a portion of impurities returned to the detector would be equally problematic because Fig. 1.16 suggests any inefficiency is flow-dependent. A more systematic study is needed to characterize the relationship before it can be reliably included. The HALO monitor (Sec. ??) might be able to provide some insight if it were usable during normal operating conditions, since it measures the H₂O concentration of purified xenon. The low circulation over the course of the experiment makes 100% getter efficiency a reasonable estimate.

The rates of impurity removal by the purification system are

$$M_G \frac{dI_G}{dt}^{(\text{pur})} = -\rho_{\text{GXe}} F_G I_G \quad (1.11\text{a})$$

$$M_L \frac{dI_L}{dt}^{(\text{pur})} = -\rho_{\text{GXe}} F_L I_L \quad (1.11\text{b})$$

where $\rho_{\text{GXe}} = 5.984 \text{ g l}^{-1}$ is the density of GXe. F_G and f_L are the flows of the gas and liquid, and are included by using their values stored in the slow control system (Sec. ??). Using the slow control system to automatically integrate these time-varying nuisance parameters into the model is incredibly advantageous over manually assigning the flow.

The schematic of the purification slow control system is shown in Fig. 1.17. While a large number of parameters are monitored only a small fraction need to be included. The three flow control valves (FCVs) that independently regulate GXe flow from the cryogenics system to purification (Sec. 1.3.4) are not shown but precede the “From Cryostat GXe” marker. LXe from the cryostat that passes through the heat exchanger

| Parameter | Function | Color | Comments |
|------------|-----------------------------------|--------|------------------------------|
| CRY_FCV101 | GXe flow control (cables) | — | Precedes “From Cryostat GXe” |
| CRY_FCV102 | GXe flow control (mid-cryostat) | — | Precedes “From Cryostat GXe” |
| CRY_FCV103 | GXe flow control (cooling towers) | — | Precedes “From Cryostat GXe” |
| PUR_FC201 | Flow control (bottom loop) | purple | |
| PUR_FC202 | Flow control (top loop) | purple | |
| PUR_FV217 | Valve (bottom loop) | pink | Bypass Getter 201 |
| PUR_FV224 | Valve (top loop) | pink | Bypass Getter 202 |

Table 1.3: Parameters queried from the slow control system to calculate F_G and F_L . Those in Fig. 1.17 are highlighted in the color listed.

(HE) and heater is labeled “From Cryostat HE”. Returning GXe is sent to the TPC Bell (“GXe to TPC Bell”) through flow control valve FCV104 to maintain cryostat pressure or is liquified in the HE (“To Cryostat HE”) before entering the bottom of the TPC (xenon that does not condense returns to the GXe in the cryogenic system). FCV104 is not necessary to monitor since returning xenon is modeled as 100% pure. The flux through the system is measured with flow controllers FC201 and FC202 that precede the getters. Valves FV217 and FV224 must be monitored because if they are open the xenon will bypass the getters. The top and bottom paths in Fig. 1.17 have one and two QDrives, respectively, so the flow through the bottom is larger. Installing a second QDrive on the top loop would not increase the flow because it was restricted by the pipes (as mentioned above this was eventually fixed) and would increase ^{222}Rn emanation.

Because the mass of xenon has been mostly stable since the detector came online valves leading to and from ReStoX (Sec. ??) and bottles do not need to be tracked. The total mass of xenon removed by the krypton column (Sec. ??) is negligible (0.07% through SR1) and can be ignored. The slow control parameters are summarized in Tab. 1.3.

The GXe flow into the purification system is calculated as

$$F_G^{(\text{in})} = \sum_i F_i \quad (1.12)$$

where F_i is the flow for $i = \text{FCV101}, \text{FCV102}, \text{FCV103}$. The inlet LXe flow is calculated

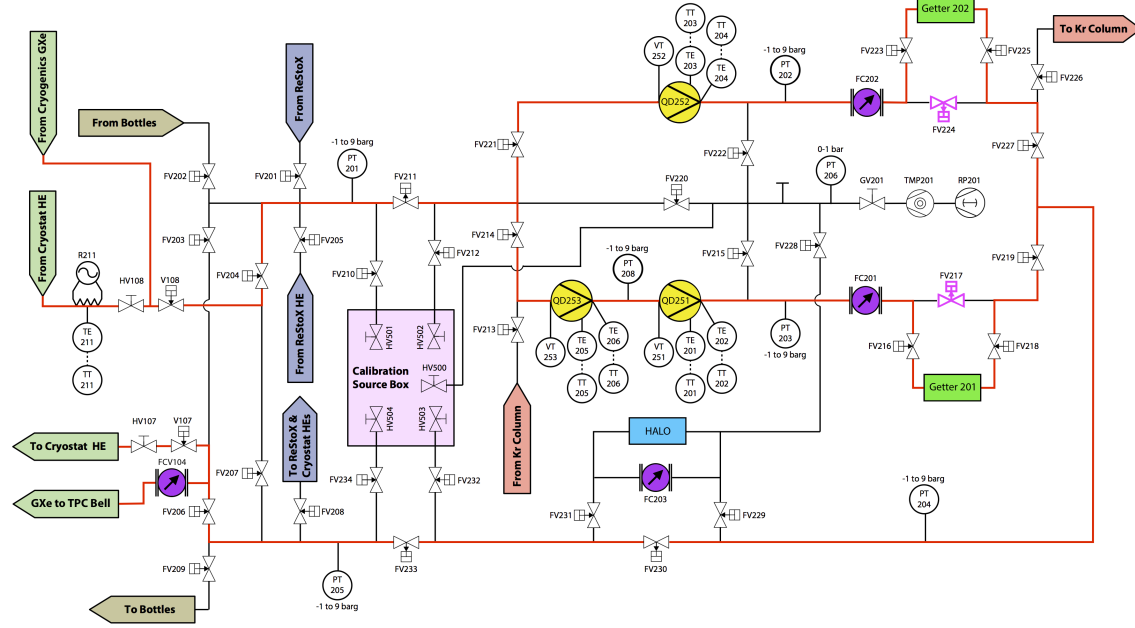


Figure 1.17: Schematic for purification system from slow control. LXe and GXe enter the purification system and pass through the top or bottom branch. They reunite before returning through the heat exchanger or as pressurized gas to the TPC Bell. QDrives (yellow), flow controls FC201 and FC202 (purple), getters (green), bypass valves (pink) and the HALO monitor (red) are highlighted. The path of xenon during ordinary operations is shown in red.

$$F_L^{(\text{in})} = \sum_j F_j - F_G^{(\text{in})} \quad (1.13)$$

for $j = \text{FC201}, \text{FC202}$. The flow that is purified is

$$F_G = F_G^{(\text{in})} \left[(1 - \text{Status}(\text{FV217})) \frac{F_{\text{FC201}}}{F^{(\text{in})}} + (1 - \text{Status}(\text{FV224})) \frac{F_{\text{FC202}}}{F^{(\text{in})}} \right] \quad (1.14a)$$

$$F_L = F_L^{(\text{in})} \left[(1 - \text{Status}(\text{FV217})) \frac{F_{\text{FC201}}}{F^{(\text{in})}} + (1 - \text{Status}(\text{FV224})) \frac{F_{\text{FC202}}}{F^{(\text{in})}} \right] \quad (1.14b)$$

where $\text{Status}()$ is 0 if closed and 1 if open. $F^{(\text{in})}$ is $F_G^{(\text{in})} + F_L^{(\text{in})} = F_{\text{FC201}} + F_{\text{FC202}}$.

1.3.3 Vaporization and Condensation

Impurity migration between the liquid and gas requires consideration of both volumes rather than strictly the liquid. Electronegative particles (e.g. O₂, CO, etc.) are expected to be more densely distributed in the GXe due to their lighter atomic mass. To parameterize the migration rates for an impurity from the liquid to the gas or vice versa, the condensation and vaporization rates need to be included.

The pulse-tube refrigerators (PTRs) and LN₂ supply the cooling power to the system (Sec. ??) and are balanced by heat from the GXe and resistive heaters (one on each coldfinger) that keep detector conditions stable. The resistive heaters are run by proportional-integral-derivative (PID) controllers and adjust in real-time to maintain a stable coldfinger temperature. Because there is no flow of heat into or out of the coldfinger the three balance

$$\dot{Q}_{\text{CF}} + \dot{Q}_{\text{GXe}} + \dot{Q}_{\text{H}} = 0 \quad (1.15)$$

where \dot{Q} is the heat transfer rate with $\dot{Q}_{\text{CF}} < 0$ and $\dot{Q}_{\text{GXe}}, \dot{Q}_{\text{H}} > 0$. Because the slow control system only monitors the resistive heaters the other two are disentangled via a measurement of \dot{Q}_{H} when the inner vessel was under vacuum before filling ($\dot{Q}_{\text{GXe}} = 0$). It was found to be $\dot{Q}_{\text{CF}} = -\dot{Q}_{\text{H}} = -260$ W. Eq. 1.15 can be rewritten as

$$\dot{Q}_{\text{GXe}} + \dot{Q}_{\text{H}} = 260 \text{ W} \quad (1.16)$$

so as the heat load from the xenon increases the current in the resistive heater decreases.

Purification has the greatest variability among heat sources during stable conditions as a result of changes in circulation speed. For roughly two days shortly after XENON1T came online purification was halted entirely, as shown in Fig. 1.18. Once the system stabilized $\dot{Q}_0 \equiv \dot{Q}_{\text{GXe}}$ was calculated via Eq. 1.16 to be 140 W. Because the system was stable the vaporization and condensation rates must be equivalent. The total xenon mass has remained unchanged by >99% so it is reasonable to assume the \dot{Q}_{H} and vaporization and condensation rates under these conditions hold true today.

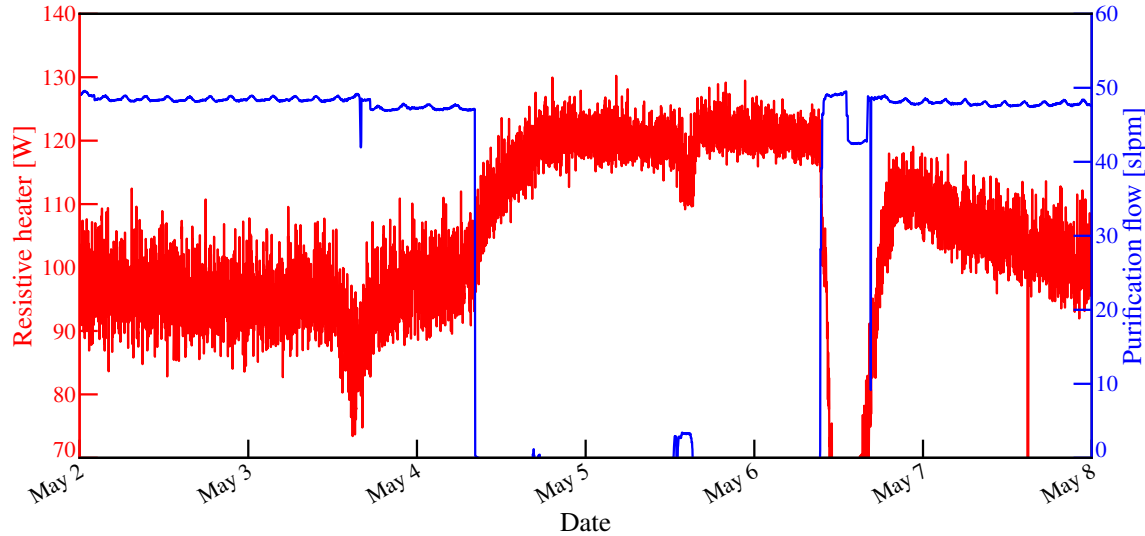


Figure 1.18: Heater power \dot{Q}_H (red) and purification flow (blue) from May 2–8, 2016. On May 4th circulation is stopped, decreasing the heat load in the GXe. \dot{Q}_H rises to ~ 120 W, so to satisfy Eq. 1.16 $\dot{Q}_{\text{GXe}} \sim 140$ W. When purification resumes on May 6th there is a sharp drop in \dot{Q}_H while the heat exchanger and other materials equilibrate before returning to a stable value.

While xenon returning from purification will add heat to the system, with a total mass of more than 3 t and narrow temperature range ($< 1^\circ\text{C}$ between bottommost and topmost sensors) the thermal load of the liquid xenon does not appreciably change. Therefore the vaporization rate is constant regardless of flow and can be modeled using the zero-flow period

$$M_G \frac{dI_G}{dt}^{(\text{vap})} = -M_L \frac{dI_L}{dt}^{(\text{vap})} = \frac{\epsilon_{\text{vap}} \dot{Q}_0 I_L}{L} \quad (1.17)$$

where ϵ_{vap} is the vaporization probability for impurities in the liquid and $L = 9.6 \times 10^4 \text{ J kg}^{-1}$ is the latent heat of vaporization.

The excess heat will increase the thermal load of the gas so its contribution to the coldfinger will grow. The specific heat for xenon gas at constant pressure is $c_p = 158 \text{ J kg}^{-1} \text{ K}^{-1}$. The condensation rate for xenon is

$$\begin{aligned}\dot{Q}_{\text{GXe}}^{\Delta T} + \dot{Q}_{\text{GXe}}^{(\text{cond})} &= \dot{Q}_{\text{GXe}} \\ \dot{m}c_p\Delta T + \dot{m}L &= \dot{Q}_{\text{GXe}} \\ \dot{m} &= \frac{\dot{Q}_{\text{GXe}}}{c_p\Delta T + L}\end{aligned}\tag{1.18}$$

where ΔT is the difference between the initial and vaporization temperatures. The condensation term in the model is

$$-M_{\text{G}} \frac{dI_{\text{G}}}{dt}^{(\text{cond})} = M_{\text{L}} \frac{dI_{\text{L}}}{dt}^{(\text{cond})} = \frac{\epsilon_{\text{cond}} \dot{Q}_{\text{GXe}} I_{\text{G}}}{c_p(T - T_0) + L}\tag{1.19}$$

where ϵ_{cond} is the probability of condensation for impurities in the gas and T is the temperature of the GXe inside the unpowered PTR cooling tower. Selecting a temperature sensor is somewhat arbitrary since the gas inside the inner vessel - despite a temperature range of $> 100^{\circ}\text{C}$ - should exhibit similar behavior. To account for this T_0 is left as a free parameter but constrained so that $T - T_0$ is within the vaporization and maximum detector temperatures.

A complication in calculating \dot{Q}_{GXe} is \dot{Q}_{CF} is known to decrease in time. This can be indirectly observed by the long-term behavior in \dot{Q}_{H} as shown in Fig. 1.19. As a result Eq. 1.16 leads to increasing overestimation of the condensation over time if not corrected, though this can be difficult since \dot{Q}_{H} also corrects for real temperature changes of the GXe. In addition, the rate of decrease is not consistent so piecewise corrections are applied. Fig. 1.19 shows the raw (from slow control) and corrected \dot{Q}_{H} over the course of the experiment.

1.3.4 GXe Purification

Because only the electrons drifting in the LXe lead to an S2 purifying the GXe was in the past not considered necessary. However, the light masses of electronegative impurities and higher temperatures that produce greater outgassing suggest that their concentration may be greater in the gas. Because impurities are exchanged between the liquid and gas (Sec. 1.3.3) their potential to compromise the electron lifetime is significant.

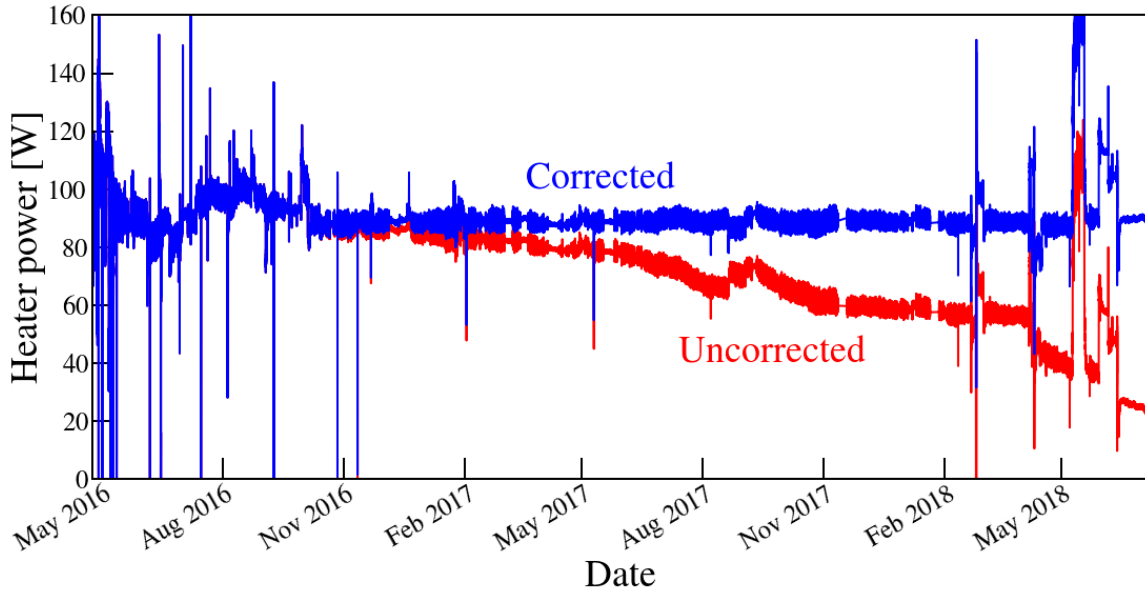


Figure 1.19: \dot{Q}_H over the lifetime of XENON1T. Sudden spikes and sporadic behavior result from compensating for rapid increases or decreases in heat from the GXe. Long-term downward trend is caused by the PTR cooling power decreasing over time. The corrected trend used in the fit is shown.

As part of the work leading up to XENON1T the Demonstrator installed piping connecting GXe outside the TPC to the purification system to investigate this effect. Fig. 1.20 shows the electron lifetimes over the course of the measurement using the 661.7 keV ^{137}Cs γ -ray. Two periods with GXe and LXe circulation were observed and are highlighted in blue. Each shows an increase in τ_e , though the second run only lasted a few days. The first measurement improves the lifetime from $\sim 200 \mu\text{s}$ to $\sim 450 \mu\text{s}$ and does not show signs of leveling off when the LXe-only circulation is restored. This confirmed the intuition that electronegative impurities in the GXe play an important role in the electron lifetime, and our dark matter search would benefit from assembling XENON1T for GXe purification.

Five lines connect the GXe volume of the XENON1T inner vessel to the purification system (Sec. ??). Three lines are attached to the cooling towers (one to each) since as the highest points they should contain the greatest impurity concentration. In addition they are warmest regions so their outgassing is expected to be the most substantial (Fig. ????). The three lines are joined before a flow control valve that

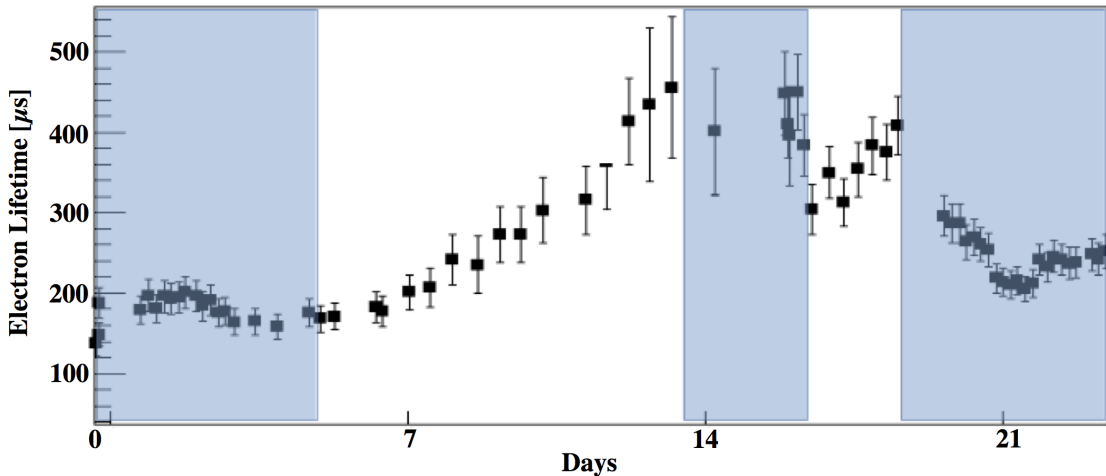


Figure 1.20: Electron lifetime using LXe with (white region) and without (blue) GXe circulation for the Demonstrator. The electron lifetime more than doubles in the first iteration over a roughly 10-day span. A period follows with only LXe purification, but is too short to observe much decrease. Upon re-initiating GXe flow the lifetime drops a bit - possibly due to trapped impurities in the GXe tubing - but then begins to climb again. The final block reveals the electron lifetime does decrease with LXe-only circulation. Longer periods with and without GXe purification are needed for better assessment. Image credit: [255].

regulates their flux. A fourth conduit is linked to the tube that carries the PMT signal and high voltage cables between the TPC and data acquisition. This region was selected because the cables were suspected of having high radon emanation, and the larger surface area means greater outgassing. Connecting directly to the purification system allows cleaning of higher impurity concentration gas and distillation of the radon. The flow is strong enough that the odds of an impurity or radon atom making it into the bell against the current is negligible. The final line is stationed approximately halfway between the TPC and cooling towers to purify GXe from the neck of the cryogenic system. This location was chosen to address two challenges: elevated radon emanation levels from cryogenics materials, and a predicted $\sim 20 \times$ higher oxygen level in the gas than liquid. The line is connected to the inner vessel in the service building at the point immediately outside the water tank to lessen the contaminants that reach the LXe through condensation either at the liquid-gas surface or from the PTR (Sec. 1.3.3). Both this line as well as the one connected to the cable tube have flow control valves that are independent from each other and the

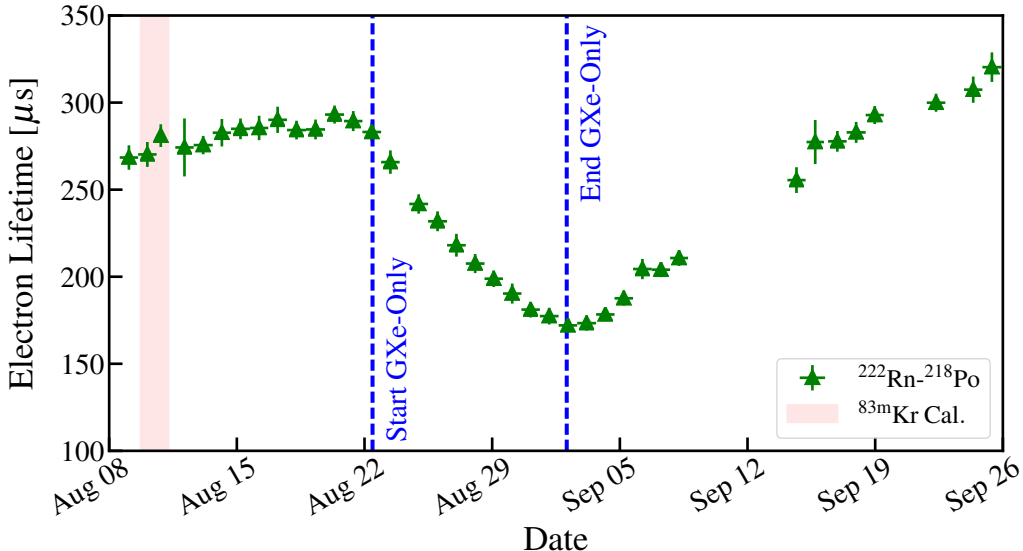


Figure 1.21: Purification of only xenon gas from August 22 - September 2, 2016, marked by green dashed lines. Electron lifetime measurements are from ^{222}Rn - ^{218}Po combined data. The purpose of the operation was to study the exchange of impurities between the gas and liquid, which depends on vaporization/condensation and outgassing.

cooling tower pipes, allowing custom ratios of flow between the three.

During standard operations GXe is passed through the getters at $F_{\text{G}} \sim 3.75$ slpm, or roughly 7-8% of the total flow during SR0 and SR1.

From August 22 to September 2, 2016 LXe purification was halted to study the effect that GXe purification has by decoupling it from the liquid. The electron lifetime decreased more rapidly than anticipated, indicating that while the impurities in the GXe were influential, they were not to the extent predicted by the Demonstrator. The physics of the GXe-only circulations in the Demonstrator and XENON1T is not yet fully understood, but future detectors may continue to provide insight into the interplay of GXe-LXe impurity exchange in a TPC. Modeling the GXe period of the evolution constrains the outgassing, vaporization, and condensation rates.

1.3.5 Outgassing and Leak

Xenon is continuously contaminated with impurities that outgas from detector materials. Therefore the outgassing model plays a critical role in the outcome of the

electron lifetime model. Historically electron lifetimes have followed a Fermi-Dirac during periods of rapid increase that result from a higher rate of impurity removal than influx. Once this phase has finished τ_e follows a linear-like upward trend, presumed to be tracking the decrease in outgassing. In the event of a purity degradation a Fermi-Dirac will ensue and the electron lifetime will return to the same line as before.

In the beginning of SR1 the α electron lifetime rapidly rose to $\sim 580 \mu\text{s}$ ($630 \mu\text{s}$ for $^{83\text{m}}\text{Kr}$) and began the expected linear-growth stage. However, instead of continuing this trend it plateaued around $\sim 600 \mu\text{s}$ ($650 \mu\text{s}$ $^{83\text{m}}\text{Kr}$). A time-independent outgassing model is known to be incorrect and gave a poor fit to the full evolution. A more likely scenario is the presence of a leak. While we cannot say definitively that a leak is the cause as it was never searched for, the presence of a time-independent impurity source is referred to in this chapter as a leak, and in the event it is not truly a leak the results do not change. Therefore the influx of impurities is modeled with outgassing and leak rates.

1.3.5.1 Outgassing Sources

There are three time-dependent outgassing sources: vaporization, diffusion, and desorption. These are well-understood for vacuum systems and while the pressure in the cryogenic system is $> 1 \text{ atm}$, much of the physics remains relevant for our detector.

Vaporization is the release of particles by producing a phase transition from a solid or liquid via heat. When the rate of particles evaporating is equivalent to the rate arriving the system is in dynamic equilibrium. If the vapor and solid/liquid host are at the same temperature in dynamic equilibrium the pressure of the vapor over the surface is equivalent to the vapor pressure of the solid/liquid. The flux of impurities leaving the surface is

$$n \left(\frac{k_B T}{2\pi m} \right)^{1/2} = nv/4 \quad (1.20)$$

where $v = (8k_B T/\pi m)^{1/2}$ is the mean speed for an ideal gas. Because the cryogenic system is designed to be thermally stable vaporization from new heat sources is mostly

irrelevant, with the exception of detector component replacement (Sec. 1.3.8). Instead vaporization primarily applies to atoms and molecules that have diffused to the inner surface from inside the material bulk.

Diffusion is the movement of one material through another. Particles inside our detector materials are naturally drawn to the surfaces by their own gas pressure. For a uniform initial concentration C_0 of dissolved gas inside a solid the outgassing rate is obtained by the diffusion equation to be

$$q = C_0 \left(\frac{D}{\pi t} \right)^{1/2} \left[1 + 2 \sum_{n=1}^{\infty} (-1)^n e^{-n^2 d^2 / Dt} \right] \quad (1.21)$$

where D is the diffusion constant and $2d$ is the thickness of the solid [256]. At small and large t the outgassing rate becomes

$$q(t) \approx \begin{cases} C_0 \left(\frac{D}{\pi t} \right)^{1/2} & t \ll \frac{d^2}{D}, \\ \frac{2DC_0}{d} e^{-\pi^2 Dt / 4d^2} & t \gg \frac{d^2}{D} \end{cases} \quad (1.22a)$$

$$(1.22b)$$

where Eq. 1.22 is derived by redefining the initial conditions in Eq. 1.21. For the lifetime of XENON1T the diffusion can be approximated by Eq. 1.22. This process is typically much slower than desorption so after desorption of initial surface contaminants diffusion dictates the outgassing rate.

The diffusion constant for a gas in a solid decreases as

$$D = D_0 e^{-E_D / RT} \quad (1.23)$$

where E_D is a measure of the attraction between a molecule and the surface to which it's adsorbed known as the *thermal activation energy*. Tab. 1.4 lists E_D and the relative fraction adsorbed for the most prevalent gases in normal air. D_0 is typically between $0.01\text{-}10 \text{ cm}^2 \text{ s}^{-1}$ for solids [257]. Eq. 1.23 explains why heating materials is such an effective method to reduce outgassing: even a small change in temperature can substantially expedite the time to reach lower outgassing. This is demonstrated in Fig. 1.22 where a sampler is heated from T_1 to T_2 for some duration before returning

1. PURITY AND THE ELECTRON LIFETIME

| Molecule | E_D [cal g ⁻¹ mole ⁻¹] | P_i [torr] | P_i/P_{tot} | f_{abs} |
|------------------|---|----------------------|----------------------|---------------------|
| N ₂ | 1630 | 592 | 0.78 | 7×10^{-7} |
| O ₂ | 1335 | 152 | 0.2 | 1×10^{-7} |
| H ₂ O | 9720 | 11 | 0.014 | 1 |
| Ar | 1558 | 5 | 0.007 | 6×10^{-9} |
| CO ₂ | 6030 | 0.23 | 3×10^{-4} | 5×10^{-7} |
| H ₂ | 216 | 3.8×10^{-4} | 4×10^{-7} | 4×10^{-10} |

Table 1.4: Activation energies E_D for normal air at 300°K. Data taken from [257].

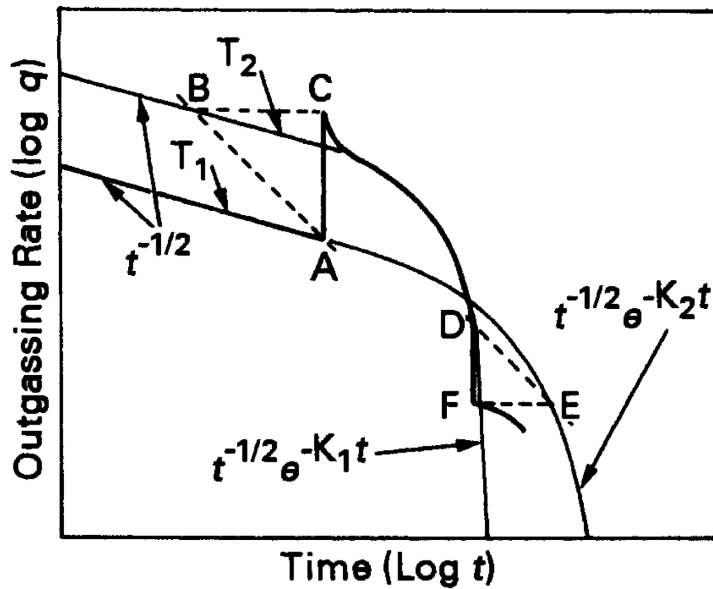


Figure 1.22: Outgassing rate q as a function of time for outdiffusion. A sample at temperature T_1 is heated to T_2 at point A . Because the gas concentration in the sample remains unchanged during this process (assume quickly heated) the outgassing at C is equivalent to B (diagonal dashed lines represent constant concentration). From C q quickly joins the T_2 curve, which begins its exponential descent (Eq. 1.22) earlier. At D the sample is restored to T_1 where it returns to its original curve at E but at an earlier time F . Image credit: [256].

to T_1 . The difference in pressure can be calculated using the reparameterization of Eq. 1.21 used in Eq. 1.22 to give

$$P_F = \frac{D_1}{D_2} P_D \quad (1.24)$$

where D_1 and D_2 correspond to the diffusion rates at lower and higher temperatures and P_F , P_D are the pressures at F and D [258].

| Sample | Treatment | Outgassing rates [10^{-13} Torr l s $^{-1}$ cm $^{-2}$] | | | |
|---|------------------------------------|---|-----------------|----------------|------|
| | | H ₂ O | CO ₂ | H ₂ | CO |
| A | Vacuum for 75 h | 430 | 10 | 670 | 65 |
| | 150°C bakeout for 50 h | 13 | 0.03 | 290 | 4.5 |
| B | 300°C bakeout for 40 h | 0.5 | 0.01 | 62 | 1.7 |
| C | 400°C degassing for 20 h in vacuum | 0.2 | 0.08 | 14 | 0.33 |
| D | 800°C degassing for 2 h in vacuum | - | 0.04 | 2.7 | 0.05 |
| 5-month exposure to atmosphere then vacuum for 24 h | | 55 | 10 | - | 50 |
| 150°C bakeout for 20 h | | - | 0.03 | 2.5 | 0.06 |

Table 1.5: Outgassing rates of H₂O, CO₂, H₂, and CO from 316L stainless steel after various treatments. Significant reductions from bakeouts can be seen. Before treatment each sample was subjected to a two-hour degreasing with perchlorethylene vapor at 125°C, followed by a one-hour ultrasonic washing at 55°C, and finally were rinsed with clean water and dried. Data is taken from [259].

Fig. 1.22 shows how heating a material accelerates its transition from Eq. 1.22 to Eq. 1.22. Thus baking materials shortens the time until the exponential decrease of gas in the solid and reduce the outgassing in the detector.

Desorption is the release of gases that were previously adsorbed on the wall of the system. The gases on the surface may be from diffusion, permeation (Sec. 1.3.5.3), or exposure to a previous or current environment.

In thermal desorption particles that are bound to a surface via weak van der Waals forces of < 40 MJ kg $^{-1}$ mole $^{-1}$ are labeled as *physisorbed* and are desorbed quickly under vacuum, while those at larger energy are *chemisorbed* and do so slowly unless external heat is applied. When more than one layer of particles exist on the surface they will desorb at a constant rate. However, once the coverage becomes less than one layer it will slow and become proportional to the surface concentration. Some molecules dissociate upon adsorption and recombine before desorption. This process depends on the square of the surface concentration so it can be much slower than normal desorption. This is especially relevant for diatomic molecules on metals.

In modeling desorption, re-adsorption of freed gases may need to be included. When baking it is necessary to heat all surfaces as any excluded regions will dominate outgassing once conditions are returned to equilibrium. The elevated pressure during a bake will cause larger than normal re-adsorption in these regions. If baking is done correctly the reduction in outgassing will be similar to diffusion - a slow initial process

but as the solid depletes its gases the decrease becomes exponential.

Outgassing rates for 316L stainless steel after various treatments are listed in Tab. 1.5 [259]. An unbaked sample has much higher outgassing than one that is baked at just 150°C for 50 hours. For these results the bakeouts were *in situ*, meaning the outer walls were exposed to atmosphere while the inner were in vacuum. This is a popular method because if kept at vacuum the detector is not re-exposed to large amounts of atoms and molecules. Sample B underwent a 300°C 40-hour bakeout and achieved <4% the H₂O outgassing rate of Sample A (150°C), highlighting the importance of temperature. Samples C and D were subjected to high-temperature degassing in an ultravacuum furnace. At 400°C for 20 hours C performs better than B in all elements except CO₂. D is degassed for just 2 hours at 800°C and performs better than C. It is then exposed to atmosphere for five months, followed by 24 hours in vacuum. It performs better than Sample A at vacuum exposure for 75 hours with no heat. After just a 150°C 20-hour bakeout its outgassing returns to the values of five months earlier. This suggests a high-temperature bake can cause a permanent (or at least long-term) decrease in the outgassing rate.

More details on desorption - including stimulated desorption (incident particles on solid surfaces releasing adsorbed gases) can be found in [256].

1.3.5.2 Outgassing Model

The outgassing models in the gas (Λ_G) and liquid (Λ_L) xenon characterize the rate of impurities outgassed from detector materials that freely roam throughout the GXe and LXe. This is different than modeling the total number of outgassed impurities because we only care about those that impact τ_e . Specifically Λ_G and Λ_L describe time-varying contamination. While the outgassing in Sec. 1.3.5.1 is based on research of vacuum systems the physical processes should be comparable to our detector. However, in a detector with so many components, temperatures ranging from roughly −100°C to 20°C, and time-dependent effects (e.g. purification flow, temperatures outside regions that are not vacuum insulated) building a truly accurate model is not feasible, and including too many terms will lead to overfitting. Everything must

instead be integrated into a single model that can describe the data.

To begin structuring the model we know outgassing decreases over time and is temperature-dependent. If temperatures are stable they can be ignored - or if only a handful of changes exist these periods can be supplemented with additional parameters. This is preferred because selecting specific temperature sensors will make the model partial to those regions, e.g. if the temperature rises in a cooling tower the entire GXe outgassing model should not be scaled accordingly - though in general the gas or liquid xenon should experience a similar reaction. Furthermore because the locations of the sensors were strategically selected to monitor the health of XENON1T, there are sections where knowledge about the temperatures are limited.

Temperature variations for three strategic regions are shown in Fig. 1.23. The narrow temperature range and good thermal isolation of the LXe keeps its temperature stable to well under 1%, with the exception of May and June 2016 when a number of operations were performed to understand and optimize detector conditions. The temperature sensor used for the LXe curve is situated just below the liquid surface and was chosen since warmer regions are of more interest. For the same reason the GXe sensor plotted is from the unpowered cooling tower. It fluctuates by roughly 2% through September 2016 but has not exceeded 1% since. The LN₂ coldfinger is more turbulent. It has been kept at 90°C since June 2016 by flushing GN₂ from the nitrogen storage tank. The larger variations may be because the temperature is a balancing act of the different heat transfer rates (Eq. 1.15) so it is more susceptible to sudden drops and rises than the GXe and LXe that have large thermal reservoirs. In addition the cooling power may experience fluctuations from small imperfections in the nitrogen flow or temperature. It appears to be increasing slightly but the total change is within 1%. From Fig. 1.17 it seems reasonable to ignore temperature dependence in the outgassing model.

Components within the gas and liquid do not have their own outgassing model since this would increase the number of parameters and lead to overfitting. However, the upgrades to the purification system in April-June 2018 likely disrupts this model as parts were removed and added. Thus while the same outgassing model is used

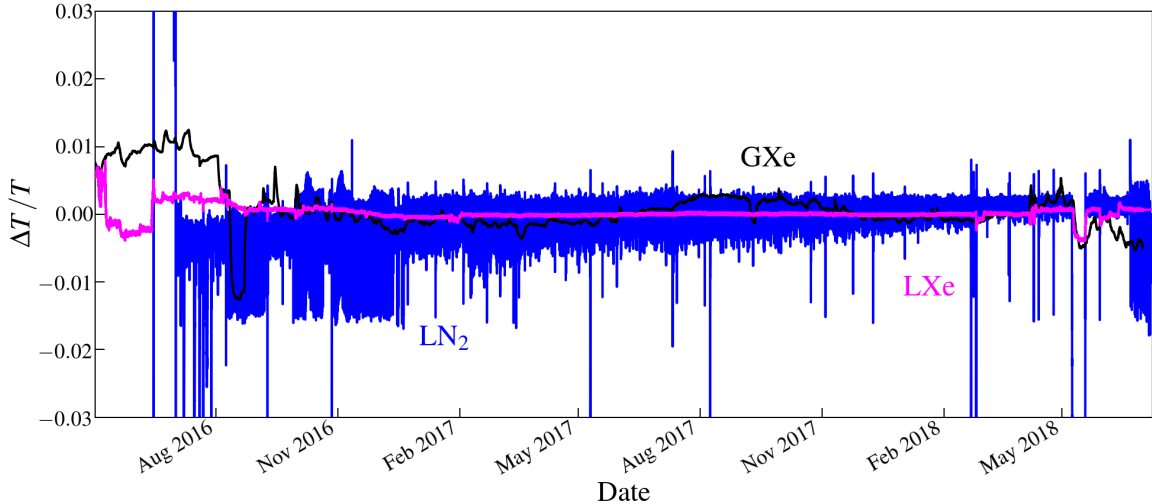


Figure 1.23: Relative temperature variations for sensors on the LN_2 coldfinger (blue), in the unpowered cooling tower (black), and just below the LXe surface (pink). The variation is defined as the $(T - T_{\text{med}})/T_{\text{med}}$ where T_{med} is the median temperature across all data. The LN_2 coldfinger shows the most volatility. The GXe changes by $\sim 2\%$ in the first several months of operation but is since stable within 1%. The LXe decreases by roughly 1% in the first couple months as adjustments to the detector were made. Since then its variation is $\ll 1\%$.

throughout the entire XENON1T lifetime, some outgassing parameters are limited to particular times.

The outgassing of the system should rapidly decrease in the beginning of the experiment and continue to do so more slowly as time goes on. A logical parameterization is an exponential. However, this cannot be expected to describe the entire outgassing for a complex system. The outgassing model that best describes the electron lifetime evolution is

$$\Lambda_G(t) = A_G(e^{-\beta_1 t} - \beta_2 t) \quad (1.25a)$$

$$\Lambda_L(t) = A_L(e^{-\beta_3 t} - \beta_4 t) \quad (1.25b)$$

where A and $\beta_i, \forall i \in \{1, 2, 3, 4\}$ are free parameters in the fit.

1.3.5.3 Time-Invariant Impurity Sources

Once τ_e flattens any time-invariant inflow of impurities should be the dominating contributor to the electronegative impurity concentration. There are two that are

relevant for XENON1T: permeation and leaks.

Permeation is the migration of particles from outside to inside the detector. A particle will adsorb onto the outer surface of the solid, diffuse through the material, and be desorbed on the interior. The rate of permeation will increase slowly until it ultimately reaches a steady-state influx of impurities.

Diatom molecules typically dissociate upon adsorption so they pass through the bulk as individual atoms. For steady-state permeation the molecule will dissociate upon the surface with equilibrium constant k_1 . Atoms on the surface then are admitted into the solid with equilibrium constant k_2 . Taking hydrogen as an example, the interior concentration is $n_H = k_2(k_1 n_{H_2})$ where n_H is the concentration of hydrogen atoms inside the solid and n_{H_2} is the hydrogen molecules on the exterior surface. The permeation flux is

$$Q_k = \frac{K_p(P_2^{1/2} - P_1^{1/2})A}{2d} \quad (1.26)$$

where K_p is the permeation constant, P_1 and P_2 are the interior and exterior pressures of the element, A is the surface area, and d is half the thickness of the material [256]. While Eq. 1.26 describes steady-state permeation

Permeation has a much weaker contribution than the outgassing sources discussed in Sec. 1.3.5.1. It is not expected to be seen in the lifetime of the experiment, so does not need to be included in this analysis.

Leaks present a more concerning problem as they are possible at any point during the experiment. There are two types of leaks: internal, where gas trapped inside the detector in or between materials streams out, and real, where gas originating outside of the system drifts through an opening.

The presence of a leak is supported by the flattening of τ_e around $600\ \mu s$ for α -decays and $650\ \mu s$ for ^{83m}Kr during Science Run 1. The residual gas analyzer (RGA) measurements of the vacuum between the inner and outer vessels did not reveal an increase in xenon, which should accompany the inflow of impurities if the leak existed between the vessels. Therefore the leak would either need to be internal, or from a component exposed to air. There are a number of possible candidates for the latter

including the pipes leading to and from the purification system, ReStoX, and the signal and HV feedthrough. The leak was never looked for because it would have required emptying the vessel.

1.3.5.4 Leak Model

Fits that supposed the leak was in the liquid matched the data better than those presuming the gas. This eliminates the cable feedthrough and lines to ReStoX since they are only in contact with GXe (during filling ReStoX can pump liquid). Supposing the leak is not internal the most likely candidate is the purification system, of which the majority of returning xenon goes to the liquid phase of the TPC.

Because τ_e is unchanging the LXe impurity concentration must be constant. Reducing the impurity influx into the LXe to that of the leak gives a rough estimate of the rate (while subdominant, nominal outgassing is still present). The calculation also assumes vaporization and condensation rates are in equilibrium - whether or not they actually does not matter for the fit. It then must be equivalent to impurity removal by the getters (Sec. 1.3.2)

$$R_I \equiv \frac{dI_L}{dt}^{(\text{leak})} = -\frac{dI_L}{dt}^{(\text{pur})} = \rho_{\text{GXe}} F_L I_L \quad (1.27)$$

where R_I is the leak rate and the right side is taken from Eq. 1.11b. The liquid impurity concentration is equivalent to

$$I_L = (\tau_e k)^{-1} \quad (1.28)$$

where $k = k(e^- + O_2)$ is the field-dependent e^- attachment coefficient described in Sec. 1.3.9. The purification flow during SR1 is ~ 48 slpm so

$$\begin{aligned}
R_I &= F_L \rho_{\text{GXe}} (\tau_e k)^{-1} \\
&= (48 \text{ slpm}) (5.984 \text{ g l}^{-1}) (600 \mu\text{s})^{-1} (0.004 \text{ s } \mu\text{s}^{-1} \text{ ppb}^{-1})^{-1} \\
&= (48 \text{ slpm}) (5.984 \text{ g l}^{-1}) (2.5 \text{ ppb}^{-1})^{-1} \\
&= 165 \text{ ppb kg day}^{-1}
\end{aligned} \tag{1.29}$$

where the α -decay electron lifetime is used (for ${}^{83\text{m}}\text{Kr}$ $R_I = 150 \text{ ppb kg day}^{\text{k}-1}$). Eq. 1.29 estimates the O₂-equivalent impurity concentration is in the low ppb realm, though still less than the designed value by more than a factor of 2. Being field-limited by the single electron hotspot prevents decreasing the attachment rate and thus increasing τ_e as shown in Fig. 1.29. Because outgassing should still make up a fraction of the impurity rate, electron lifetime measurements have uncertainty, vaporization and condensation rates may not be equivalent (though they be close), and F_L fluctuates slightly $165 \text{ ppb kg day}^{-1}$ should serve only as an approximation.

1.3.6 Getter Defficiencies

One of the stranger effects observed in the beginning of SR0 was a slow decrease in lifetime when it seemed detection conditions were not changing over a number of ($\lesssim 10$) days. Two more have appeared since then showing the same behavior. They are referred to as “getter defficiencies” because the evolution during these times follows $< 100\%$ removal of contaminants by the getters, and there is evidence to support this was the case for at least two of the three periods.

The first getter defficiency began on November 26, 2016 shortly after the ${}^{241}\text{AmBe}$ and ${}^{83\text{m}}\text{Kr}$ calibrations and ended on December 5. A power glitch occurred several days before that released a small number of impurities into the chamber (Sec. 1.3.7) but the lifetime was recovering when this decline began. This is the one getter defficiency that lacks an explanation. There were a number of ongoing operations at the time including ${}^{85}\text{Kr}$ distillation and pipette filling for RGMS - both of which use the purification system - but they don’t align perfectly with the dates. The electron lifetime over this period decreases by $\sim 10 \mu\text{s}$ and is shown in the left panel of Fig. 1.24.

1. PURITY AND THE ELECTRON LIFETIME

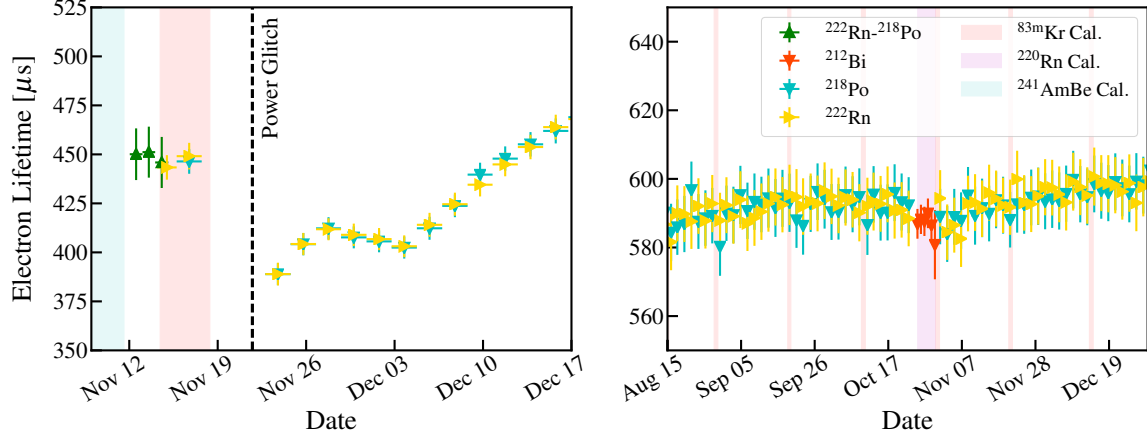


Figure 1.24: Periods of getter defficiencies for November 26 - December 5, 2016 (left) and October 25-30, 2017 (right). ^{222}Rn - ^{218}Po combined (green), ^{222}Rn , (yellow triangles), ^{218}Po (turquoise), and ^{212}Bi (red) electron lifetimes are shown. $^{83\text{m}}\text{Kr}$ (shaded orange), ^{220}Rn (purple), and $^{241}\text{AmBe}$ (green) calibrations are highlighted. The cause of the first deficiency in 2016 is not understood, as detector parameters are stable during this period. The getter deficiency in October 2017 is likely caused by an excess of impurities that were released from the ^{220}Rn calibration. Each resulted in a total drop of $\lesssim 10 \mu\text{s}$. The power glitch on November 21, 2016 causes a sudden purity decrease (Sec. 1.3.7).

The second instance was during the Science Run 0 ^{220}Rn calibration. Despite the calibration lasting for 13 days (December 19, 2016 to January 1, 2017) the first ~ 10 days or so were not useable as the valve in the calibration box Fig. ???? was left open. ^{220}Rn and ^{216}Po made it impossible to select ^{212}Bi α -decays, and the mixing of the three gives a rough value of τ_e but cannot be expected to be entirely accurate as learned from ^{222}Rn - ^{218}Po simultaneous fitting (Sec. 1.2.2). Although the values from these measurements should not be included in the fit, they still track the behavior of the evolution during this period. They show a steep decrease at the beginning of the calibration before returning to the expected evolution model.

The dip can be explained by considering impurity buildup inside the calibration source box. ^{220}Rn had been injected into the TPC roughly two months earlier but because it was for commissioning and not a true calibration the event rate was kept small ($\lesssim 50,000$ events hr^{-1}). Impurities from the calibration source box would have also been low and more likely to be removed by the getters. In the following months impurities from outgassing and handling would have likely accumulated, and

for the SR0 calibration the rate reached $> 200,000$ events hr^{-1} within 7 hours and $> 300,000$ events hr^{-1} within 17 hours. The higher influx from the source box would have carried with it larger concentrations of impurities, which would explain the dip and - once the high concentration of impurities from inside the source box became sufficiently low - the return to the previous trend.

The third period was the final ^{220}Rn calibration of Science Run 1 (October 25-30, 2017). Instead of the 3-4 week spacing between calibrations - as with the previous three - more than 10 weeks passed. As with SR0, impurity buildup may have become large enough to lower the getter efficiency. The total drop in purity is $\lesssim 10 \mu\text{s}$, and is shown in the right panel of Fig. 1.24.

To model the getter defficiencies Eq. 1.11a and 1.11b become

$$\frac{dI_G}{dt}^{\text{(gd)}} = \alpha_i \frac{dI_G}{dt}^{\text{(pur)}} = -\alpha_i \rho_{\text{GXe}} F_G I_G \quad (1.30\text{a})$$

$$\frac{dI_L}{dt}^{\text{(gd)}} = \alpha_i \frac{dI_L}{dt}^{\text{(pur)}} = -\alpha_i \rho_{\text{GXe}} F_L I_L \quad (1.30\text{b})$$

with $\alpha_i \in [0, 1]$ where α_i is the i^{th} getter defficiency.

1.3.7 Impurity Spikes

April 14 18:27 LXe level too high, adjusted by Ops Manager. April 16 17:05 normal power turned off. April 19 9:03 and 9:09 normal power turned off. PTR with LN2 test May 9-18.

On a number of occasions sudden drops in purity occurred. Unlike the getter defficiencies (Sec. 1.3.6), these drops were immediate and had no measurable duration. In all cases they were traceable to changes in the state of the detector. In total there were two impurity spikes before science run data, two during Science Run 0, one during Science Run 1, and three following SR1 (Sec. 1.3.8). They all align with changes in parameters monitored by the slow control system (in most cases due to part of detector being unpowered). In some instances it is difficult to distinguish the responsible parties because several abnormalities occurred. Each case is listed in

1. PURITY AND THE ELECTRON LIFETIME

| Date | Origin | Region | Possible cause | $\sim\tau_e$ [μs] | $\sim\Delta\tau_e$ [μs] |
|----------------------|----------------------|-----------|--------------------------------|-------------------|-------------------------|
| June 14, 2016 | Power glitch | GXe | PTR power → 0 | 65 | -30 |
| July 15, 2016 | LN ₂ test | GXe | PTR power → 0 | 225* | -100 |
| Nov. 21, 2016 | Power disruption | LXe | Temperature increase | 450 | -75 |
| Jan. 18-Feb. 1, 2017 | Earthquake | GXe + LXe | Liquid level change | 520* | -120 |
| June 5, 2017 | Gate washing | LXe | Liquid level change | 575 | -50 |
| Feb. 21, 2018 | Power glitch | GXe | PTR power drop of ~50% | 600 | -150 |
| Feb. 24, 2018 | Blackout | GXe + LXe | PTR power → 0, $F_G = F_L = 0$ | 500* | -150 |
| Mar. 5-7, 2018 | Gate washings | LXe | Liquid level change | 450 | -70 |

Table 1.6: Purity drops over the lifetime of XENON1T. Dates and expected causes are listed, along with the detector region (GXe or LXe) in which the impurity release is thought to occur. Possible causes, τ_e , and change in τ_e from α lifetime measurements are given. Cases where data is not available for several days or weeks following a drop are marked with *.

Tab. 1.12 along with relevant information.

June 14, 2016 The first impurity spike happened when a power glitch shut off the operating PTR. The coldfinger, which is kept at -98°C warmed, releasing impurities that had condensed on and around its surface into the GXe. Power was quickly restored and the detector remained stable, but the impurities condensed and diffused into the liquid, causing a dip of $\Delta\tau_e \sim -30$ μs.

July 15, 2016 The second purity drop occurred during a LN₂ test. In the event both PTRs lose power and the uninterruptible power supply (UPS) does not work properly, LN₂ from the dewar outside the service building is transferred to the third cooling tower to maintain safe detector conditions (it is nominally kept at -90°C to quicken the transition). A test was performed to ensure it worked properly. Like the first spike, the warming of the PTR allowed contaminants to diffuse into the GXe. The electron lifetime dropped by approximately 100 μs.

November 21, 2016 In the beginning of SR0 (following the ²⁴¹AmBe and ^{83m}Kr calibrations but before dark matter data taking) the experiment experienced a power disruption. The PTR was stable but temperature sensors show a small increase in the liquid, leading to drop of roughly 75 μs. It is visible in the left panel of Fig. 1.24.

January 18-February 1, 2017 Science Run 0 ended because of an earthquake in the Gran Sasso area. Following the earthquake electron emission, or a *hotspot*, was observed while running at the SR0 cathode voltage $V_c = 12$ kV. Over the next two

weeks the hotspot did not disappear except at lower voltages so it was decided to use $V_c = 8$ kV for SR1. During this window the liquid level increased for a period before returning to the SR0 height. A number of operations were done so it is possible one or more are responsible. Since the conditions were unstable this data was not used in the combined analysis, so τ_e did not need to be measured. A rough estimate of the change in τ_e is $-120\ \mu\text{s}$, but this value is dependent on when the drop (or drops) occurred.

June 5, 2017 At the end of May 2017 a hotspot appeared on the gate. Lowering the anode voltage from 4 to 3.6 kV eliminated the electron emission but also decreased the extraction efficiency (Sec. ??). To fix this a “gate washing” - lifting the TPC slightly so the gate rises out of the LXe and submerging it again - was done. The hope that whatever was causing the hotspot (e.g. a particle) would be “washed” away. Upon returning the anode voltage to 4 kV the hotspot had disappeared and normal dark matter data taking resumed. The dip in τ_e ($-50\ \mu\text{s}$) is suspected to come from impurities nested in the PTFE just above the liquid level that were dispersed throughout the LXe once submerged.

February 21, 2018 Roughly two weeks after the end of SR1 the PTR power dropped by $\sim 50\%$ because of a power glitch. The change in τ_e was approximately $-150\ \mu\text{s}$. The decrease in τ_e was larger than that from June 5th, indicating the concentration of impurities on the coldfinger may be larger compared to those on the PTFE near the LXe surface, though this is likely dependent on other factors such as temperature and time between drops.

February 24, 2018 Three days after the power glitch there was a blackout that turned off the PTR and a number of other components. In addition, purification was stopped for ~ 12 hours so impurities inside the tube that connects the LXe to the purification system would have been able to diffuse into the liquid.¹ The cathode remained off for nearly two weeks. The decrease in electron lifetime is estimated at $-150\ \mu\text{s}$.

¹During normal operations it is extremely rare that an impurity will reach the LXe against the flow.

1. PURITY AND THE ELECTRON LIFETIME

March 5-7, 2018 Upon ramping V_c back to 8 kV after the blackout a hotspot on the gate emerged. Three gate washings spaced roughly 24 hours apart were able to remove the hotspot. As with the June 5, 2017 gate washing it is likely impurities near the liquid surface would have been submerged. This resulted in a decrease of 70 μs .

The purity drops are modeled as

$$\text{GXe purity drop} = M_G \Delta I_G^{(i)} \int \delta(t - t_G^{(i)}) dt \quad (1.31\text{a})$$

$$\text{LXe purity drop} = M_L \Delta I_L^{(i)} \int \delta(t - t_L^{(i)}) dt \quad (1.31\text{b})$$

where $\Delta I_L^{(i)}$ and $\Delta I_G^{(i)}$ are free parameters representing the magnitude of the drops and $\delta(t - t^{(i)})$ is the delta function for the i^{th} instance.

Once the detector returns to nominal operating conditions the impurities are removed by the getters and within a period of days to weeks - depending on τ_e and $\Delta I_{G/L}^{(i)}$ - the electron lifetime returns to its original trend. However, for a stretch of time during or following the spike the governing physics of the electron lifetime evolution may deviate from predicted behavior.

When the coldfinger is warmed the concentration of attached impurities decreases as they get enough thermal energy to leave. Following a return to normal conditions the concentration of contaminants passed to the liquid via condensation (Sec. 1.3.3) is lower. Additionally the rate of evaporation of contaminants from the coldfinger should also decrease, though at -98°C this should have a small effect.

Aside from the itself modeling these changes can be difficult because the physics of these processes is not well understood. Studies of to what extent impurities coalesced on the coldfinger have on ϵ_{cond} , or how impurities bond to materials in and out of LXe need to be investigated. These effects are not modeled in the electron lifetime evolution, though because they are brief and the net effect is an immediate purity drop it is not necessary.

1.3.8 Hardware Upgrades

The most difficult parts of the electron lifetime model to characterize are online detector operations. The reason is they disrupt the system and in many cases the change is permanent and its effect on the model can be difficult to diagnose.

The first major operation was the installation of the third QDrive to the purification system from September 29 - October 5, 2016. The circulation was at \sim 45 slpm - just 45% of the designed flow - and required running the QDrives at high voltages. The suspension of flow through one of the two purification branches led to a decrease in τ_e as shown in Fig. 1.25. Once the upgrade was completed the flow increased to \sim 55 slpm with the QDrives running at safe voltages. In addition to the QDrive, buffer volumes were installed to relieve pressure between the pumps. These additions likely added more outgassing (additionally the QDrive increased ^{222}Rn , though this is irrelevant to the electronegative purity). However, since xenon passes through the getter after the QDrives it is not expected to change the outgassing model or purity because the model assumes that 100% of all contaminants are absorbed by the zirconium. However, there are plausible scenarios when this would not be the case, such as large initial impurity residue on the materials from exposure to air during installation, an sizable initial outgassing that overwhelms the getters, or the rise in flow speed (Sec. 1.3.2).

During Science Runs 0 and 1 no hardware was exchanged so detector conditions were stable. In April 2018 pipes in the purification system were upgraded from 1/2" outer diameter to 1" to increase conductance. When purification resumed the circulation speed reached 70 slpm.

The final hardware upgrade was in the middle of June when a magnetic pump was installed in parallel to the QDrives. With the QDrives off it reached \sim 80 slpm. The slow control schematic of the modification to the purification system can be seen in Fig. 1.27.

The QDrives were chosen in part because they did not risk exposure to air if something were to break, unlike KNF pumps used in the past. However, they could

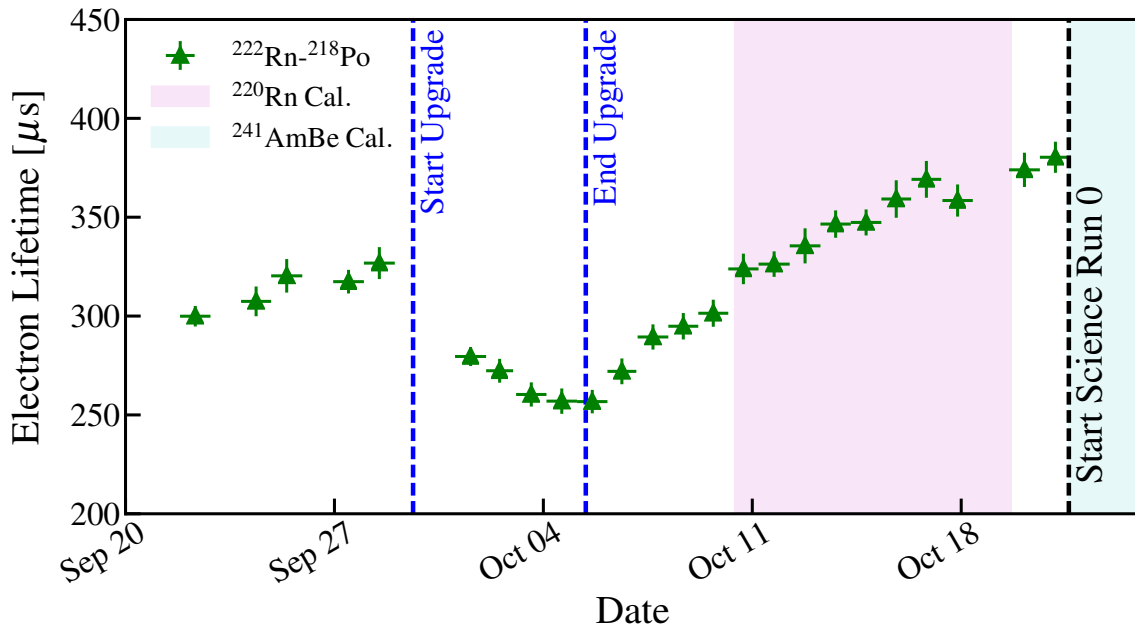


Figure 1.25: Installation of the third QDrive in the purification system from September 29 - October 5, 2016. Lifetimes are measured with ^{222}Rn - ^{218}Po combined data (green). ^{220}Rn and $^{241}\text{AmBe}$ calibrations are shaded purple and turquoise, respectively.

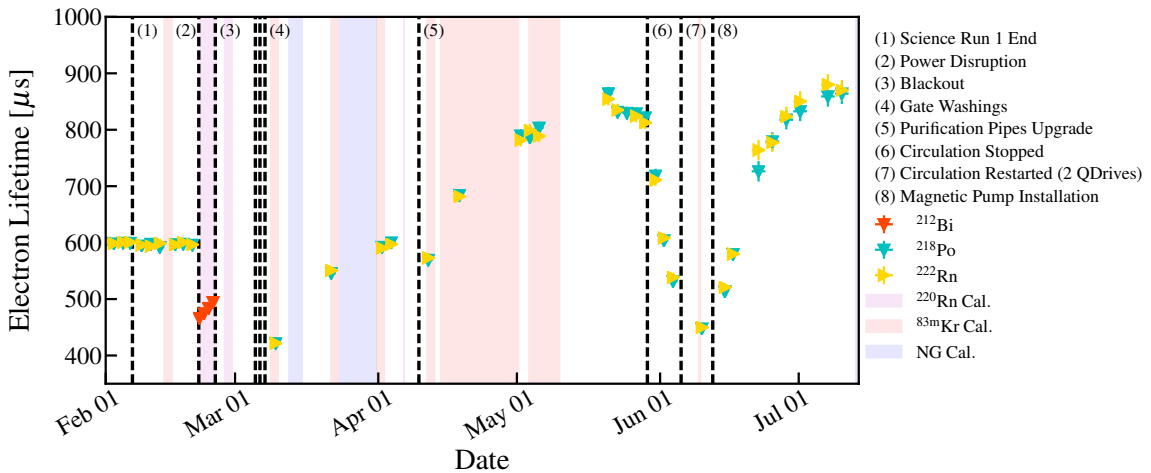


Figure 1.26: Electron lifetime measurements following the end of SR1. Initial drops in purity are due to a power disruption, blackout, and gate washings. Subsequent changes are caused by upgrades to the purification system.

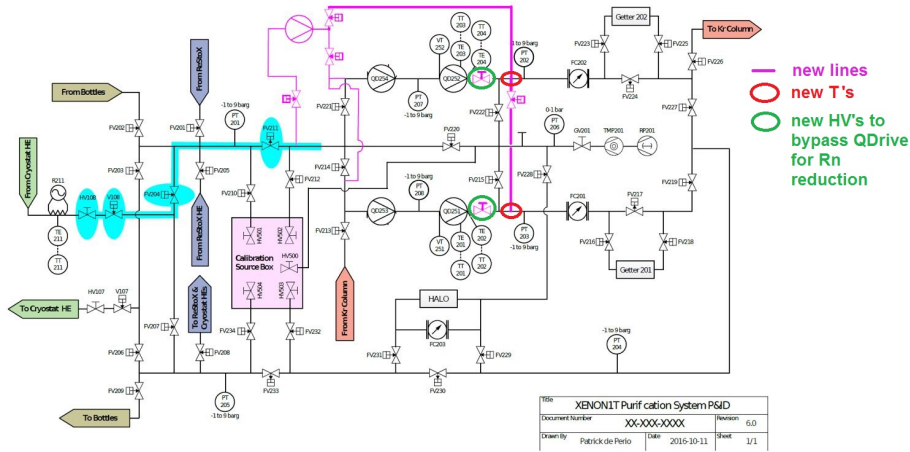
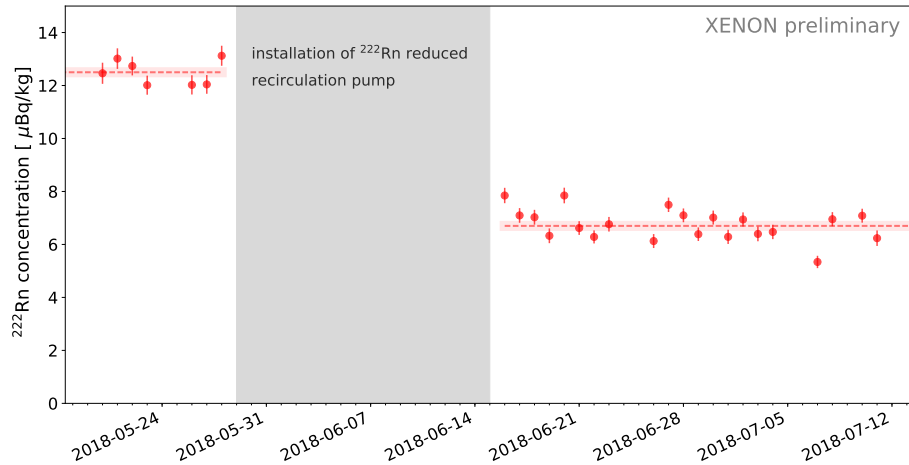


Figure 1.27: Figure out what schematic this is for.


 Figure 1.28: ^{222}Rn concentration before and after the magnetic pump upgrade. A drop from 12.5 ± 0.2 to $6.8 \pm 0.2 \mu\text{Bq kg}^{-1}$ is observed. Preliminary plot.

be unreliable - especially at higher flows - and are one of the highest contributors to the ^{222}Rn background with an estimated contribution of 30% from screening during commissioning. Once the QDrives were removed from circulation the ^{222}Rn event rate dropped from 12.5 ± 0.2 to $6.8 \pm 0.2 \mu\text{Bq kg}^{-1}$, or $\sim 45\%$, as shown in Fig. 1.28. The larger than expected decrease may be due to only two of the three QDrives in service having been screened (QD251 and QD253) to estimate the contribution. Higher radon emanation from the third would inflate the QDrive fraction of the radon budget. A second possibility is the screening tests were performed at room temperature, but higher temperature while running might escalate emanation.

The success of the magnetic pump is encouraging for XENONnT where the electron lifetime needs significant improvement and the background needs to be smaller. It has only been in use for < 3 months so other beneficial or adverse effects may appear, but so far the upgrade appears promising.

The number of hardware updates for the purification system reflects the shortcomings in meeting design specifications: 100 slpm and $\tau_e > 1$ ms. This was the first attempt at ton-scale purification and what has been learned will be applied to the XENONnT upgrade.

1.3.9 Field Dependence

In addition to inhomogeneous variations in charge yields (Sec. 1.2.5) the electric field affects the attachment rate constant k for the reaction



for some impurity S. The attachment rate describes the attraction between electrons and some element or molecule. Because oxygen is expected to have the highest concentration the model uses the O₂ attachment rate (thus impurities fit are modeled in O₂-equivalence). Unfortunately very little research has been done on this topic so the model uses a measurement from 1976 [175], shown in Fig. 1.29. It measured the oxygen attachment rate constant $k(O_2 + e^-)$ decreases at higher E_d . SF₆ follows this trend though is larger, while N₂O increases at larger field.

Oxygen is expected to be by far the most prevalent and dangerous contaminant. But small quantities of other molecules exist whose electron attachment rate constants are unknown are not considered. The magnitude of the effect is likely small but should not be overlooked. Because the results in Fig. 1.29 are the sole measurement additional measurements are needed.

The electron lifetime is calculated as

$$\tau_e = \frac{1}{I_L k} \quad (1.33)$$

which is used to compute the log-likelihood in the fit (Sec. 1.4.1).

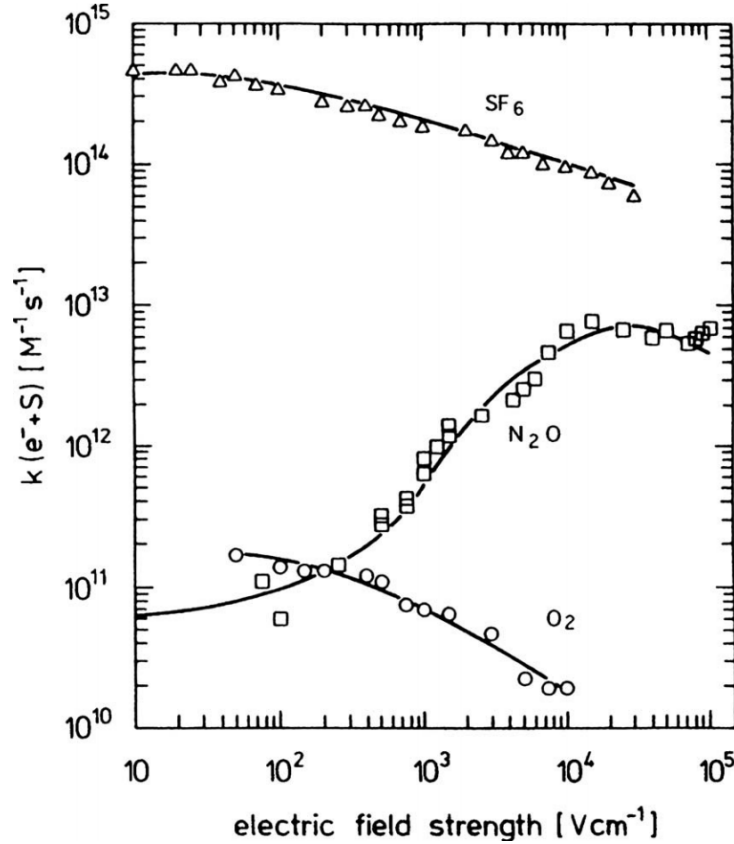


Figure 1.29: Field-dependent attachment rates for O_2 , N_2O , and SF_6 . Because analysis uses O_2 to model all impurities the attachment rate will decrease with electric field. Image credit: [175].

1.4 Electron Lifetime Fit

Putting the elements from Sec. 1.3 together gives the impurity evolution model

$$M_G \frac{dI_G}{dt} = -\alpha F_G \rho_{GXe} I_G + \frac{\epsilon_{\text{vap}} \dot{Q}_0 I_L}{L} - \frac{\epsilon_{\text{cond}} \dot{Q}_{GXe} I_G}{c_p \Delta T + L} + \Lambda_G + \sum_i M_G \Delta I_G^{(i)} \int \delta(t - t_G^{(i)}) dt \quad (1.34a)$$

$$M_L \frac{dI_L}{dt} = -\alpha F_L \rho_{GXe} I_L - \frac{\epsilon_{\text{vap}} \dot{Q}_0 I_L}{L} + \frac{\epsilon_{\text{cond}} \dot{Q}_{GXe} I_G}{c_p \Delta T + L} + \Lambda_L + R_I + \sum_i M_L \Delta I_L^{(i)} \int \delta(t - t_L^{(i)}) dt \quad (1.34b)$$

with $\alpha = 1$ for all times except periods of getter defficiencies (Sec. 1.3.6).

1.4.1 Statistical Inference

The majority of the model is fit to electron lifetime measurements from ^{222}Rn (Sec. 1.2.2) because its emanation from detector materials meant it could be continually used to measure τ_e . However, in beginning of the experiment electron lifetime measurements were done using S2/S1 (Sec. 1.2.1), and once the α background could be used the lifetimes were computed using α -decays from ^{222}Rn - ^{218}Po together. Late it was realized that this combined fit slightly underestimated the lifetime so τ_e was recalculated with separate fits for ^{222}Rn and ^{218}Po . However, the electron lifetimes preceding SR0 could not be recalculated because the data had been deleted. A comparison between the two was used to adjust the ^{222}Rn - ^{218}Po fits to align with expected values.

For this analysis the likelihood is calculated as

$$\mathcal{L}_i = \exp \left[-\frac{(\tau_{e,i} - \hat{\tau}_{e,i})^2}{2\sigma_{e,i}^2} \right] \quad (1.35a)$$

$$\mathcal{L} = \prod_i \mathcal{L}_i \quad (1.35b)$$

$$\ln \mathcal{L} = - \sum_i \frac{(\tau_{e,i} - \hat{\tau}_{e,i})^2}{2\sigma_{e,i}^2} \quad (1.35c)$$

where $\tau_{e,i}$ and $\hat{\tau}_{e,i}$ are the measured (Sec. 1.2) and predicted electron lifetimes, respectively. Because previous measurements do not exist the only constraints on $p(\boldsymbol{\theta}|\boldsymbol{\alpha})$ come from physical limitations. A Markov Chain Monte Carlo is used to fit $\ln \mathcal{L}$ (Sec. 1.4.2).

1.4.2 Markov Chain Monte Carlo

Similar to the electronic and nuclear recoil banding fitting for the dark matter search analysis (Sec. ??) this analysis uses a Markov Chain Monte Carlo (MCMC). MCMCs use k walkers to explore the target distribution over T iterations. Each walker $i \in \{1, \dots, k\}$ has parameters $\boldsymbol{\theta}_i$ with proposed steps based on the current positions of the walkers, making MCMCs memoryless - that is, there is no advantage to having

knowledge of previous steps.

This analysis uses a Differential Evolution Markov Chain (DEMC) rather than the Affine-Invariant Ensemble Sampler used in the dark matter search. The two are similar in that they are both random walk Monte Carlos and companion walkers are used to draw proposals. Both are homogeneous, satisfy detailed balance, and have their posteriors as their stationary distributions (see Sec. ?? for details concerning MCMCs).

The DEMC method used in this fit follows from [260] with improvements suggested in [261] and a snooker updater outlined in [262].

1. Initialize k walkers of n -dimensional parameter space to some state $\boldsymbol{\theta}(t = 0)$ (for this analysis random samples are drawn from within a specified range).
2. Set $\gamma_0 = 2.38/(2n)^{1/2} = 2.38/(2\dot{5}1)^{1/2} = 0.236$ and $\sigma_\gamma = 10^{-4}$.
3. Update each $\{\boldsymbol{\theta}_i, \forall i = 1, \dots, k\}$.
 - a) With 80% probability use the standard DEMC from [260], [261]. Randomly select two of the $k - 1$ walkers, $\boldsymbol{\theta}_{r_1}$, $\boldsymbol{\theta}_{r_2}$ and propose step

$$\boldsymbol{\theta}_p = \boldsymbol{\theta}_i + \boldsymbol{\Theta}_{r_1, r_2} \boldsymbol{\gamma} \quad (1.36)$$

where $\boldsymbol{\Theta}_{r_1, r_2}$ is a matrix with $\boldsymbol{\theta}_{r_1} - \boldsymbol{\theta}_{r_2}$ diagonal elements

$$\Theta_{ij} = (\theta_{i, r_1} - \theta_{i, r_2})\delta_{ij} \quad (1.37)$$

where δ_{ij} is the Kronecker delta and $\boldsymbol{\gamma} = \gamma_0(\mathbf{1} + \mathbf{z})$ where $\mathbf{z} \sim \text{Norm}(0, \sigma_\gamma)^n$. \mathbf{z} is necessarily symmetric to guarantee the jump from $\boldsymbol{\theta}_i$ to $\boldsymbol{\theta}_p$ is as likely as the reverse, and must be included to ensure any state can be reached with probability > 0 . The acceptance probability of the new step is chosen as

$$q = \min\left(1, \frac{\mathcal{L}(\boldsymbol{\theta}_p)p(\boldsymbol{\theta}_p|\boldsymbol{\alpha})}{\mathcal{L}(\boldsymbol{\theta}_i)p(\boldsymbol{\theta}_i|\boldsymbol{\alpha})}\right) \quad (1.38)$$

which is just the Metropolis ratio. An illustration of this method is shown in the left panel of Fig. 1.30.

b) The remaining 20% of proposals will be drawn using a snooker updater [262]. This method begins by randomly selecting three of the $k - 1$ chains such that $\boldsymbol{\theta}_i, \boldsymbol{\theta}_{r_1}, \boldsymbol{\theta}_{r_2}, \boldsymbol{\theta}_{r_3}$ are each distinct. Projections of the first two are calculated

$$\boldsymbol{\theta}_{p_1} = \left[(\boldsymbol{\theta}_{r_1} - \boldsymbol{\theta}_i) \cdot (\boldsymbol{\theta}_{r_3} - \boldsymbol{\theta}_i) \right] \frac{\boldsymbol{\theta}_{r_3} - \boldsymbol{\theta}_i}{\|\boldsymbol{\theta}_{r_3} - \boldsymbol{\theta}_i\|^2} \quad (1.39a)$$

$$\boldsymbol{\theta}_{p_2} = \left[(\boldsymbol{\theta}_{r_2} - \boldsymbol{\theta}_i) \cdot (\boldsymbol{\theta}_{r_3} - \boldsymbol{\theta}_i) \right] \frac{\boldsymbol{\theta}_{r_3} - \boldsymbol{\theta}_i}{\|\boldsymbol{\theta}_{r_3} - \boldsymbol{\theta}_i\|^2} \quad (1.39b)$$

as shown in the right panel of Fig. 1.30. A step is proposed

$$\boldsymbol{\theta}_p = \boldsymbol{\theta}_i + \gamma_0(\boldsymbol{\theta}_{p_1} - \boldsymbol{\theta}_{p_2}) \quad (1.40)$$

using the projections from Eq. 1.39. Finally, the acceptance probability is

$$q = \min\left(1, \frac{\mathcal{L}(\boldsymbol{\theta}_p)p(\boldsymbol{\theta}_p|\boldsymbol{\alpha})}{\mathcal{L}(\boldsymbol{\theta}_i)p(\boldsymbol{\theta}_i|\boldsymbol{\alpha})} \frac{\|\boldsymbol{\theta}_p - \boldsymbol{\theta}_{r_3}\|^{n-1}}{\|\boldsymbol{\theta}_i - \boldsymbol{\theta}_{r_3}\|^{n-1}}\right) \quad (1.41)$$

and we can see that q becomes small for $\boldsymbol{\theta}_p \approx \boldsymbol{\theta}_{r_3}$.

4. Generate a random number from a uniform distribution $r \in [0, 1]$. If $r < q$ then accept $\boldsymbol{\theta}_p$, otherwise reject and remain in current state.
5. Define the acceptance of proposed states across all chains as $f = k_{\text{acc}}/k$ where k_{acc} is the number of accepted proposals in current iteration.
6. Adjust γ_0 to maintain an acceptance fraction of ~ 0.25 . If it dips too low $\boldsymbol{\theta}_p$ may on average be over-extending to regions of low likelihood, while if too high it may be a sign that there are more farther regions that should be explored. It is reset to 1 every 100 iterations to account for multi-modal distributions.
 - (i) If $100 | t$ then $\gamma_0 = 1$.
 - (ii) If $f < 0.2$ then $\gamma_0 = 0.9\gamma_0$.
 - (iii) If $f > 0.31$ then $\gamma_0 = 1.1\gamma_0$.
 - (iv) Otherwise $\gamma_0 = \gamma_0(2f^{1/2})$.
7. Set $t = t + 1$.
8. Repeat steps 3–7 for T iterations.

The acceptance probability in Eq. 1.38 can be rewritten

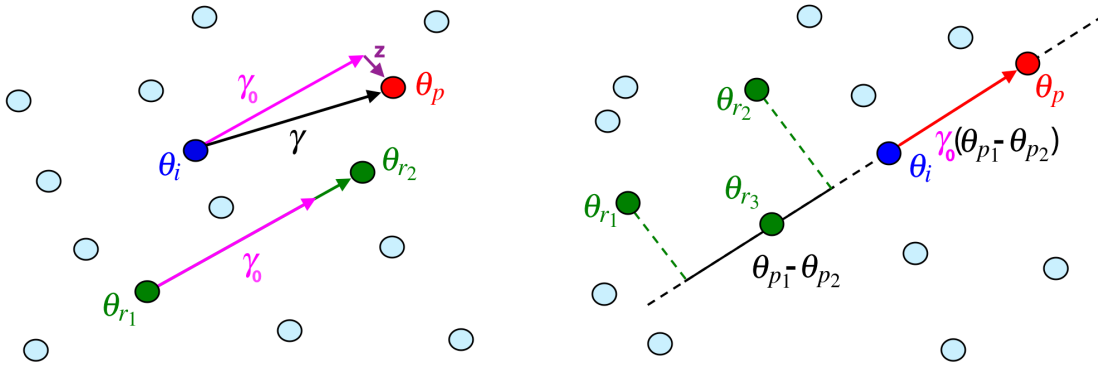


Figure 1.30: Examples of $\boldsymbol{\theta}_p$ using DEMC (left) and DEMC snooker update (right) in two dimensions. Example of normal DEMC proposal (item 3a). The difference between two randomly selected walkers $\boldsymbol{\theta}_{r1}, \boldsymbol{\theta}_{r2}$ is used to propose an update to the i^{th} walker using Eq. 1.36 in two dimensions. $\boldsymbol{\theta}_p$ and $\boldsymbol{\theta}_{r1} - \boldsymbol{\theta}_{r2}$ are at a slight tilt with respect one another due to \mathbf{z} . Example of DEMC snooker update proposal (item 3b). An update is proposed using difference of projections of $\boldsymbol{\theta}_{r1}, \boldsymbol{\theta}_{r2}$ along $\boldsymbol{\theta}_{r3} - \boldsymbol{\theta}_i$ where $\boldsymbol{\theta}_{r3}$ is a third randomly drawn walker using Eq. 1.40.

$$\frac{\mathcal{L}(\boldsymbol{\theta}_p)p(\boldsymbol{\theta}_p|\boldsymbol{\alpha}_p)}{\mathcal{L}(\boldsymbol{\theta}_i)p(\boldsymbol{\theta}_i|\boldsymbol{\alpha}_i)} = \frac{\frac{\mathcal{L}(\boldsymbol{\theta}_p)p(\boldsymbol{\theta}_p|\boldsymbol{\alpha}_p)}{p(\mathbf{x}|\boldsymbol{\alpha}_p)}}{\frac{\mathcal{L}(\boldsymbol{\theta}_i)p(\boldsymbol{\theta}_i|\boldsymbol{\alpha}_i)}{p(\boldsymbol{\theta}_i|\mathbf{x}, \boldsymbol{\alpha}_i)}} = \frac{p(\boldsymbol{\theta}_p|\mathbf{x}, \boldsymbol{\alpha}_p)}{p(\boldsymbol{\theta}_i|\mathbf{x}, \boldsymbol{\alpha}_i)} \quad (1.42)$$

so the probability a proposal is accepted is just the ratio of the posteriors of $\boldsymbol{\theta}_p$ and $\boldsymbol{\theta}_i$. In fact, Eq. ?? and Eq. 1.41 are just the ratio of the posteriors scaled by z^{n-1} and $(\|\boldsymbol{\theta}_p - \boldsymbol{\theta}_{r3}\|/\|\boldsymbol{\theta}_i - \boldsymbol{\theta}_{r3}\|)^{n-1}$, respectively - both of which reduce to Eq. 1.42 when $n = 1$.

The electron lifetime evolution MCMC uses 400 walkers for $n = 51$ parameters over 8000 iterations.

1.4.3 Results

With the electron lifetime evolution model described in Sec. 1.3 and the fit method in Sec. 1.4, the results are presented.

Parameters in the model (Eq. 1.34) that are assumed to be constant over the lifetime of the experiment are shown in Tab. 1.7. These values are not queried from the slow control system and are fixed in the fit. Some in fact may change slightly (e.g. M_G

1. PURITY AND THE ELECTRON LIFETIME

| Parameter | Value | Units | Comment |
|---------------------|----------------------|-----------------------------------|---|
| M_G | 23 | kg | GXe mass |
| M_L | 3157 | kg | LXe mass |
| ρ_{GXe} | 5.894 | g l^{-1} | GXe density |
| c_p | 158 | $\text{J kg}^{-1} \text{ K}^{-1}$ | Constant pressure specific heat of GXe, Sec. 1.3.3 |
| L | 9.5587×10^4 | J kg^{-1} | Latent heat of GXe, Sec. 1.3.3 |
| \dot{Q}_0 | 140 | W | GXe cooling power when $F_G = F_L = 0$, Sec. 1.3.3 |

Table 1.7: Parameters in the electron lifetime evolution model that are fixed.

| Parameter | Prior distribution | Units | Posterior | Comment |
|--------------------------|--------------------|-------|---------------------------|--|
| I_G^0 | ≥ 0 | ppb | 9951^{+8538}_{-6224} | Initial GXe impurity concentration |
| I_L^0 | ≥ 0 | ppb | $75.3^{+80.9}_{-58.2}$ | Initial LXe impurity concentration |
| ϵ_{vap} | 0-1 | — | $0.288^{+0.310}_{-0.214}$ | Probability of LXe impurity vaporization, Sec. 1.3.3 |
| ϵ_{cond} | 0-1 | — | $0.994^{+0.005}_{-0.015}$ | Probability of GXe impurity condensation, Sec. 1.3.3 |
| T_0 | -110-20 | °C | | Base temperature for condensation, Sec. 1.3.3 |

Table 1.8: Time-dependent parameters in fit.

and M_L during distillation) but are expected to have negligible effects. The cooling power when the circulation through the various XENON1T systems (Fig. ??) is zero \dot{Q}_0 was only measured in the beginning of the experiment (Sec. 1.3.3). Recalibrating would require halting the flow through the purification system, which would cause a drop in electron lifetime that would take weeks to recover. Therefore, \dot{Q}_0 has the lowest degree of certainty among the fixed values.

There are four free parameters that are time-invariant, i.e. their value is unchanging over the lifetime of the experiment. They are the initial (May 1, 2016) gas and liquid xenon impurity concentrations (I_G^0 and I_L^0 , respectively), probability of an impurity in the LXe to vaporize (ϵ_{vap}), and probability of an impurity in the GXe to condense (ϵ_{cond}). I_G and I_L are anti-correlated, since a larger initial impurity concentration in one implies a smaller concentration in the other.

The electron lifetime model is shown in Fig. 1.31. It matches the data well.

1.4.4 $^{83\text{m}}\text{Kr}$ Evolution

An separate electron lifetime trend is needed to describe the $^{83\text{m}}\text{Kr}$ measurements. Because the evolution of the trend is independent of the isotope used for the measure-

| Parameter | Prior distribution | Units | Start | Posterior | Comment |
|-----------|--------------------|--------------------------|------------------|---------------------------------------|--------------|
| A_G | ≥ 0 | ppb kg day^{-1} | May 1, 2016 | 321^{+77}_{-76} | Sec. 1.3.5.2 |
| | | | February 1, 2017 | $2.2^{+2.4}_{-1.6}$ | |
| | | | April 10, 2018 | $7.1^{+8.2}_{-4.5}$ | |
| | | | June 12, 2018 | $15.1^{+12.6}_{-9.7}$ | |
| β_1 | ≥ 0 | day^{-1} | May 1, 2016 | $0.0027^{+0.0020}_{-0.0014}$ | Sec. 1.3.5.2 |
| | | | February 1, 2017 | $0.0048^{+0.0053}_{-0.0035}$ | |
| | | | April 10, 2018 | $0.0086^{+0.0070}_{-0.0058}$ | |
| | | | June 12, 2018 | $0.0060^{+0.0067}_{-0.0038}$ | |
| β_2 | ≥ 0 | day^{-1} | May 1, 2016 | $5.37^{+10.2}_{-9.71} \times 10^{-4}$ | Sec. 1.3.5.2 |
| | | | February 1, 2017 | $0.0043^{+0.1382}_{-0.0750}$ | |
| | | | April 10, 2018 | $0.09^{+0.14}_{-0.10}$ | |
| | | | June 12, 2018 | $0.10^{+0.11}_{-0.10}$ | |
| A_L | ≥ 0 | ppb kg day^{-1} | May 1, 2016 | $49.3^{+28.5}_{-25.2}$ | Sec. 1.3.5.2 |
| | | | February 1, 2017 | $11.7^{+1.8}_{-1.8}$ | |
| | | | April 10, 2018 | $3.4^{+2.6}_{-2.3}$ | |
| | | | June 12, 2018 | $7.5^{+4.7}_{-4.3}$ | |
| β_3 | ≥ 0 | day^{-1} | May 1, 2016 | $0.0069^{+0.0053}_{-0.0051}$ | Sec. 1.3.5.2 |
| | | | February 1, 2017 | $0.0107^{+0.0017}_{-0.0016}$ | |
| | | | April 10, 2018 | $0.0031^{+0.0040}_{-0.0021}$ | |
| | | | June 12, 2018 | $0.0042^{+0.0053}_{-0.0028}$ | |
| β_4 | ≥ 0 | day^{-1} | May 1, 2016 | $0.0017^{+0.0046}_{-0.0052}$ | Sec. 1.3.5.2 |
| | | | February 1, 2017 | $0.00221^{+0.00076}_{-0.00053}$ | |
| | | | April 10, 2018 | $0.031^{+0.034}_{-0.027}$ | |
| | | | June 12, 2018 | $0.037^{+0.054}_{-0.040}$ | |
| R_I | ≥ 0 | ppb kg day^{-1} | May 1, 2016 | 170^{+64}_{-58} | Sec. 1.3.5.4 |
| | | | February 1, 2017 | $159.5^{+3.3}_{-2.3}$ | |
| | | | April 10, 2018 | $172.5^{+3.7}_{-3.5}$ | |
| | | | June 12, 2018 | $176.9^{+6.53}_{-6.7}$ | |

Table 1.9: Outgassing and leak medians and 68% credible intervals.

| Date | Prior distribution | Region | Posterior | Comment |
|----------------------|--------------------|--------|---------------------------|----------------------------|
| Aug. 22-Sep. 2, 2016 | 0-1 | GXE | $0.628^{+0.236}_{-0.333}$ | GXE-only purification |
| Aug. 22-Sep. 2, 2016 | 0-1 | LXE | $0.632^{+0.081}_{-0.118}$ | GXE-only purification |
| May 8-18, 2018 | 0-1 | GXE | $0.436^{+0.388}_{-0.328}$ | LN ₂ cooling |
| May 8-18, 2018 | 0-1 | LXE | $0.889^{+0.033}_{-0.031}$ | LN ₂ cooling |
| May 29-June 5, 2018 | ≥ 0 | GXE | $1.48^{+1.11}_{-1.04}$ | Circulation stopped |
| May 29-June 5, 2018 | 0-1 | LXE | $0.306^{+0.077}_{-0.064}$ | Circulation stopped |
| June 5-12, 2018 | ≥ 0 | LXE | $1.34^{+0.83}_{-0.79}$ | Magnetic pump installation |

Table 1.10: Fraction of outgassing during periods where system conditions changed. Medians and 68% credible intervals are listed, along with change in conditions.

1. PURITY AND THE ELECTRON LIFETIME

| Parameter | Date | Prior distribution | Posterior | Comment |
|------------|----------------------|--------------------|---------------------------|-------------------------------|
| α_1 | Nov. 26-Dec. 5, 2016 | 0-1 | $0.822^{+0.019}_{-0.018}$ | |
| α_2 | Dec. 19-21, 2016 | 0-1 | $0.687^{+0.208}_{-0.272}$ | ^{220}Rn calibration |
| α_3 | Oct. 25-30, 2017 | 0-1 | $0.979^{+0.014}_{-0.017}$ | ^{220}Rn calibration |

Table 1.11: Time-dependent parameters in fit.

| Date | Origin | Region | Possible cause | $\sim\tau_e$ [μs] | $\sim\Delta\tau_e$ [μs] | ΔI [ppb] |
|----------------------|----------------------|-----------|--|-------------------|-------------------------|------------------------|
| June 14, 2016 | Power glitch | GXe | PTR power \rightarrow 0 | 65 | -30 | $73.9^{+25.4}_{-29.5}$ |
| July 15, 2016 | LN ₂ test | GXe | PTR power \rightarrow 0 | 225* | -100 | $32.2^{+2.3}_{-2.6}$ |
| Nov. 21, 2016 | Power disruption | LXe | Temperature increase | 450 | -75 | $2.96^{+0.29}_{-0.26}$ |
| Jan. 18-Feb. 1, 2017 | Earthquake | GXe + LXe | Liquid level change | 520* | -120 | $2.57^{+0.21}_{-0.23}$ |
| June 5, 2017 | Gate washing | LXe | Liquid level change | 575 | -50 | $1.03^{+0.14}_{-0.14}$ |
| Feb. 21, 2018 | Power glitch | GXe | PTR power drop of $\sim 50\%$ | 600 | -150 | $3.79^{+0.11}_{-0.09}$ |
| Feb. 24, 2018 | Blackout | GXe + LXe | PTR power \rightarrow 0, $F_G = F_L = 0$ | 500* | -150 | $3.31^{+1.84}_{-1.76}$ |
| Mar. 5-7, 2018 | Gate washings | LXe | Liquid level change | 450 | -70 | $2.02^{+0.76}_{-0.78}$ |

Table 1.12: Impurity drops during XENON1T.

ment the alpha model will describe the ^{83m}Kr model if it can be adjusted upwards. The ratio between the two becomes larger at higher τ_e so scaling by a constant will not work. Fig. 1.32 shows the difference in electron lifetimes between ^{83m}Kr and the alpha model as a function of alpha model, where the values for the alpha model are from the trend at the times of the ^{83m}Kr measurements.

To determine which electron lifetime model should be used to correct background data the combined energy spectrum (Sec. ??) is examined. Fig. 1.33 shows the combined energy spectrum as a function of depth using both trends. The spectrum corrected with lifetimes from α -decays shows a shift to higher E at larger z , meaning it is over-corrected. The spectrum using ^{83m}Kr is consistent across the depth of the detector. This is not so surprising since the background is almost entirely electronic recoils.

At higher energies in Fig. 1.33 some of the mono-energetic lines begin to appear under-corrected. This is explained by Fig. 1.14 where the ^{60}Co (1173.2 keV) and ^{208}Tl (2614.5 keV) have higher charge yields than ^{129m}Xe and ^{131m}Xe so τ_e measurements would be lower. Correcting their S2s with the ^{83m}Kr values falls short. The effect is much smaller than using the α -decay trend, but for analyses using these high-energy lines the distortion would need to be fixed. Aside from using the electron lifetime, the

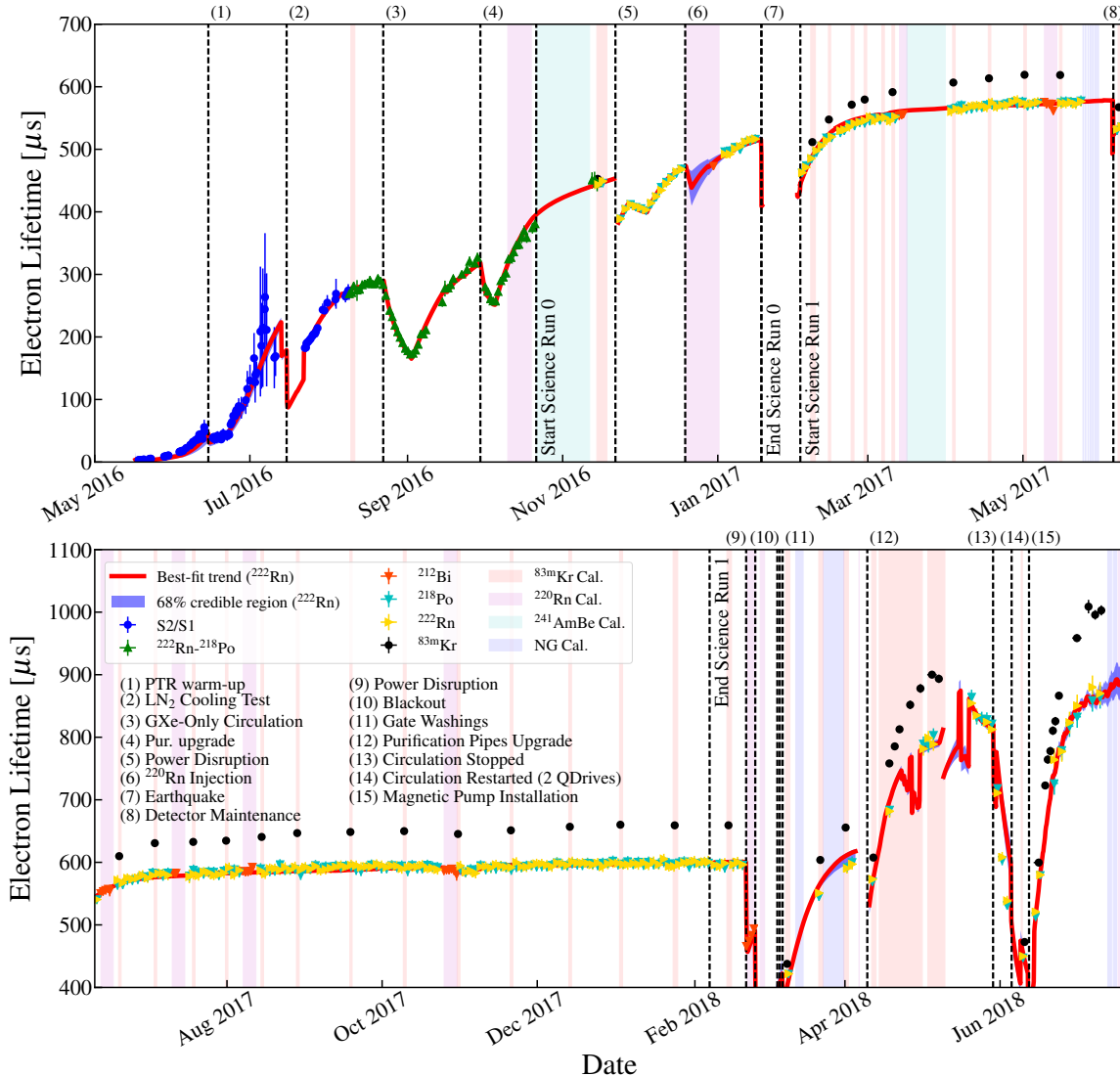


Figure 1.31: Electron lifetime model and data over the lifetime of XENON1T.

peaks can be corrected by minimizing their width if the underlying background is well understood and there are enough statistics. This would also result in a measurement of the electron lifetime.

Page 257 in Aprile book

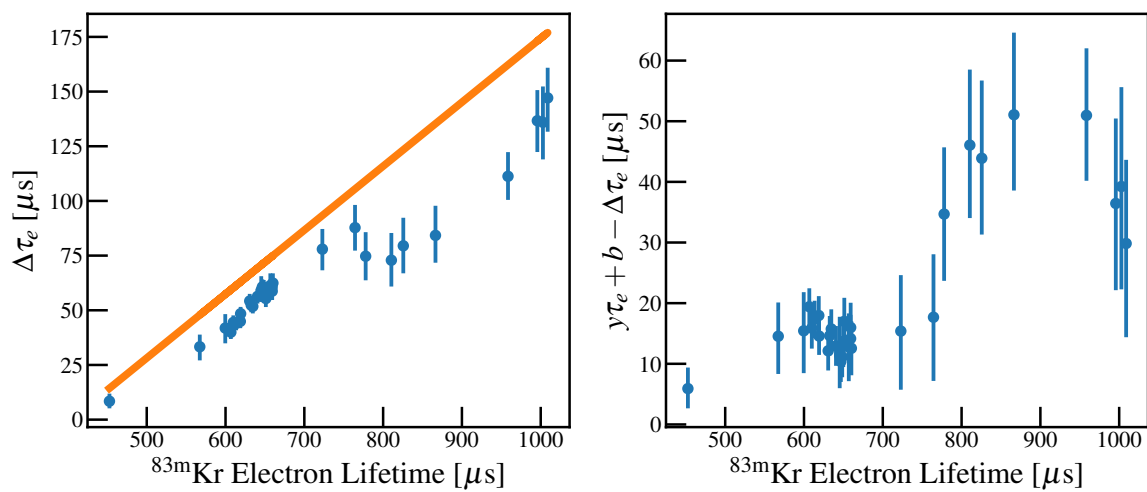


Figure 1.32: Adjustment of the electron lifetime fit to match $^{83\text{m}}\text{Kr}$. The left panel shows the $\Delta\tau_e$ ($\tau_e^{^{83\text{m}}\text{Kr}} - \tau_e^\alpha$) dependence on $\tau_e^{^{83\text{m}}\text{Kr}}$ where τ_e^α is the electron lifetime of the trend. Values from $^{83\text{m}}\text{Kr}$ measurements are marked in blue and the best-fit trend is shown in orange. The right panel shows the residuals of the left.

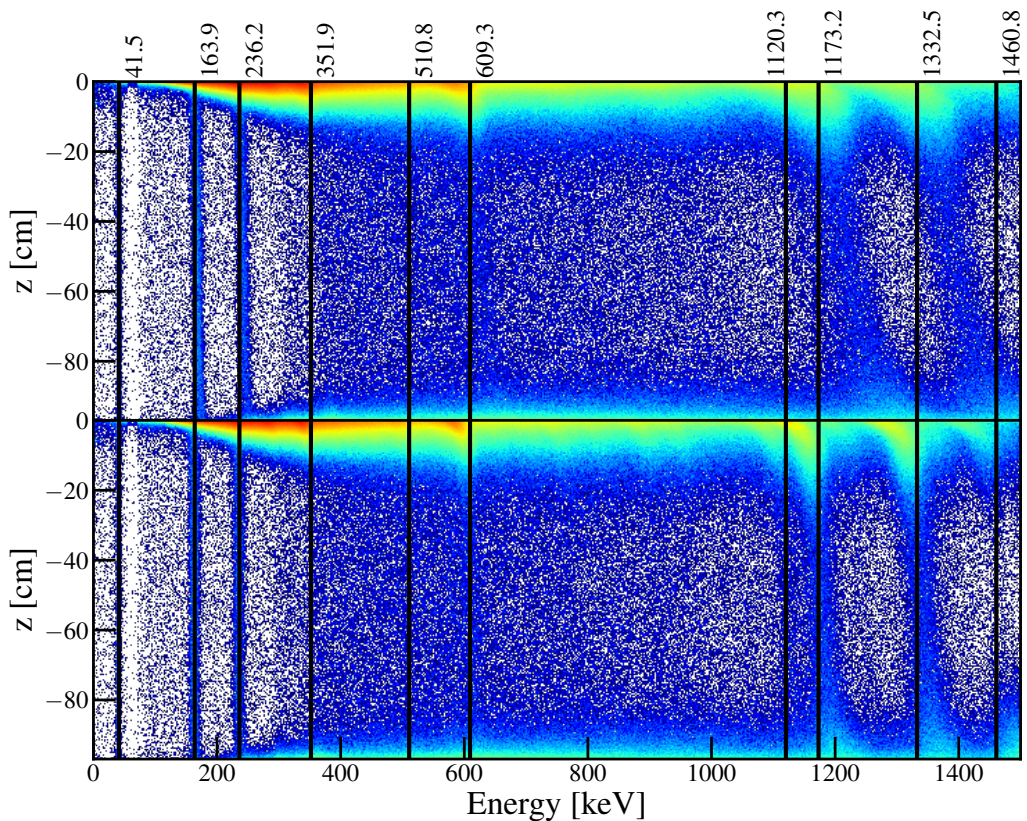


Figure 1.33: Combined energy spectrum over z for 0-1500 keV using the α -decay (top) and $^{83\text{m}}\text{Kr}$ (bottom) $S2_b$ corrections. For the α -corrected spectrum the monoenergetic peaks curve towards higher E deeper in the detector, indicating they are overcorrected. This occurs to an extent with the $^{83\text{m}}\text{Kr}$ -corrected spectrum at higher energy, but can be explained by the effects of an inhomogeneous electric field. Events near the top of the detector may saturate PMTs in the top array.

Bibliography

- [1] F. Zwicky, “Die Rotverschiebung von extragalaktischen Nebeln,” *Helvetica Physica Acta*, vol. 6, pp. 110–127, 1933.
- [2] V. C. Rubin and W. K. Ford Jr., “Rotation of the Andromeda Nebula from a Spectroscopic Survey of Emission Regions,” *The Astrophysical Journal*, vol. 159, p. 379, Feb. 1970. DOI: [10.1086/150317](https://doi.org/10.1086/150317).
- [3] K. G. Begeman, A. H. Broeils, and R. H. Sanders, “Extended rotation curves of spiral galaxies - Dark haloes and modified dynamics,” *MNRAS*, vol. 249, pp. 523–537, Apr. 1991. DOI: [10.1093/mnras/249.3.523](https://doi.org/10.1093/mnras/249.3.523).
- [4] Y. Sofue and V. Rubin, “Rotation Curves of Spiral Galaxies,” *Annual Review of Astronomy and Astrophysics*, vol. 39, pp. 137–174, 2001. DOI: [10.1146/annurev.astro.39.1.137](https://doi.org/10.1146/annurev.astro.39.1.137).
- [5] R. Gendler and the Subaru Telescope (NAOJ) and the Hubble Legacy Archive. (2013). NGC 6503, Spiral Galaxy in Draco, [Online]. Available: <http://www.robgendlerastropics.com/NGC6503-HST-Subaru.html> (visited on 08/10/2018).
- [6] NASA/JPL-Caltech/GSFC/SDSS. (May 2007). Dwarfs in Coma Cluster, [Online]. Available: <https://www.jpl.nasa.gov/spaceimages/details.php?id=PIA09561> (visited on 08/10/2018).
- [7] ESA/Hubble & NASA. (Dec. 2011). A Horseshoe Einstein Ring from Hubble, [Online]. Available: <https://apod.nasa.gov/apod/ap111221.html> (visited on 08/10/2018).
- [8] ALMA (NRAO/ESO/NAOJ)/Luis Calçada (ESO). (Jun. 2015). Gravitational lensing of distant star-forming galaxies (schematic), [Online]. Available: https://en.wikipedia.org/wiki/File:Gravitational_lensing_of_distant_star-forming_galaxies_schematic.png (visited on 08/10/2018).

BIBLIOGRAPHY

- [9] F. De Paolis, M. Giordano, G. Ingrosso, L. Manni, A. Nucita, and F. Strafella, “The Scales of Gravitational Lensing,” *Universe*, vol. 2, p. 6, Mar. 2016. DOI: [10.3390/universe2010006](https://doi.org/10.3390/universe2010006). arXiv: [1604.06601](https://arxiv.org/abs/1604.06601).
- [10] M. Markevitch, “Chandra Observation of the Most Interesting Cluster in the Universe,” in *The X-ray Universe 2005*, A. Wilson, Ed., ser. ESA Special Publication, vol. 604, Jan. 2006, p. 723. eprint: [astro-ph/0511345](https://arxiv.org/abs/astro-ph/0511345).
- [11] D. Clowe, M. Bradač, A. H. Gonzalez, M. Markevitch, S. W. Randall, C. Jones, and D. Zaritsky, “A Direct Empirical Proof of the Existence of Dark Matter,” *The Astrophysical Journal Letters*, vol. 648, pp. L109–L113, Sep. 2006. DOI: [10.1086/508162](https://doi.org/10.1086/508162).
- [12] M. Markevitch, A. H. Gonzalez, D. Clowe, A. Vikhlinin, W. Forman, C. Jones, S. Murray, and W. Tucker, “Direct Constraints on the Dark Matter Self-Interaction Cross Section from the Merging Galaxy Cluster 1E 0657-56,” *The Astrophysical Journal*, vol. 606, pp. 819–824, May 2004. DOI: [10.1086/383178](https://doi.org/10.1086/383178).
- [13] A. A. Penzias and R. W. Wilson, “A Measurement of Excess Antenna Temperature at 4080 Mc/s.,” *The Astrophysical Journal*, vol. 142, pp. 419–421, Jul. 1965. DOI: [10.1086/148307](https://doi.org/10.1086/148307).
- [14] D. J. Fixsen, “The Temperature of the Cosmic Microwave Background,” *The Astrophysical Journal*, vol. 707, pp. 916–920, Dec. 2009. DOI: [10.1088/0004-637X/707/2/916](https://doi.org/10.1088/0004-637X/707/2/916). arXiv: [0911.1955](https://arxiv.org/abs/0911.1955).
- [15] G. F. Smoot *et al.*, “First results of the COBE satellite measurement of the anisotropy of the cosmic microwave background radiation,” *Advances in Space Research*, vol. 11, pp. 193–205, 1991. DOI: [10.1016/0273-1177\(91\)90490-B](https://doi.org/10.1016/0273-1177(91)90490-B).
- [16] R. K. Sachs and A. M. Wolfe, “Perturbations of a Cosmological Model and Angular Variations of the Microwave Background,” *The Astrophysical Journal*, vol. 147, p. 73, Jan. 1967. DOI: [10.1086/148982](https://doi.org/10.1086/148982).
- [17] S. Dodelson, *Modern Cosmology*. Elsevier, 2003, vol. A volume in International Series of Monographs in Electronics and Instrumentation, ISBN: 978-0-12-219141-1.
- [18] Planck Collaboration. (2015). Map of CMB temperature from SMICA, [Online]. Available: <https://www.cosmos.esa.int/web/planck/picture-gallery> (visited on 01/18/2018).

-
- [19] P. A. R. Ade *et al.*, “Planck early results. I. The Planck mission,” *Astronomy & Astrophysics*, vol. 536, A1, A1, Dec. 2011. DOI: [10.1051/0004-6361/201116464](https://doi.org/10.1051/0004-6361/201116464). arXiv: [1101.2022 \[astro-ph.IM\]](https://arxiv.org/abs/1101.2022).
 - [20] ——, “Planck 2015 results. XIII. Cosmological parameters,” *Astronomy & Astrophysics*, vol. 594, A13, A13, Sep. 2016. DOI: [10.1051/0004-6361/201525830](https://doi.org/10.1051/0004-6361/201525830). arXiv: [1502.01589](https://arxiv.org/abs/1502.01589).
 - [21] R. D. Peccei and H. R. Quinn, “CP conservation in the presence of pseudoparticles,” *Physical Review Letters*, vol. 38, pp. 1440–1443, Jun. 1977. DOI: [10.1103/PhysRevLett.38.1440](https://doi.org/10.1103/PhysRevLett.38.1440).
 - [22] J. Preskill, M. B. Wise, and F. Wilczek, “Cosmology of the invisible axion,” *Physical Letters B*, vol. 120, pp. 127–132, Jan. 1983. DOI: [10.1016/0370-2693\(83\)90637-8](https://doi.org/10.1016/0370-2693(83)90637-8).
 - [23] J. E. Kim, “Weak-Interaction Singlet and Strong CP Invariance,” *Physical Review Letters*, vol. 43, pp. 103–107, 2 1979. DOI: [10.1103/PhysRevLett.43.103](https://doi.org/10.1103/PhysRevLett.43.103).
 - [24] M. A. Shifman, A. I. Vainshtein, and V. I. Zakharov, “Can confinement ensure natural CP invariance of strong interactions?” *Nuclear Physics B*, vol. 166, no. 3, pp. 493–506, Apr. 1980, ISSN: 0550-3213. DOI: [10.1016/0550-3213\(80\)90209-6](https://doi.org/10.1016/0550-3213(80)90209-6).
 - [25] A. R. Zhitnitsky, “On Possible Suppression of the Axion Hadron Interactions,” *Soviet Journal of Nuclear Physics*, vol. 31, pp. 260–263, 1980. [Online]. Available: <http://inspirehep.net/record/157263?ln=en>.
 - [26] M. Dine, W. Fischler, and M. Srednicki, “A simple solution to the strong CP problem with a harmless axion,” *Physical Letters B*, vol. 104, no. 3, pp. 199 –202, 1981, ISSN: 0370-2693. DOI: [10.1016/0370-2693\(81\)90590-6](https://doi.org/10.1016/0370-2693(81)90590-6).
 - [27] C. Patrignani and P. D. Group, “Review of Particle Physics,” *Chinese Physics C*, vol. 40, no. 10, p. 100001, 2016. [Online]. Available: <http://stacks.iop.org/1674-1137/40/i=10/a=100001>.
 - [28] H. Primakoff, “Photo-Production of Neutral Mesons in Nuclear Electric Fields and the Mean Life of the Neutral Meson,” *Physical Review*, vol. 81, pp. 899–899, 5 1951. DOI: [10.1103/PhysRev.81.899](https://doi.org/10.1103/PhysRev.81.899).
 - [29] N. Du *et al.*, “Search for invisible axion dark matter with the axion dark matter experiment,” *Physical Review Letters*, vol. 120, p. 151301, 15 2018. DOI: [10.1103/PhysRevLett.120.151301](https://doi.org/10.1103/PhysRevLett.120.151301).

- [30] V. Anastassopoulos *et al.*, “New CAST limit on the axion-photon interaction,” *Nature Physics*, vol. 13, pp. 584–590, Jun. 2017. DOI: [10.1038/nphys4109](https://doi.org/10.1038/nphys4109).
- [31] A. Garcon *et al.*, “The cosmic axion spin precession experiment (CASPER): a dark-matter search with nuclear magnetic resonance,” *Quantum Science and Technology*, vol. 3, no. 1, p. 014008, Jan. 2018. DOI: [10.1088/2058-9565/aa9861](https://doi.org/10.1088/2058-9565/aa9861). arXiv: [1707.05312 \[physics.ins-det\]](https://arxiv.org/abs/1707.05312).
- [32] Z. Ahmed *et al.*, “Search for Axions with the CDMS Experiment,” *Physical Review Letters*, vol. 103, no. 14, 141802, p. 141802, Oct. 2009. DOI: [10.1103/PhysRevLett.103.141802](https://doi.org/10.1103/PhysRevLett.103.141802). arXiv: [0902.4693 \[hep-ex\]](https://arxiv.org/abs/0902.4693).
- [33] E. Armengaud *et al.*, “Axion searches with the EDELWEISS-II experiment,” *JCAP*, vol. 11, 067, p. 067, Nov. 2013. DOI: [10.1088/1475-7516/2013/11/067](https://doi.org/10.1088/1475-7516/2013/11/067). arXiv: [1307.1488](https://arxiv.org/abs/1307.1488).
- [34] K. Abe *et al.*, “Search for solar axions in XMASS, a large liquid-xenon detector,” *Physical Letters B*, vol. 724, pp. 46–50, Jul. 2013. DOI: [10.1016/j.physletb.2013.05.060](https://doi.org/10.1016/j.physletb.2013.05.060). arXiv: [1212.6153 \[astro-ph.CO\]](https://arxiv.org/abs/1212.6153).
- [35] E. Aprile *et al.*, “First axion results from the XENON100 experiment,” *Physical Review D*, vol. 90, no. 6, 062009, p. 062009, Sep. 2014. DOI: [10.1103/PhysRevD.90.062009](https://doi.org/10.1103/PhysRevD.90.062009). arXiv: [1404.1455](https://arxiv.org/abs/1404.1455).
- [36] B. Ryden, *Introduction to Cosmology*. Addison Wesley, 2003.
- [37] B. Moore, S. Ghigna, F. Governato, G. Lake, T. Quinn, J. Stadel, and P. Tozzi, “Dark Matter Substructure within Galactic Halos,” *The Astrophysical Journal Letters*, vol. 524, pp. L19–L22, Oct. 1999. DOI: [10.1086/312287](https://doi.org/10.1086/312287).
- [38] A. Klypin, A. V. Kravtsov, O. Valenzuela, and F. Prada, “Where Are the Missing Galactic Satellites?” *The Astrophysical Journal*, vol. 522, pp. 82–92, Sep. 1999. DOI: [10.1086/307643](https://doi.org/10.1086/307643).
- [39] J. D. Simon and M. Geha, “The Kinematics of the Ultra-faint Milky Way Satellites: Solving the Missing Satellite Problem,” *The Astrophysical Journal*, vol. 670, pp. 313–331, Nov. 2007. DOI: [10.1086/521816](https://doi.org/10.1086/521816). arXiv: [0706.0516](https://arxiv.org/abs/0706.0516).
- [40] J. S. Bullock and M. Boylan-Kolchin, “Small-Scale Challenges to the Λ CDM Paradigm,” *Annual Review of Astronomy and Astrophysics*, vol. 55, pp. 343–387, Aug. 2017. DOI: [10.1146/annurev-astro-091916-055313](https://doi.org/10.1146/annurev-astro-091916-055313). arXiv: [1707.04256](https://arxiv.org/abs/1707.04256).

-
- [41] G. Ogiya and O. Hahn, “What sets the central structure of dark matter haloes?” *MNRAS*, vol. 473, pp. 4339–4359, Feb. 2018. DOI: [10.1093/mnras/stx2639](https://doi.org/10.1093/mnras/stx2639). arXiv: [1707.07693](https://arxiv.org/abs/1707.07693).
 - [42] P. van Dokkum *et al.*, “A galaxy lacking dark matter,” *Nature*, vol. 555, pp. 629–632, Mar. 2018. DOI: [10.1038/nature25767](https://doi.org/10.1038/nature25767). arXiv: [1803.10237](https://arxiv.org/abs/1803.10237).
 - [43] ——, “An Enigmatic Population of Luminous Globular Clusters in a Galaxy Lacking Dark Matter,” *The Astrophysical Journal Letters*, vol. 856, L30, p. L30, Apr. 2018. DOI: [10.3847/2041-8213/aab60b](https://doi.org/10.3847/2041-8213/aab60b). arXiv: [1803.10240](https://arxiv.org/abs/1803.10240).
 - [44] M. Milgrom, “A modification of the Newtonian dynamics as a possible alternative to the hidden mass hypothesis,” *The Astrophysical Journal*, vol. 270, pp. 365–370, Jul. 1983. DOI: [10.1086/161130](https://doi.org/10.1086/161130).
 - [45] B. Famaey, S. McGaugh, and M. Milgrom, “MOND and the dynamics of NGC1052-DF2,” *arXiv e-prints*, Apr. 2018. arXiv: [1804.04167](https://arxiv.org/abs/1804.04167).
 - [46] J. W. Moffat and V. T. Toth, “NGC 1052-DF2 And Modified Gravity (MOG) Without Dark Matter,” *arXiv e-prints*, May 2018. arXiv: [1805.01117 \[gr-qc\]](https://arxiv.org/abs/1805.01117).
 - [47] R. Abraham *et al.*, “The Maybe Stream: A Possible Cold Stellar Stream in the Ultra-diffuse Galaxy NGC1052-DF2,” *Research Notes of the American Astronomical Society*, vol. 2, 16, p. 16, May 2018. DOI: [10.3847/2515-5172/aac087](https://doi.org/10.3847/2515-5172/aac087).
 - [48] G. Ogiya, “Tidal stripping as a possible origin of the ultra diffuse galaxy lacking dark matter,” *arXiv e-prints*, Apr. 2018. arXiv: [1804.06421](https://arxiv.org/abs/1804.06421).
 - [49] F. Lelli, S. S. McGaugh, and J. M. Schombert, “SPARC: Mass Models for 175 Disk Galaxies with Spitzer Photometry and Accurate Rotation Curves,” *The Astronomical Journal*, vol. 152, 157, p. 157, Dec. 2016. DOI: [10.3847/0004-6256/152/6/157](https://doi.org/10.3847/0004-6256/152/6/157). arXiv: [1606.09251](https://arxiv.org/abs/1606.09251).
 - [50] P. Li, F. Lelli, S. McGaugh, and J. Schombert, “Fitting the Radial Acceleration Relation to Individual SPARC Galaxies,” *arXiv e-prints*, Feb. 2018. arXiv: [1803.00022](https://arxiv.org/abs/1803.00022).
 - [51] W. J. G. de Blok, F. Walter, E. Brinks, C. Trachternach, S.-H. Oh, and R. C. Kennicutt Jr., “High-Resolution Rotation Curves and Galaxy Mass Models from THINGS,” *The Astronomical Journal*, vol. 136, pp. 2648–2719, Dec. 2008. DOI: [10.1088/0004-6256/136/6/2648](https://doi.org/10.1088/0004-6256/136/6/2648). arXiv: [0810.2100](https://arxiv.org/abs/0810.2100).

- [52] D. C. Rodrigues, V. Marra, A. del Popolo, and Z. Davari, “Absence of a fundamental acceleration scale in galaxies,” *Nature Astronomy*, Jun. 2018. DOI: [10.1038/s41550-018-0498-9](https://doi.org/10.1038/s41550-018-0498-9). arXiv: [1806.06803](https://arxiv.org/abs/1806.06803).
- [53] X.-J. Bi, P.-F. Yin, and Q. Yuan, “Status of dark matter detection,” *Frontiers of Physics*, vol. 8, pp. 794–827, Dec. 2013. DOI: [10.1007/s11467-013-0330-z](https://doi.org/10.1007/s11467-013-0330-z). arXiv: [1409.4590 \[hep-ph\]](https://arxiv.org/abs/1409.4590).
- [54] P. J. Fox, R. Harnik, J. Kopp, and Y. Tsai, “LEP shines light on dark matter,” *Physical Review D*, vol. 84, no. 1, 014028, p. 014 028, Jul. 2011. DOI: [10.1103/PhysRevD.84.014028](https://doi.org/10.1103/PhysRevD.84.014028). arXiv: [1103.0240 \[hep-ph\]](https://arxiv.org/abs/1103.0240).
- [55] C. Alpigiani, “Searches for Dark Matter in ATLAS,” *arXiv e-prints*, Aug. 2017. arXiv: [1708.09674 \[hep-ex\]](https://arxiv.org/abs/1708.09674).
- [56] CERN. (2015). LHC experiments join forces to zoom in on the Higgs boson, [Online]. Available: <https://home.cern/about/updates/2015/03/lhc-experiments-join-forces-zoom-higgs> (visited on 08/09/2018).
- [57] J. I. Read, “The local dark matter density,” *Journal of Physics G*, vol. 41, no. 6, 063101, p. 063 101, Jun. 2014. DOI: [10.1088/0954-3899/41/6/063101](https://doi.org/10.1088/0954-3899/41/6/063101). arXiv: [1404.1938](https://arxiv.org/abs/1404.1938).
- [58] J. Ellis, R. A. Flores, K. Freese, S. Ritz, D. Seckel, and J. Silk, “Cosmic ray constraints on the annihilations of relic particles in the galactic halo,” *Physical Letters B*, vol. 214, pp. 403–412, Nov. 1988. DOI: [10.1016/0370-2693\(88\)91385-8](https://doi.org/10.1016/0370-2693(88)91385-8).
- [59] B. Zitzer *et al.*, “A Search for Dark Matter from Dwarf Galaxies using VERITAS,” in *Proceedings of the 38th International Conference on High Energy Physics (ICHEP2016). 3-10 August 2016. Chicago, USA.*, 2016, p. 446. arXiv: [1509.01105 \[astro-ph.HE\]](https://arxiv.org/abs/1509.01105).
- [60] G. Bertone, D. Hooper, and J. Silk, “Particle dark matter: evidence, candidates and constraints,” *Physical Reports*, vol. 405, pp. 279–390, Jan. 2005. DOI: [10.1016/j.physrep.2004.08.031](https://doi.org/10.1016/j.physrep.2004.08.031).
- [61] J. Kopp, V. Niro, T. Schwetz, and J. Zupan, “DAMA/LIBRA data and leptonically interacting dark matter,” *Physical Review D*, vol. 80, no. 8, 083502, p. 083 502, Oct. 2009. DOI: [10.1103/PhysRevD.80.083502](https://doi.org/10.1103/PhysRevD.80.083502). arXiv: [0907.3159 \[hep-ph\]](https://arxiv.org/abs/0907.3159).
- [62] P. Bhattacharjee, S. Chaudhury, S. Kundu, and S. Majumdar, “Deriving the velocity distribution of Galactic dark matter particles from the rotation curve

- data,” *Physical Review D*, vol. 87, no. 8, 083525, p. 083 525, Apr. 2013. DOI: [10.1103/PhysRevD.87.083525](https://doi.org/10.1103/PhysRevD.87.083525). arXiv: [1210.2328 \[astro-ph.GA\]](https://arxiv.org/abs/1210.2328).
- [63] J. Diemand, B. Moore, and J. Stadel, “Velocity and spatial biases in cold dark matter subhalo distributions,” *MNRAS*, vol. 352, pp. 535–546, Aug. 2004. DOI: [10.1111/j.1365-2966.2004.07940.x](https://doi.org/10.1111/j.1365-2966.2004.07940.x).
- [64] M. Kuhlen *et al.*, “Dark matter direct detection with non-Maxwellian velocity structure,” *JCAP*, vol. 2, 030, p. 030, Feb. 2010. DOI: [10.1088/1475-7516/2010/02/030](https://doi.org/10.1088/1475-7516/2010/02/030). arXiv: [0912.2358](https://arxiv.org/abs/0912.2358).
- [65] T. Marrodán Undagoitia and L. Rauch, “Dark matter direct-detection experiments,” *Journal of Physics G*, vol. 43, no. 1, 013001, p. 013 001, Jan. 2016. DOI: [10.1088/0954-3899/43/1/013001](https://doi.org/10.1088/0954-3899/43/1/013001). arXiv: [1509.08767 \[physics.ins-det\]](https://arxiv.org/abs/1509.08767).
- [66] T. Piffl *et al.*, “The RAVE survey: the Galactic escape speed and the mass of the Milky Way,” *Astronomy & Astrophysics*, vol. 562, A91, A91, Feb. 2014. DOI: [10.1051/0004-6361/201322531](https://doi.org/10.1051/0004-6361/201322531). arXiv: [1309.4293 \[astro-ph.GA\]](https://arxiv.org/abs/1309.4293).
- [67] J. D. Lewin and P. F. Smith, “Review of mathematics, numerical factors, and corrections for dark matter experiments based on elastic nuclear recoil,” *Astroparticle Physics*, vol. 6, pp. 87–112, Dec. 1996. DOI: [10.1016/S0927-6505\(96\)00047-3](https://doi.org/10.1016/S0927-6505(96)00047-3).
- [68] R. H. Helm, “Inelastic and elastic scattering of 187-mev electrons from selected even-even nuclei,” *Physical Review*, vol. 104, pp. 1466–1475, 5 1956. DOI: [10.1103/PhysRev.104.1466](https://doi.org/10.1103/PhysRev.104.1466).
- [69] J. Engel, “Nuclear form factors for the scattering of weakly interacting massive particles,” *Physical Letters B*, vol. 264, no. 1, pp. 114 –119, 1991, ISSN: 0370-2693. DOI: [10.1016/0370-2693\(91\)90712-Y](https://doi.org/10.1016/0370-2693(91)90712-Y).
- [70] C. E. Yaguna, “Isospin-violating dark matter in the light of recent data,” *Physical Review D*, vol. 95, no. 5, 055015, p. 055 015, Mar. 2017. DOI: [10.1103/PhysRevD.95.055015](https://doi.org/10.1103/PhysRevD.95.055015). arXiv: [1610.08683 \[hep-ph\]](https://arxiv.org/abs/1610.08683).
- [71] A. K. Drukier, K. Freese, and D. N. Spergel, “Detecting cold dark-matter candidates,” *Physical Review D*, vol. 33, pp. 3495–3508, Jun. 1986. DOI: [10.1103/PhysRevD.33.3495](https://doi.org/10.1103/PhysRevD.33.3495).
- [72] K. Freese, M. Lisanti, and C. Savage, “Colloquium: Annual modulation of dark matter,” *Review of Modern Physics*, vol. 85, pp. 1561–1581, Oct. 2013. DOI: [10.1103/RevModPhys.85.1561](https://doi.org/10.1103/RevModPhys.85.1561). arXiv: [1209.3339](https://arxiv.org/abs/1209.3339).

- [73] C. Amole *et al.*, “Dark Matter Search Results from the PICO-60 C_3F_8 Bubble Chamber,” *Physical Review Letters*, vol. 118, no. 25, 251301, p. 251 301, Jun. 2017. DOI: [10.1103/PhysRevLett.118.251301](https://doi.org/10.1103/PhysRevLett.118.251301). arXiv: [1702.07666](https://arxiv.org/abs/1702.07666).
- [74] J. Ellis and R. A. Flores, “Elastic supersymmetric relic-nucleus scattering revisited,” *Physical Letters B*, vol. 263, pp. 259–266, Jul. 1991. DOI: [10.1016/0370-2693\(91\)90597-J](https://doi.org/10.1016/0370-2693(91)90597-J).
- [75] S. Archambault *et al.*, “Constraints on low-mass WIMP interactions on ^{19}F from PICASSO,” *Physical Letters B*, vol. 711, pp. 153–161, May 2012. DOI: [10.1016/j.physletb.2012.03.078](https://doi.org/10.1016/j.physletb.2012.03.078). arXiv: [1202.1240 \[hep-ex\]](https://arxiv.org/abs/1202.1240).
- [76] E. Behnke *et al.*, “Final results of the PICASSO dark matter search experiment,” *Astroparticle Physics*, vol. 90, pp. 85–92, Apr. 2017. DOI: [10.1016/j.astropartphys.2017.02.005](https://doi.org/10.1016/j.astropartphys.2017.02.005). arXiv: [1611.01499 \[hep-ex\]](https://arxiv.org/abs/1611.01499).
- [77] ——, “First dark matter search results from a 4-kg CF_3I bubble chamber operated in a deep underground site,” *Physical Review D*, vol. 86, no. 5, 052001, p. 052 001, Sep. 2012. DOI: [10.1103/PhysRevD.86.052001](https://doi.org/10.1103/PhysRevD.86.052001). arXiv: [1204.3094 \[astro-ph.CO\]](https://arxiv.org/abs/1204.3094).
- [78] M. Felizardo *et al.*, “Final Analysis and Results of the Phase II SIMPLE Dark Matter Search,” *Physical Review Letters*, vol. 108, no. 20, 201302, p. 201 302, May 2012. DOI: [10.1103/PhysRevLett.108.201302](https://doi.org/10.1103/PhysRevLett.108.201302). arXiv: [1106.3014](https://arxiv.org/abs/1106.3014).
- [79] A. Antonicci *et al.*, “MOSCAB: A geyser-concept bubble chamber to be used in a dark matter search,” *arXiv e-prints*, Jul. 2017. arXiv: [1708.00101 \[physics.ins-det\]](https://arxiv.org/abs/1708.00101).
- [80] C. Amole *et al.*, “Dark matter search results from the PICO-60 CF_3I bubble chamber,” *Physical Review D*, vol. 93, no. 5, 052014, p. 052 014, Mar. 2016. DOI: [10.1103/PhysRevD.93.052014](https://doi.org/10.1103/PhysRevD.93.052014). arXiv: [1510.07754 \[hep-ex\]](https://arxiv.org/abs/1510.07754).
- [81] ——, “Improved dark matter search results from PICO-2L Run 2,” *Physical Review D*, vol. 93, no. 6, 061101, p. 061 101, Mar. 2016. DOI: [10.1103/PhysRevD.93.061101](https://doi.org/10.1103/PhysRevD.93.061101). arXiv: [1601.03729](https://arxiv.org/abs/1601.03729).
- [82] M. Felizardo *et al.*, “The SIMPLE Phase II dark matter search,” *Physical Review D*, vol. 89, no. 7, 072013, p. 072 013, Apr. 2014. DOI: [10.1103/PhysRevD.89.072013](https://doi.org/10.1103/PhysRevD.89.072013). arXiv: [1404.4309 \[hep-ph\]](https://arxiv.org/abs/1404.4309).
- [83] C. Fu *et al.*, “Spin-Dependent Weakly-Interacting-Massive-Particle-Nucleon Cross Section Limits from First Data of PandaX-II Experiment,” *Physical Review Letters*, vol. 118, no. 7, 071301, p. 071 301, Feb. 2017. DOI: [10.1103/PhysRevLett.118.071301](https://doi.org/10.1103/PhysRevLett.118.071301). arXiv: [1611.06553 \[hep-ex\]](https://arxiv.org/abs/1611.06553).

-
- [84] M. G. Aartsen *et al.*, “Search for annihilating dark matter in the Sun with 3 years of IceCube data,” *The European Physical Journal C*, vol. 77, 146, p. 146, Mar. 2017. DOI: [10.1140/epjc/s10052-017-4689-9](https://doi.org/10.1140/epjc/s10052-017-4689-9). arXiv: [1612.05949 \[astro-ph.HE\]](https://arxiv.org/abs/1612.05949).
 - [85] T. Tanaka *et al.*, “An Indirect Search for Weakly Interacting Massive Particles in the Sun Using 3109.6 Days of Upward-going Muons in Super-Kamiokande,” *The Astrophysical Journal*, vol. 742, 78, p. 78, Dec. 2011. DOI: [10.1088/0004-637X/742/2/78](https://doi.org/10.1088/0004-637X/742/2/78). arXiv: [1108.3384 \[astro-ph.HE\]](https://arxiv.org/abs/1108.3384).
 - [86] K. Choi *et al.*, “Search for Neutrinos from Annihilation of Captured Low-Mass Dark Matter Particles in the Sun by Super-Kamiokande,” *Physical Review Letters*, vol. 114, no. 14, 141301, p. 141301, Apr. 2015. DOI: [10.1103/PhysRevLett.114.141301](https://doi.org/10.1103/PhysRevLett.114.141301).
 - [87] L. Roszkowski, R. Ruiz de Austri, and R. Trotta, “Implications for the Constrained MSSM from a new prediction for $b \rightarrow s\gamma$,” *Journal of High Energy Physics*, vol. 7, 075, p. 075, Jul. 2007. DOI: [10.1088/1126-6708/2007/07/075](https://doi.org/10.1088/1126-6708/2007/07/075). arXiv: [0705.2012 \[hep-ph\]](https://arxiv.org/abs/0705.2012).
 - [88] R. Bernabei *et al.*, “The DAMA/LIBRA apparatus,” *Nuclear Instruments and Methods in Physics Research A*, vol. 592, pp. 297–315, Jul. 2008. DOI: [10.1016/j.nima.2008.04.082](https://doi.org/10.1016/j.nima.2008.04.082). arXiv: [0804.2738](https://arxiv.org/abs/0804.2738).
 - [89] E. Shields, J. Xu, and F. Calaprice, “SABRE: A New NaI(Tl) Dark Matter Direct Detection Experiment,” *Physics Procedia*, vol. 61, pp. 169–178, 2015. DOI: [10.1016/j.phpro.2014.12.028](https://doi.org/10.1016/j.phpro.2014.12.028).
 - [90] R. Bernabei *et al.*, “DAMA/LIBRA results and perspectives,” *arXiv e-prints*, Jan. 2013. arXiv: [1301.6243 \[astro-ph.GA\]](https://arxiv.org/abs/1301.6243).
 - [91] ——, “Final model independent result of DAMA/LIBRA-phase1,” *The European Physical Journal C*, vol. 73, 2648, p. 2648, Dec. 2013. DOI: [10.1140/epjc/s10052-013-2648-7](https://doi.org/10.1140/epjc/s10052-013-2648-7). arXiv: [1308.5109](https://arxiv.org/abs/1308.5109).
 - [92] R. Bernabei *et al.*, “Investigating the DAMA annual modulation data in a mixed coupling framework,” *Physical Letters B*, vol. 509, no. 3, pp. 197–203, 2001, ISSN: 0370-2693. DOI: [10.1016/S0370-2693\(01\)00493-2](https://doi.org/10.1016/S0370-2693(01)00493-2).
 - [93] R. Bernabei *et al.*, “Investigating the DAMA annual modulation data in the framework of inelastic dark matter,” *The European Physical Journal C*, vol. 23, pp. 61–64, Mar. 2002. DOI: [10.1007/s100520100854](https://doi.org/10.1007/s100520100854).

- [94] ——, “Investigating Pseudoscalar and Scalar Dark Matter,” *International Journal of Modern Physics A*, vol. 21, pp. 1445–1469, 2006. DOI: [10.1142/S0217751X06030874](https://doi.org/10.1142/S0217751X06030874).
- [95] E. Aprile *et al.*, “Search for Electronic Recoil Event Rate Modulation with 4 Years of XENON100 Data,” *Physical Review Letters*, vol. 118, p. 101 101, 10 2017. DOI: [10.1103/PhysRevLett.118.101101](https://doi.org/10.1103/PhysRevLett.118.101101).
- [96] K. Blum, “DAMA vs. the annually modulated muon background,” *ArXiv e-prints*, Oct. 2011. arXiv: [1110.0857 \[astro-ph.HE\]](https://arxiv.org/abs/1110.0857).
- [97] J. P. Ralston, “One Model Explains DAMA/LIBRA, CoGENT, CDMS, and XENON,” *ArXiv e-prints*, Jun. 2010. arXiv: [1006.5255 \[hep-ph\]](https://arxiv.org/abs/1006.5255).
- [98] J. H. Davis, “Fitting the Annual Modulation in DAMA with Neutrons from Muons and Neutrinos,” *Physical Review Letters*, vol. 113, no. 8, 081302, p. 081302, Aug. 2014. DOI: [10.1103/PhysRevLett.113.081302](https://doi.org/10.1103/PhysRevLett.113.081302). arXiv: [1407.1052 \[hep-ph\]](https://arxiv.org/abs/1407.1052).
- [99] P. S. Barbeau, J. I. Collar, Y. Efremenko, and K. Scholberg, “Comment on “Fitting the Annual Modulation in DAMA with Neutrons from Muons and Neutrinos”,” *Physical Review Letters*, vol. 113, no. 22, 229001, p. 229 001, Nov. 2014. DOI: [10.1103/PhysRevLett.113.229001](https://doi.org/10.1103/PhysRevLett.113.229001). arXiv: [1409.3185 \[hep-ph\]](https://arxiv.org/abs/1409.3185).
- [100] J. Klinger and V. A. Kudryavtsev, “Muon-Induced Neutrons Do Not Explain the DAMA Data,” *Physical Review Letters*, vol. 114, no. 15, 151301, p. 151 301, Apr. 2015. DOI: [10.1103/PhysRevLett.114.151301](https://doi.org/10.1103/PhysRevLett.114.151301). arXiv: [1503.07225 \[hep-ph\]](https://arxiv.org/abs/1503.07225).
- [101] G. D’Imperio *et al.*, “Dark matter search with the SABRE experiment,” *arXiv e-prints*, Jul. 2018. arXiv: [1807.00584 \[physics.ins-det\]](https://arxiv.org/abs/1807.00584).
- [102] D. Hooper, J. I. Collar, J. Hall, D. McKinsey, and C. M. Kelso, “Consistent dark matter interpretation for CoGeNT and DAMA/LIBRA,” *Physical Review D*, vol. 82, no. 12, 123509, p. 123 509, Dec. 2010. DOI: [10.1103/PhysRevD.82.123509](https://doi.org/10.1103/PhysRevD.82.123509). arXiv: [1007.1005 \[hep-ph\]](https://arxiv.org/abs/1007.1005).
- [103] C. E. Aalseth *et al.*, “Search for An Annual Modulation in Three Years of CoGeNT Dark Matter Detector Data,” *ArXiv e-prints*, Jan. 2014. arXiv: [1401.3295 \[astro-ph.CO\]](https://arxiv.org/abs/1401.3295).
- [104] ——, “Maximum Likelihood Signal Extraction Method Applied to 3.4 years of CoGeNT Data,” *arXiv e-prints*, Jan. 2014. arXiv: [1401.6234](https://arxiv.org/abs/1401.6234).

-
- [105] J. H. Davis, C. McCabe, and C. Boehm, “Quantifying the evidence for dark matter in CoGeNT data,” *JCAP*, vol. 8, 014, p. 014, Aug. 2014. DOI: [10.1088/1475-7516/2014/08/014](https://doi.org/10.1088/1475-7516/2014/08/014). arXiv: [1405.0495 \[hep-ph\]](https://arxiv.org/abs/1405.0495).
 - [106] Q. Yue *et al.*, “Limits on light weakly interacting massive particles from the CDEX-1 experiment with a p-type point-contact germanium detector at the China Jinping Underground Laboratory,” *Physical Review D*, vol. 90, no. 9, 091701, p. 091701, Nov. 2014. DOI: [10.1103/PhysRevD.90.091701](https://doi.org/10.1103/PhysRevD.90.091701). arXiv: [1404.4946 \[hep-ex\]](https://arxiv.org/abs/1404.4946).
 - [107] Z. Ahmed *et al.*, “Search for annual modulation in low-energy CDMS-II data,” *ArXiv e-prints*, Mar. 2012. arXiv: [1203.1309 \[astro-ph.CO\]](https://arxiv.org/abs/1203.1309).
 - [108] R. Agnese *et al.*, “Improved WIMP-search reach of the CDMS II germanium data,” *Physical Review D*, vol. 92, no. 7, 072003, p. 072003, Oct. 2015. DOI: [10.1103/PhysRevD.92.072003](https://doi.org/10.1103/PhysRevD.92.072003). arXiv: [1504.05871 \[hep-ex\]](https://arxiv.org/abs/1504.05871).
 - [109] R. Agnese *et al.*, “Silicon detector dark matter results from the final exposure of cdms ii,” *Physical Review Letters*, vol. 111, p. 251301, 25 2013. DOI: [10.1103/PhysRevLett.111.251301](https://doi.org/10.1103/PhysRevLett.111.251301).
 - [110] E. Armengaud *et al.*, “Constraints on low-mass WIMPs from the EDELWEISS-III dark matter search,” *JCAP*, vol. 5, 019, p. 019, May 2016. DOI: [10.1088/1475-7516/2016/05/019](https://doi.org/10.1088/1475-7516/2016/05/019). arXiv: [1603.05120](https://arxiv.org/abs/1603.05120).
 - [111] G. Angloher *et al.*, “Results from 730 kg days of the CRESST-II Dark Matter search,” *The European Physical Journal C*, vol. 72, 1971, p. 1971, Apr. 2012. DOI: [10.1140/epjc/s10052-012-1971-8](https://doi.org/10.1140/epjc/s10052-012-1971-8). arXiv: [1109.0702](https://arxiv.org/abs/1109.0702).
 - [112] R. Strauss *et al.*, “A detector module with highly efficient surface-alpha event rejection operated in CRESST-II Phase 2,” *The European Physical Journal C*, vol. 75, 352, p. 352, Aug. 2015. DOI: [10.1140/epjc/s10052-015-3572-9](https://doi.org/10.1140/epjc/s10052-015-3572-9). arXiv: [1410.1753 \[physics.ins-det\]](https://arxiv.org/abs/1410.1753).
 - [113] W. H. Lippincott, K. J. Coakley, D. Gastler, E. Kearns, D. N. McKinsey, and J. A. Nikkel, “Scintillation yield and time dependence from electronic and nuclear recoils in liquid neon,” *Physical Review C*, vol. 86, no. 1, 015807, p. 015807, Jul. 2012. DOI: [10.1103/PhysRevC.86.015807](https://doi.org/10.1103/PhysRevC.86.015807). arXiv: [1111.3260 \[nucl-ex\]](https://arxiv.org/abs/1111.3260).
 - [114] K. a. Rielage, “Update on the MiniCLEAN Dark Matter Experiment,” *Physics Procedia*, vol. 61, pp. 144–152, 2015. DOI: [10.1016/j.phpro.2014.12.024](https://doi.org/10.1016/j.phpro.2014.12.024). arXiv: [1403.4842 \[physics.ins-det\]](https://arxiv.org/abs/1403.4842).

BIBLIOGRAPHY

- [115] P. Cushman *et al.*, “Snowmass CF1 Summary: WIMP Dark Matter Direct Detection,” *arXiv e-prints*, Oct. 2013. arXiv: [1310.8327 \[hep-ex\]](#).
- [116] A. Badertscher *et al.*, “ArDM: first results from underground commissioning,” *Journal of Instrumentation*, vol. 8, C09005, p. C09005, Sep. 2013. DOI: [10.1088/1748-0221/8/09/C09005](#). arXiv: [1309.3992 \[physics.ins-det\]](#).
- [117] P. Agnes *et al.*, “DarkSide-50 532-day Dark Matter Search with Low-Radioactivity Argon,” *arXiv e-prints*, Feb. 2018. arXiv: [1802.07198](#).
- [118] ——, “Low-mass Dark Matter Search with the DarkSide-50 Experiment,” *arXiv e-prints*, Feb. 2018. arXiv: [1802.06994 \[astro-ph.HE\]](#).
- [119] C. E. Aalseth *et al.*, “DarkSide-20k: A 20 tonne two-phase LAr TPC for direct dark matter detection at LNGS,” *The European Physical Journal Plus*, vol. 133, 131, p. 131, Mar. 2018. DOI: [10.1140/epjp/i2018-11973-4](#). arXiv: [1707.08145 \[physics.ins-det\]](#).
- [120] D. S. Akerib *et al.*, “Results from a search for dark matter in the complete lux exposure,” *Physical Review Letters*, vol. 118, p. 021303, 2 2017. DOI: [10.1103/PhysRevLett.118.021303](#).
- [121] X. Cui *et al.*, “Dark Matter Results From 54-Ton-Day Exposure of PandaX-II Experiment,” *Physical Review Letters*, vol. 119, p. 181302, 18 Oct. 2017. DOI: [10.1103/PhysRevLett.119.181302](#). arXiv: [1708.06917](#).
- [122] XMASS Collaboration, “A direct dark matter search in XMASS-I,” *arXiv e-prints*, Apr. 2018. arXiv: [1804.02180](#).
- [123] E. Aprile *et al.*, “Dark Matter Search Results from a One Tonne×Year Exposure of XENON1T,” *arXiv e-prints*, May 2018. arXiv: [1805.12562](#).
- [124] C. Savage, G. Gelmini, P. Gondolo, and K. Freese, “Compatibility of DAMA/LIBRA dark matter detection with other searches,” *JCAP*, vol. 4, 010, p. 010, Apr. 2009. DOI: [10.1088/1475-7516/2009/04/010](#). arXiv: [0808.3607](#).
- [125] R. Agnese *et al.*, “Silicon Detector Dark Matter Results from the Final Exposure of CDMS II,” *Physical Review Letters*, vol. 111, no. 25, 251301, p. 251 301, Dec. 2013. DOI: [10.1103/PhysRevLett.111.251301](#).
- [126] P.-A. Amaudruz *et al.*, “First Results from the DEAP-3600 Dark Matter Search with Argon at SNOLAB,” *Physical Review Letters*, vol. 121, no. 7, 071801, p. 071 801, Aug. 2018. DOI: [10.1103/PhysRevLett.121.071801](#).

- [127] R. Agnese *et al.*, “Results from the Super Cryogenic Dark Matter Search Experiment at Soudan,” *Physical Review Letters*, vol. 120, no. 6, 061802, p. 061802, Feb. 2018. DOI: [10.1103/PhysRevLett.120.061802](https://doi.org/10.1103/PhysRevLett.120.061802).
- [128] Q. Arnaud *et al.*, “First results from the NEWS-G direct dark matter search experiment at the LSM,” *Astroparticle Physics*, vol. 97, pp. 54–62, Jan. 2018. DOI: [10.1016/j.astropartphys.2017.10.009](https://doi.org/10.1016/j.astropartphys.2017.10.009). arXiv: [1706.04934 \[astro-ph.IM\]](https://arxiv.org/abs/1706.04934).
- [129] G. Angloher *et al.*, “Results on light dark matter particles with a low-threshold CRESST-II detector,” *The European Physical Journal C*, vol. 76, 25, p. 25, Jan. 2016. DOI: [10.1140/epjc/s10052-016-3877-3](https://doi.org/10.1140/epjc/s10052-016-3877-3). arXiv: [1509.01515](https://arxiv.org/abs/1509.01515).
- [130] R. Agnese *et al.*, “New Results from the Search for Low-Mass Weakly Interacting Massive Particles with the CDMS Low Ionization Threshold Experiment,” *Physical Review Letters*, vol. 116, no. 7, 071301, p. 071301, Feb. 2016. DOI: [10.1103/PhysRevLett.116.071301](https://doi.org/10.1103/PhysRevLett.116.071301).
- [131] E. Aprile *et al.*, “Dark Matter Results from 225 Live Days of XENON100 Data,” *Physical Review Letters*, vol. 109, no. 18, 181301, p. 181301, Nov. 2012. DOI: [10.1103/PhysRevLett.109.181301](https://doi.org/10.1103/PhysRevLett.109.181301). arXiv: [1207.5988 \[astro-ph.CO\]](https://arxiv.org/abs/1207.5988).
- [132] ——, “First Dark Matter Search Results from the XENON1T Experiment,” *Physical Review Letters*, vol. 119, no. 18, 181301, p. 181301, Nov. 2017. DOI: [10.1103/PhysRevLett.119.181301](https://doi.org/10.1103/PhysRevLett.119.181301). arXiv: [1705.06655](https://arxiv.org/abs/1705.06655).
- [133] E. A. Bagnaschi *et al.*, “Supersymmetric dark matter after LHC run 1,” *The European Physical Journal C*, vol. 75, 500, p. 500, Oct. 2015. DOI: [10.1140/epjc/s10052-015-3718-9](https://doi.org/10.1140/epjc/s10052-015-3718-9). arXiv: [1508.01173 \[hep-ph\]](https://arxiv.org/abs/1508.01173).
- [134] E. Aprile and T. Doke, “Liquid xenon detectors for particle physics and astrophysics,” *Review of Modern Physics*, vol. 82, pp. 2053–2097, Jul. 2010. DOI: [10.1103/RevModPhys.82.2053](https://doi.org/10.1103/RevModPhys.82.2053). arXiv: [0910.4956 \[physics.ins-det\]](https://arxiv.org/abs/0910.4956).
- [135] L. Baudis, “WIMP dark matter direct-detection searches in noble gases,” *Physics of the Dark Universe*, vol. 4, pp. 50–59, Sep. 2014. DOI: [10.1016/j.dark.2014.07.001](https://doi.org/10.1016/j.dark.2014.07.001). arXiv: [1408.4371 \[astro-ph.IM\]](https://arxiv.org/abs/1408.4371).
- [136] N. Barros, J. Thurn, and K. Zuber, “Double beta decay searches of ^{134}Xe , ^{126}Xe and ^{124}Xe with large scale Xe detectors,” *Journal of Physics G*, vol. 41, no. 11, 115105, p. 115105, Nov. 2014. DOI: [10.1088/0954-3899/41/11/115105](https://doi.org/10.1088/0954-3899/41/11/115105). arXiv: [1409.8308 \[nucl-ex\]](https://arxiv.org/abs/1409.8308).
- [137] S. Singh, R. Chandra, P. K. Rath, P. K. Raina, and J. G. Hirsch, “Nuclear deformation and the two-neutrino double- β decay in $^{124,126}\text{Xe}$,

BIBLIOGRAPHY

- $^{128,130}\text{Te}$, $^{130,132}\text{Ba}$ and ^{150}Nd isotopes,” *The European Physical Journal A*, vol. 33, pp. 375–388, Sep. 2007. DOI: [10.1140/epja/i2007-10481-7](https://doi.org/10.1140/epja/i2007-10481-7). arXiv: [0706.4357 \[nucl-th\]](https://arxiv.org/abs/0706.4357).
- [138] J. Mock *et al.*, “Modeling pulse characteristics in Xenon with NEST,” *Journal of Instrumentation*, vol. 9, T04002, T04002, Apr. 2014. DOI: [10.1088/1748-0221/9/04/T04002](https://doi.org/10.1088/1748-0221/9/04/T04002). arXiv: [1310.1117 \[physics.ins-det\]](https://arxiv.org/abs/1310.1117).
- [139] T. Heindl *et al.*, “Table-top setup for investigating the scintillation properties of liquid argon,” *Journal of Instrumentation*, vol. 6, p. 2011, Feb. 2011. DOI: [10.1088/1748-0221/6/02/P02011](https://doi.org/10.1088/1748-0221/6/02/P02011). arXiv: [1511.07720 \[physics.ins-det\]](https://arxiv.org/abs/1511.07720).
- [140] C. H. Faham, “Prototype, Surface Commissioning and Photomultiplier Tube Characterization for the Large Underground Xenon (LUX) Direct Dark Matter Search Experiment,” PhD thesis, Brown University, May 2014.
- [141] L. S. Miller, S. Howe, and W. E. Spear, “Charge Transport in Solid and Liquid Ar, Kr, and Xe,” *Physical Review*, vol. 166, pp. 871–878, Feb. 1968. DOI: [10.1103/PhysRev.166.871](https://doi.org/10.1103/PhysRev.166.871).
- [142] M. J. Berger, J. S. Coursey, M. A. Zucker, and J. Chang. (2017). ESTAR, PSTAR, and ASTAR: Computer Programs for Calculating Stopping-Power and Range Tables for Electrons, Protons, and Helium Ions (version 1.2.3), [Online]. Available: <https://physics.nist.gov/Star> (visited on 01/16/2018).
- [143] H. A. Bethe, “Nuclear Physics B. Nuclear Dynamics, Theoretical,” *Review of Modern Physics*, vol. 9, pp. 69–244, Apr. 1937. DOI: [10.1103/RevModPhys.9.69](https://doi.org/10.1103/RevModPhys.9.69).
- [144] V. Chepel and H. Araújo, “Liquid noble gas detectors for low energy particle physics,” *Journal of Instrumentation*, vol. 8, R04001, R04001, Apr. 2013. DOI: [10.1088/1748-0221/8/04/R04001](https://doi.org/10.1088/1748-0221/8/04/R04001). arXiv: [1207.2292 \[physics.ins-det\]](https://arxiv.org/abs/1207.2292).
- [145] L. Onsager, “Initial Recombination of Ions,” *Physical Review*, vol. 54, pp. 554–557, 8 1938. DOI: [10.1103/PhysRev.54.554](https://doi.org/10.1103/PhysRev.54.554).
- [146] A. Mozumder, “Free-ion yield and electron-ion recombination rate in liquid xenon,” *Chemical Physics Letters*, vol. 245, pp. 359–363, Nov. 1995. DOI: [10.1016/0009-2614\(95\)01024-4](https://doi.org/10.1016/0009-2614(95)01024-4).
- [147] T. Doke, A. Hitachi, J. Kikuchi, K. Masuda, H. Okada, and E. Shibamura, “Absolute Scintillation Yields in Liquid Argon and Xenon for Various Particles,” *Japanese Journal of Applied Physics*, vol. 41, p. 1538, Mar. 2002. DOI: [10.1143/JJAP.41.1538](https://doi.org/10.1143/JJAP.41.1538).

- [148] J. Thomas and D. A. Imel, “Recombination of electron-ion pairs in liquid argon and liquid xenon,” *Physical Review A*, vol. 36, pp. 614–616, Jul. 1987. DOI: [10.1103/PhysRevA.36.614](https://doi.org/10.1103/PhysRevA.36.614).
- [149] K. Yoshino, U. Sowada, and W. F. Schmidt, “Effect of molecular solutes on the electron drift velocity in liquid Ar, Kr, and Xe,” *Physical Review A*, vol. 14, pp. 438–444, 1 1976. DOI: [10.1103/PhysRevA.14.438](https://doi.org/10.1103/PhysRevA.14.438).
- [150] G. Jaffé, “Zur Theorie der Ionisation in Kolonnen,” *Annalen der Physik*, vol. 347, no. 12, pp. 303–344, 1913, ISSN: 1521-3889. DOI: [10.1002/andp.19133471205](https://doi.org/10.1002/andp.19133471205). [Online]. Available: <http://dx.doi.org/10.1002/andp.19133471205>.
- [151] K. Deiters *et al.*, “Test of a liquid argon multistrip ionization chamber with 8.5μ RMS resolution,” *Nuclear Instruments and Methods*, vol. 180, pp. 45–52, Feb. 1981. DOI: [10.1016/0029-554X\(81\)90008-2](https://doi.org/10.1016/0029-554X(81)90008-2).
- [152] J. B. Birks and F. A. Black, “Letters to the Editor: Deterioration of Anthracene under α -Particle Irradiation,” *Proceedings of the Physical Society A*, vol. 64, pp. 511–512, May 1951. DOI: [10.1088/0370-1298/64/5/112](https://doi.org/10.1088/0370-1298/64/5/112).
- [153] J. Birks, D. Fry, L. Costrell, and K. Kandiah, *The Theory and Practice of Scintillation Counting*. Elsevier, 1964, vol. A volume in International Series of Monographs in Electronics and Instrumentation, ISBN: 978-0-08-010472-0.
- [154] T. Doke *et al.*, “Let dependence of scintillation yields in liquid argon,” *Nuclear Instruments and Methods in Physics Research A*, vol. 269, pp. 291–296, Jun. 1988. DOI: [10.1016/0168-9002\(88\)90892-3](https://doi.org/10.1016/0168-9002(88)90892-3).
- [155] M. Szydagis *et al.*, “NEST: A Comprehensive Model for Scintillation Yield in Liquid Xenon,” *ArXiv e-prints*, Jun. 2011. arXiv: [1106.1613 \[physics.ins-det\]](https://arxiv.org/abs/1106.1613).
- [156] D.-M. Mei, Z.-B. Yin, L. C. Stonehill, and A. Hime, “A model of nuclear recoil scintillation efficiency in noble liquids,” *Astroparticle Physics*, vol. 30, pp. 12–17, Aug. 2008. DOI: [10.1016/j.astropartphys.2008.06.001](https://doi.org/10.1016/j.astropartphys.2008.06.001). arXiv: [0712.2470 \[nucl-ex\]](https://arxiv.org/abs/0712.2470).
- [157] E. Aprile *et al.*, “Exclusion of leptophilic dark matter models using XENON100 electronic recoil data,” *Science*, vol. 349, pp. 851–854, Aug. 2015. DOI: [10.1126/science.aab2069](https://doi.org/10.1126/science.aab2069).
- [158] P. Christillin, “Nuclear Compton scattering,” *Journal of Physics G*, vol. 12, pp. 837–851, Sep. 1986. DOI: [10.1088/0305-4616/12/9/008](https://doi.org/10.1088/0305-4616/12/9/008).

BIBLIOGRAPHY

- [159] J. H. Hubbell, “Electron positron pair production by photons: A historical overview,” *Radiation Physics and Chemistry*, vol. 75, pp. 614–623, Jun. 2006. DOI: [10.1016/j.radphyschem.2005.10.008](https://doi.org/10.1016/j.radphyschem.2005.10.008).
- [160] M. J. Berger *et al.* (2010). XCOM: Photon Cross Sections Database, [Online]. Available: <https://www.nist.gov/pml/xcom-photon-cross-sections-database> (visited on 01/16/2018).
- [161] M. Weber, “Gentle Neutron Signals and Noble Background in the XENON100 Dark Matter Search Experiment,” PhD thesis, 2013.
- [162] E. Aprile *et al.*, “Physics reach of the XENON1T dark matter experiment.,” *JCAP*, vol. 4, 027, p. 027, Apr. 2016. DOI: [10.1088/1475-7516/2016/04/027](https://doi.org/10.1088/1475-7516/2016/04/027). arXiv: [1512.07501 \[physics.ins-det\]](https://arxiv.org/abs/1512.07501).
- [163] R. L. Burman, A. C. Dodd, and P. Plischke, “Neutrino flux calculations for the ISIS spallation neutron facility,” *Nuclear Instruments and Methods in Physics Research A*, vol. 368, pp. 416–424, Jan. 1996. DOI: [10.1016/0168-9002\(95\)00627-3](https://doi.org/10.1016/0168-9002(95)00627-3).
- [164] C. McCabe, “Prospects for dark matter detection with inelastic transitions of xenon,” *JCAP*, vol. 5, 033, p. 033, May 2016. DOI: [10.1088/1475-7516/2016/05/033](https://doi.org/10.1088/1475-7516/2016/05/033). arXiv: [1512.00460 \[hep-ph\]](https://arxiv.org/abs/1512.00460).
- [165] C. E. Dahl, “The physics of background discrimination in liquid xenon, and first results from Xenon10 in the hunt for WIMP dark matter,” English, PhD thesis, 2009, p. 182, ISBN: 9781109255294. [Online]. Available: <http://inspirehep.net/record/1374815/files/E.Dahlthesis.pdf>.
- [166] U. Fano, “Ionization Yield of Radiations. II. The Fluctuations of the Number of Ions,” *Physical Review*, vol. 72, pp. 26–29, Jul. 1947. DOI: [10.1103/PhysRev.72.26](https://doi.org/10.1103/PhysRev.72.26).
- [167] T. Doke, A. Hitachi, S. Kubota, A. Nakamoto, and T. Takahashi, “Estimation of Fano factors in liquid argon, krypton, xenon and xenon-doped liquid argon,” *Nuclear Instruments and Methods*, vol. 134, pp. 353–357, Apr. 1976. DOI: [10.1016/0029-554X\(76\)90292-5](https://doi.org/10.1016/0029-554X(76)90292-5).
- [168] J. Seguinot, J. Tischhauser, and T. Ypsilantis, “Liquid xenon scintillation: photon yield and Fano factor measurements,” *Nuclear Instruments and Methods in Physics Research A*, vol. 354, pp. 280–287, Feb. 1995. DOI: [10.1016/0168-9002\(94\)01236-9](https://doi.org/10.1016/0168-9002(94)01236-9).

- [169] T. Takahashi *et al.*, “Average energy expended per ion pair in liquid xenon,” *Physical Review A*, vol. 12, pp. 1771–1775, Nov. 1975. DOI: [10.1103/PhysRevA.12.1771](https://doi.org/10.1103/PhysRevA.12.1771).
- [170] E. Aprile, K. L. Giboni, P. Majewski, K. Ni, and M. Yamashita, “Observation of anticorrelation between scintillation and ionization for MeV gamma rays in liquid xenon,” *Physical Review B*, vol. 76, p. 014115, 1 2007. DOI: [10.1103/PhysRevB.76.014115](https://doi.org/10.1103/PhysRevB.76.014115).
- [171] J. Lindhard, V. Nielsen, M. Scharff, and P. Thomsen, “Integral equations governing radiation effects (notes on atomic collisions, iii),” *Mat. Fys. Medd. Dan. Vid. Selsk*, vol. Vol: 33: No. 10, 1963.
- [172] P. Sorensen and C. E. Dahl, “Nuclear recoil energy scale in liquid xenon with application to the direct detection of dark matter,” *Physical Review D*, vol. 83, no. 6, 063501, p. 063501, Mar. 2011. DOI: [10.1103/PhysRevD.83.063501](https://doi.org/10.1103/PhysRevD.83.063501). arXiv: [1101.6080 \[astro-ph.IM\]](https://arxiv.org/abs/1101.6080).
- [173] B. Lenardo, K. Kazkaz, A. Manalaysay, J. Mock, M. Szydagis, and M. Tripathi, “A Global Analysis of Light and Charge Yields in Liquid Xenon,” *IEEE Transactions on Nuclear Science*, vol. 62, pp. 3387–3396, Dec. 2015. DOI: [10.1109/TNS.2015.2481322](https://doi.org/10.1109/TNS.2015.2481322). arXiv: [1412.4417 \[astro-ph.IM\]](https://arxiv.org/abs/1412.4417).
- [174] J. Angle *et al.*, “Search for Light Dark Matter in XENON10 Data,” *Physical Review Letters*, vol. 107, no. 5, 051301, p. 051301, Jul. 2011. DOI: [10.1103/PhysRevLett.107.051301](https://doi.org/10.1103/PhysRevLett.107.051301). arXiv: [1104.3088 \[astro-ph.CO\]](https://arxiv.org/abs/1104.3088).
- [175] G. Bakale, U. Sowada, and W. F. Schmidt, “Effect of an electric field on electron attachment to sulfur hexafluoride, nitrous oxide, and molecular oxygen in liquid argon and xenon,” *Journal of Physical Chemistry*, vol. 80, no. 23, pp. 2556–2559, 1976. DOI: [10.1021/j100564a006](https://doi.org/10.1021/j100564a006).
- [176] S. Belogurov *et al.*, “High pressure gas scintillation drift chamber with photomultipliers inside of working medium,” IEEE Nuclear Science Symposium and Medical Imaging Conference Record, 1995.
- [177] CHROMacademy. (), [Online]. Available: <http://www.chromacademy.com/lms/sco736/images> (visited on 01/29/2018).
- [178] C. H. Faham, V. M. Gehman, A. Currie, A. Dobi, P. Sorensen, and R. J. Gaitskell, “Measurements of wavelength-dependent double photoelectron emission from single photons in VUV-sensitive photomultiplier tubes,” *Journal of Instrumentation*, vol. 10, P09010, P09010, Sep. 2015. DOI: [10.1088/1748-0221/2015/9/P09010](https://doi.org/10.1088/1748-0221/2015/9/P09010). arXiv: [1506.08748 \[physics.ins-det\]](https://arxiv.org/abs/1506.08748).

BIBLIOGRAPHY

- [179] K. Lung *et al.*, “Characterization of the Hamamatsu R11410-10 3-in. photomultiplier tube for liquid xenon dark matter direct detection experiments,” *Nuclear Instruments and Methods in Physics Research A*, vol. 696, pp. 32–39, Dec. 2012. DOI: [10.1016/j.nima.2012.08.052](https://doi.org/10.1016/j.nima.2012.08.052). arXiv: [1202.2628 \[physics.ins-det\]](https://arxiv.org/abs/1202.2628).
- [180] F. Neves *et al.*, “Measurement of the absolute reflectance of polytetrafluoroethylene (PTFE) immersed in liquid xenon,” *Journal of Instrumentation*, vol. 12, P01017, Jan. 2017. DOI: [10.1088/1748-0221/12/01/P01017](https://doi.org/10.1088/1748-0221/12/01/P01017). arXiv: [1612.07965 \[physics.ins-det\]](https://arxiv.org/abs/1612.07965).
- [181] I. Israelashvili *et al.*, “A comprehensive simulation study of a Liquid-Xe detector for contraband detection,” *Journal of Instrumentation*, vol. 10, P03030, P03030, Mar. 2015. DOI: [10.1088/1748-0221/10/03/P03030](https://doi.org/10.1088/1748-0221/10/03/P03030). arXiv: [1501.00150 \[physics.ins-det\]](https://arxiv.org/abs/1501.00150).
- [182] R. F. Lang *et al.*, “Characterization of a deuterium-deuterium plasma fusion neutron generator,” *Nuclear Instruments and Methods in Physics Research A*, vol. 879, pp. 31–38, Jan. 2018. DOI: [10.1016/j.nima.2017.10.001](https://doi.org/10.1016/j.nima.2017.10.001). arXiv: [1705.04741 \[physics.ins-det\]](https://arxiv.org/abs/1705.04741).
- [183] E. Aprile *et al.*, “Simultaneous Measurement of Ionization and Scintillation from Nuclear Recoils in Liquid Xenon for a Dark Matter Experiment,” *Physical Review Letters*, vol. 97, no. 8, 081302, p. 081302, Aug. 2006. DOI: [10.1103/PhysRevLett.97.081302](https://doi.org/10.1103/PhysRevLett.97.081302).
- [184] ——, “The XENON1T dark matter experiment,” *The European Physical Journal C*, vol. 77, 881, p. 881, Dec. 2017. DOI: [10.1140/epjc/s10052-017-5326-3](https://doi.org/10.1140/epjc/s10052-017-5326-3). arXiv: [1708.07051 \[astro-ph.IM\]](https://arxiv.org/abs/1708.07051).
- [185] P. Barrow *et al.*, “Qualification tests of the R11410-21 photomultiplier tubes for the XENON1T detector,” *Journal of Instrumentation*, vol. 12, P01024, Jan. 2017. DOI: [10.1088/1748-0221/12/01/P01024](https://doi.org/10.1088/1748-0221/12/01/P01024). arXiv: [1609.01654 \[astro-ph.IM\]](https://arxiv.org/abs/1609.01654).
- [186] E. Aprile *et al.*, “Lowering the radioactivity of the photomultiplier tubes for the XENON1T dark matter experiment,” *The European Physical Journal C*, vol. 75, 546, p. 546, Nov. 2015. DOI: [10.1140/epjc/s10052-015-3657-5](https://doi.org/10.1140/epjc/s10052-015-3657-5). arXiv: [1503.07698 \[astro-ph.IM\]](https://arxiv.org/abs/1503.07698).
- [187] L. Baudis *et al.*, “Performance of the Hamamatsu R11410 photomultiplier tube in cryogenic xenon environments,” *Journal of Instrumentation*, vol. 8, P04026, P04026, Apr. 2013. DOI: [10.1088/1748-0221/8/04/P04026](https://doi.org/10.1088/1748-0221/8/04/P04026). arXiv: [1303.0226 \[astro-ph.IM\]](https://arxiv.org/abs/1303.0226).

- [188] L. W. Goetzke, E. Aprile, M. Anthony, G. Plante, and M. Weber, “Measurement of light and charge yield of low-energy electronic recoils in liquid xenon,” *Physical Review D*, vol. 96, no. 10, 103007, p. 103007, Nov. 2017. DOI: [10.1103/PhysRevD.96.103007](https://doi.org/10.1103/PhysRevD.96.103007). arXiv: [1611.10322 \[astro-ph.IM\]](https://arxiv.org/abs/1611.10322).
- [189] E. Aprile *et al.*, “The XENON100 dark matter experiment,” *Astroparticle Physics*, vol. 35, pp. 573–590, Apr. 2012. DOI: [10.1016/j.astropartphys.2012.01.003](https://doi.org/10.1016/j.astropartphys.2012.01.003). arXiv: [1107.2155 \[astro-ph.IM\]](https://arxiv.org/abs/1107.2155).
- [190] ——, “Material radioassay and selection for the XENON1T dark matter experiment,” *The European Physical Journal C*, vol. 77, 890, p. 890, Dec. 2017. DOI: [10.1140/epjc/s10052-017-5329-0](https://doi.org/10.1140/epjc/s10052-017-5329-0). arXiv: [1705.01828 \[physics.ins-det\]](https://arxiv.org/abs/1705.01828).
- [191] ——, “Performance of a cryogenic system prototype for the XENON1T detector,” *Journal of Instrumentation*, vol. 7, p. 10001, Oct. 2012. DOI: [10.1088/1748-0221/7/10/P10001](https://doi.org/10.1088/1748-0221/7/10/P10001). arXiv: [1208.2001 \[physics.ins-det\]](https://arxiv.org/abs/1208.2001).
- [192] ——, “Removing krypton from xenon by cryogenic distillation to the ppq level,” *The European Physical Journal C*, vol. 77, 275, p. 275, May 2017. DOI: [10.1140/epjc/s10052-017-4757-1](https://doi.org/10.1140/epjc/s10052-017-4757-1).
- [193] S. Lindemann and H. Simgen, “Krypton assay in xenon at the ppq level using a gas chromatographic system and mass spectrometer,” *The European Physical Journal C*, vol. 74, 2746, p. 2746, Feb. 2014. DOI: [10.1140/epjc/s10052-014-2746-1](https://doi.org/10.1140/epjc/s10052-014-2746-1). arXiv: [1308.4806 \[physics.ins-det\]](https://arxiv.org/abs/1308.4806).
- [194] S. Bruenner, D. Cichon, S. Lindemann, T. M. Undagoitia, and H. Simgen, “Radon depletion in xenon boil-off gas,” *The European Physical Journal C*, vol. 77, 143, p. 143, Mar. 2017. DOI: [10.1140/epjc/s10052-017-4676-1](https://doi.org/10.1140/epjc/s10052-017-4676-1). arXiv: [1611.03737 \[physics.ins-det\]](https://arxiv.org/abs/1611.03737).
- [195] E. Aprile *et al.*, “Online ^{222}Rn removal by cryogenic distillation in the XENON100 experiment,” *The European Physical Journal C*, vol. 77, 358, p. 358, Jun. 2017. DOI: [10.1140/epjc/s10052-017-4902-x](https://doi.org/10.1140/epjc/s10052-017-4902-x).
- [196] C. Geis, C. Grignon, U. Oberlack, D. Ramírez García, and Q. Weitzel, “Optical response of highly reflective film used in the water Cherenkov muon veto of the XENON1T dark matter experiment,” *Journal of Instrumentation*, vol. 12, P06017, Jun. 2017. DOI: [10.1088/1748-0221/12/06/P06017](https://doi.org/10.1088/1748-0221/12/06/P06017). arXiv: [1706.03687 \[physics.ins-det\]](https://arxiv.org/abs/1706.03687).

BIBLIOGRAPHY

- [197] D. S. Akerib *et al.*, “Tritium calibration of the LUX dark matter experiment,” *Physical Review D*, vol. 93, no. 7, 072009, p. 072 009, Apr. 2016. DOI: [10.1103/PhysRevD.93.072009](https://doi.org/10.1103/PhysRevD.93.072009).
- [198] E. Aprile *et al.*, “Signal yields of keV electronic recoils and their discrimination from nuclear recoils in liquid xenon,” *Physical Review D*, vol. 97, no. 9, 092007, p. 092 007, May 2018. DOI: [10.1103/PhysRevD.97.092007](https://doi.org/10.1103/PhysRevD.97.092007). arXiv: [1709.10149 \[astro-ph.IM\]](https://arxiv.org/abs/1709.10149).
- [199] ——, “First Dark Matter Results from the XENON100 Experiment,” *Physical Review Letters*, vol. 105, no. 13, 131302, p. 131 302, Sep. 2010. DOI: [10.1103/PhysRevLett.105.131302](https://doi.org/10.1103/PhysRevLett.105.131302). arXiv: [1005.0380 \[astro-ph.CO\]](https://arxiv.org/abs/1005.0380).
- [200] R. Saldanha, L. Grandi, Y. Guardincerri, and T. Wester, “Model independent approach to the single photoelectron calibration of photomultiplier tubes,” *Nuclear Instruments and Methods in Physics Research A*, vol. 863, pp. 35–46, Aug. 2017. DOI: [10.1016/j.nima.2017.02.086](https://doi.org/10.1016/j.nima.2017.02.086). arXiv: [1602.03150 \[physics.ins-det\]](https://arxiv.org/abs/1602.03150).
- [201] M. Anthony, E. Aprile, L. Grandi, Q. Lin, and R. Saldanha, “Characterization of photomultiplier tubes with a realistic model through GPU-boosted simulation,” *Journal of Instrumentation*, vol. 13, T02011, Feb. 2018. DOI: [10.1088/1748-0221/13/02/T02011](https://doi.org/10.1088/1748-0221/13/02/T02011). arXiv: [1710.00219 \[astro-ph.IM\]](https://arxiv.org/abs/1710.00219).
- [202] J. B. Albert *et al.*, “Search for Neutrinoless Double-Beta Decay with the Upgraded EXO-200 Detector,” *Physical Review Letters*, vol. 120, no. 7, 072701, p. 072 701, Feb. 2018. DOI: [10.1103/PhysRevLett.120.072701](https://doi.org/10.1103/PhysRevLett.120.072701). arXiv: [1707.08707 \[hep-ex\]](https://arxiv.org/abs/1707.08707).
- [203] X. Ji, “Status of the PandaX Experiment at China Jinping Underground Lab,” UCLA Dark Matter 2016, 2016, [Online]. Available: <https://conferences.pa.ucla.edu/dm16/talks/xiangdongji.pdf>.
- [204] D. S. Akerib *et al.*, “Signal yields, energy resolution, and recombination fluctuations in liquid xenon,” *Physical Review D*, vol. 95, no. 1, 012008, p. 012 008, Jan. 2017. DOI: [10.1103/PhysRevD.95.012008](https://doi.org/10.1103/PhysRevD.95.012008). arXiv: [1610.02076 \[physics.ins-det\]](https://arxiv.org/abs/1610.02076).
- [205] X. Du, K. Bailey, Z.-T. Lu, P. Mueller, T. P. O’Connor, and L. Young, “An atom trap system for practical ^{81}Kr dating,” *Review of Scientific Instruments*, vol. 75, pp. 3224–3232, Oct. 2004. DOI: [10.1063/1.1790562](https://doi.org/10.1063/1.1790562).
- [206] J. B. Albert *et al.*, “Improved measurement of the $2\nu\beta\beta$ half-life of ^{136}Xe with the EXO-200 detector,” *Physical Review C*, vol. 89, no. 1,

- 015502, p. 015 502, Jan. 2014. DOI: [10.1103/PhysRevC.89.015502](https://doi.org/10.1103/PhysRevC.89.015502). arXiv: [1306.6106 \[nucl-ex\]](https://arxiv.org/abs/1306.6106).
- [207] D.-M. Mei and A. Hime, “Muon-induced background study for underground laboratories,” *Physical Review D*, vol. 73, no. 5, 053004, p. 053 004, Mar. 2006. DOI: [10.1103/PhysRevD.73.053004](https://doi.org/10.1103/PhysRevD.73.053004).
- [208] Wikimedia Commons. (2017). Decay Chain of Thorium-232, [Online]. Available: https://commons.wikimedia.org/wiki/File:Decay_Chain_of_Thorium-232.svg (visited on 02/26/2018).
- [209] ——, (2017). Decay Chain of Uranium-238, [Online]. Available: https://commons.wikimedia.org/wiki/File:Decay_Chain_of_Uranium-238.svg (visited on 02/26/2018).
- [210] E. Aprile *et al.*, “Limits on Spin-Dependent WIMP-Nucleon Cross Sections from 225 Live Days of XENON100 Data,” *Physical Review Letters*, vol. 111, no. 2, 021301, p. 021 301, Jul. 2013. DOI: [10.1103/PhysRevLett.111.021301](https://doi.org/10.1103/PhysRevLett.111.021301). arXiv: [1301.6620 \[astro-ph.CO\]](https://arxiv.org/abs/1301.6620).
- [211] ——, “Search for bosonic super-WIMP interactions with the XENON100 experiment,” *Physical Review D*, vol. 96, no. 12, 122002, p. 122 002, Dec. 2017. DOI: [10.1103/PhysRevD.96.122002](https://doi.org/10.1103/PhysRevD.96.122002). arXiv: [1709.02222](https://arxiv.org/abs/1709.02222).
- [212] ——, “Search for WIMP inelastic scattering off xenon nuclei with XENON100,” *Physical Review D*, vol. 96, no. 2, 022008, p. 022 008, Jul. 2017. DOI: [10.1103/PhysRevD.96.022008](https://doi.org/10.1103/PhysRevD.96.022008). arXiv: [1705.05830 \[hep-ex\]](https://arxiv.org/abs/1705.05830).
- [213] F. James, “Interpretation of the shape of the likelihood function around its minimum,” *Computer Physics Communications*, vol. 20, no. 1, pp. 29–35, 1980, ISSN: 0010-4655. DOI: [10.1016/0010-4655\(80\)90103-4](https://doi.org/10.1016/0010-4655(80)90103-4).
- [214] M. S. Bartlett, “Approximate Confidence Intervals: More Than One Unknown Parameter,” *Biometrika*, vol. 40, no. 3-4, pp. 306–317, 1953. DOI: [10.1093/biomet/40.3-4.306](https://doi.org/10.1093/biomet/40.3-4.306).
- [215] N. Priel, L. Rauch, H. Landsman, A. Manfredini, and R. Budnik, “A model independent safeguard against background mismodeling for statistical inference,” *JCAP*, vol. 5, 013, p. 013, May 2017. DOI: [10.1088/1475-7516/2017/05/013](https://doi.org/10.1088/1475-7516/2017/05/013). arXiv: [1610.02643 \[physics.data-an\]](https://arxiv.org/abs/1610.02643).
- [216] G. J. Feldman and R. D. Cousins, “Unified approach to the classical statistical analysis of small signals,” *Phys. Rev. D*, vol. 57, pp. 3873–3889, 7 Apr. 1998. DOI: [10.1103/PhysRevD.57.3873](https://doi.org/10.1103/PhysRevD.57.3873). [Online]. Available: <https://link.aps.org/doi/10.1103/PhysRevD.57.3873>.

BIBLIOGRAPHY

- [217] S. Agostinelli *et al.*, “GEANT4 - a simulation toolkit,” *Nuclear Instruments and Methods in Physics Research A*, vol. 506, pp. 250–303, Jul. 2003. doi: [10.1016/S0168-9002\(03\)01368-8](https://doi.org/10.1016/S0168-9002(03)01368-8).
- [218] D. Foreman-Mackey, D. W. Hogg, D. Lang, and J. Goodman, “emcee: The MCMC Hammer,” *Publication of the Astronomical Society of the Pacific*, vol. 125, p. 306, Mar. 2013. doi: [10.1086/670067](https://doi.org/10.1086/670067). arXiv: [1202.3665 \[astro-ph.IM\]](https://arxiv.org/abs/1202.3665).
- [219] J. Goodman and J. Weare, “Ensemble samplers with affine invariance,” *Communications in Applied Mathematics and Computational Science*, vol. 5, no. 1, 025808, pp. 65–80, Jan. 2010. doi: [10.2140/camcos.2010.5.65](https://doi.org/10.2140/camcos.2010.5.65).
- [220] A. Gelman and D. B. Rubin, “Inference from Iterative Simulation Using Multiple Sequences,” *Statistical Science*, vol. 7, no. 4, pp. 457–472, Nov. 1992.
- [221] D. S. Akerib *et al.*, “Ultra-Low Energy Calibration of LUX Detector using ^{127}Xe Electron Capture,” *arXiv e-prints*, Sep. 2017. arXiv: [1709.00800 \[physics.ins-det\]](https://arxiv.org/abs/1709.00800).
- [222] E. M. Boulton *et al.*, “Calibration of a two-phase xenon time projection chamber with a ^{37}Ar source,” *Journal of Instrumentation*, vol. 12, P08004, Aug. 2017. doi: [10.1088/1748-0221/12/08/P08004](https://doi.org/10.1088/1748-0221/12/08/P08004). arXiv: [1705.08958 \[physics.ins-det\]](https://arxiv.org/abs/1705.08958).
- [223] E. Aprile *et al.*, “Scintillation response of liquid xenon to low energy nuclear recoils,” *Physical Review D*, vol. 72, no. 7, 072006, p. 072 006, Oct. 2005. doi: [10.1103/PhysRevD.72.072006](https://doi.org/10.1103/PhysRevD.72.072006).
- [224] ——, “New measurement of the relative scintillation efficiency of xenon nuclear recoils below 10 keV,” *Physical Review C*, vol. 79, no. 4, 045807, p. 045 807, Apr. 2009. doi: [10.1103/PhysRevC.79.045807](https://doi.org/10.1103/PhysRevC.79.045807). arXiv: [0810.0274](https://arxiv.org/abs/0810.0274).
- [225] G. Plante *et al.*, “New measurement of the scintillation efficiency of low-energy nuclear recoils in liquid xenon,” *Physical Review C*, vol. 84, no. 4, 045805, p. 045 805, Oct. 2011. doi: [10.1103/PhysRevC.84.045805](https://doi.org/10.1103/PhysRevC.84.045805). arXiv: [1104.2587 \[nucl-ex\]](https://arxiv.org/abs/1104.2587).
- [226] A. Manzur, A. Curioni, L. Kastens, D. N. McKinsey, K. Ni, and T. Wongjirad, “Scintillation efficiency and ionization yield of liquid xenon for monoenergetic nuclear recoils down to 4 keV,” *Physical Review C*, vol. 81, no. 2, 025808, p. 025 808, Feb. 2010. doi: [10.1103/PhysRevC.81.025808](https://doi.org/10.1103/PhysRevC.81.025808). arXiv: [0909.1063 \[physics.ins-det\]](https://arxiv.org/abs/0909.1063).

- [227] E. Aprile *et al.*, “Response of the XENON100 dark matter detector to nuclear recoils,” *Physical Review D*, vol. 88, no. 1, 012006, p. 012 006, Jul. 2013. DOI: [10.1103/PhysRevD.88.012006](https://doi.org/10.1103/PhysRevD.88.012006). arXiv: [1304.1427 \[astro-ph.IM\]](https://arxiv.org/abs/1304.1427).
- [228] P. Sorensen *et al.*, “The scintillation and ionization yield of liquid xenon for nuclear recoils,” *Nuclear Instruments and Methods in Physics Research A*, vol. 601, pp. 339–346, Apr. 2009. DOI: [10.1016/j.nima.2008.12.197](https://doi.org/10.1016/j.nima.2008.12.197). arXiv: [0807.0459](https://arxiv.org/abs/0807.0459).
- [229] D. S. Akerib *et al.*, “Low-energy (0.7–74 keV) nuclear recoil calibration of the LUX dark matter experiment using D-D neutron scattering kinematics,” *arXiv e-prints*, Aug. 2016. arXiv: [1608.05381 \[physics.ins-det\]](https://arxiv.org/abs/1608.05381).
- [230] K. Watanabe, E. C. Y. Inn, and M. Zelikoff, “Absorption Coefficients of Oxygen in the Vacuum Ultraviolet,” *Journal of Chemical Physics*, vol. 21, no. 6, pp. 1026–1030, 1953. DOI: [10.1063/1.1699104](https://doi.org/10.1063/1.1699104).
- [231] K. Watanabe and M. Zelikoff, “Absorption coefficients of water vapor in the vacuum ultraviolet,” *Journal of the Optical Society of America*, vol. 43, no. 9, pp. 753–755, 1953. DOI: [10.1364/JOSA.43.000753](https://doi.org/10.1364/JOSA.43.000753).
- [232] A. Baldini *et al.*, “Absorption of scintillation light in a 100 l liquid xenon γ -ray detector and expected detector performance,” *Nuclear Instruments and Methods in Physics Research A*, vol. 545, pp. 753–764, Jun. 2005. DOI: [10.1016/j.nima.2005.02.029](https://doi.org/10.1016/j.nima.2005.02.029).
- [233] K. Ozone, “Liquid Xenon Scintillation Detector for the New $\mu \rightarrow e\gamma$ Search Experiment,” English, PhD thesis, Mar. 2005. [Online]. Available: <http://meg.icepp.s.u-tokyo.ac.jp/docs/theses/ozoned.pdf>.
- [234] K. Yoshino, J. R. Esmond, W. H. Parkinson, K. Ito, and T. Matsui, “Absorption cross section measurements of water vapor in the wavelength region 120 to 188 nm,” *Chemical Physics*, vol. 211, pp. 387–391, Nov. 1996. DOI: [10.1016/0301-0104\(96\)00210-8](https://doi.org/10.1016/0301-0104(96)00210-8).
- [235] W. Tauchert, H. Jungblut, and W. F. Schmidt, “Photoelectric determination of V_0 values and electron ranges in some cryogenic liquids,” *Canadian Journal of Chemistry*, vol. 55, no. 11, pp. 1860–1866, 1977. DOI: [10.1139/v77-260](https://doi.org/10.1139/v77-260).
- [236] E. M. Gushchin, K. A., and O. I. M., “Electron dynamics in condensed argon and xenon,” *JETP*, vol. 82, pp. 1114–1125, Apr. 1982.
- [237] S. S.-S. Huang and G. R. Freeman, “Electron mobilities in gaseous, critical, and liquid xenon: Density, electric field, and temperature effects: Quasilocal-

BIBLIOGRAPHY

- ization,” *Journal of Chemical Physics*, vol. 68, pp. 1355–1362, Feb. 1978. DOI: [10.1063/1.435954](https://doi.org/10.1063/1.435954).
- [238] E. B. Wagner, F. J. Davis, and G. S. Hurst, “Time-of-Flight Investigations of Electron Transport in Some Atomic and Molecular Gases,” *Journal of Chemical Physics*, vol. 47, pp. 3138–3147, Nov. 1967. DOI: [10.1063/1.1712365](https://doi.org/10.1063/1.1712365).
- [239] J. L. Pack, R. E. Voshall, A. V. Phelps, and L. E. Kline, “Longitudinal electron diffusion coefficients in gases: Noble gases,” *Journal of Applied Physics*, vol. 71, pp. 5363–5371, Jun. 1992. DOI: [10.1063/1.350555](https://doi.org/10.1063/1.350555).
- [240] V. M. Atrazhev, A. V. Berezhnov, D. O. Dunikov, I. V. Chernysheva, V. V. Dmitrenko, and G. Kapralova, “Electron transport coefficients in liquid xenon,” in *IEEE International Conference on Dielectric Liquids, 2005. ICDL 2005.*, Jun. 2005, pp. 329–332. DOI: [10.1109/ICDL.2005.1490092](https://doi.org/10.1109/ICDL.2005.1490092).
- [241] O. Hilt and W. F. Schmidt, “Positive-hole mobility in liquid xenon as a function of temperature,” *Journal of Physics: Condensed Matter*, vol. 6, pp. L735–L738, Nov. 1994. DOI: [10.1088/0953-8984/6/47/003](https://doi.org/10.1088/0953-8984/6/47/003).
- [242] O. Hilt, W. F. Schmidt, and A. G Khrapak, “Ionic mobilities in liquid xenon,” *IEEE Transactions Dielectrics Electrical Insulation*, vol. 1, pp. 648–656, Aug. 1994. DOI: [10.1109/94.311708](https://doi.org/10.1109/94.311708).
- [243] K. Wamba *et al.*, “Mobility of thorium ions in liquid xenon,” *Nuclear Instruments and Methods in Physics Research A*, vol. 555, pp. 205–210, Dec. 2005. DOI: [10.1016/j.nima.2005.09.023](https://doi.org/10.1016/j.nima.2005.09.023).
- [244] A. J. Walters and L. W. Mitchell, “Mobility and lifetime of ^{208}Tl ions in liquid xenon,” *Journal of Physics D*, vol. 36, pp. 1323–1331, Jun. 2003. DOI: [10.1088/0022-3727/36/11/313](https://doi.org/10.1088/0022-3727/36/11/313).
- [245] H. T. Davis, S. A. Rice, and L. Meyer, “On the Kinetic Theory of Dense Fluids. XIII. The Mobility of Negative Ions in Liquid Ar, Kr, Xe,” *Journal of Chemical Physics*, vol. 37, pp. 2470–2472, Nov. 1962. DOI: [10.1063/1.1733029](https://doi.org/10.1063/1.1733029).
- [246] E. Aprile, A. E. Bolotnikov, A. I. Bolozdynya, and T. Doke, *Noble Gas Detectors*. WILEY-VCH Verlag GmbH & Co. KGaA, 2006, ISBN: 978-3-527-40597-8.
- [247] F. Bloch and N. E. Bradbury, “On the Mechanism of Unimolecular Electron Capture,” *Physical Review*, vol. 48, pp. 689–695, Oct. 1935. DOI: [10.1103/PhysRev.48.689](https://doi.org/10.1103/PhysRev.48.689).

- [248] A. Herzenberg, “Attachment of Slow Electrons to Oxygen Molecules,” *Journal of Chemical Physics*, vol. 51, pp. 4942–4950, Dec. 1969. DOI: [10.1063/1.1671887](https://doi.org/10.1063/1.1671887).
- [249] N. L. Aleksandrov, “Three-body electron attachment to $O_2(a^1\Delta_g)$,” *Chemical Physics Letters*, vol. 212, pp. 409–412, Sep. 1993. DOI: [10.1016/0009-2614\(93\)89346-J](https://doi.org/10.1016/0009-2614(93)89346-J).
- [250] ——, “Breakup of $O_2/-$ ions in collisions with molecules,” *High Temperature Science*, vol. 18, pp. 911–917, Mar. 1981.
- [251] N. L. Aleksandrov and E. M. Anokhin, “Low-energy electron attachment and detachment in vibrationally excited oxygen,” *Journal of Physics D*, vol. 42, no. 22, 225210, p. 225 210, Nov. 2009. DOI: [10.1088/0022-3727/42/22/225210](https://doi.org/10.1088/0022-3727/42/22/225210).
- [252] D. S. Akerib *et al.*, “ ^{83m}Kr calibration of the 2013 LUX dark matter search,” *Physical Review D*, vol. 96, no. 11, 112009, p. 112 009, Dec. 2017. DOI: [10.1103/PhysRevD.96.112009](https://doi.org/10.1103/PhysRevD.96.112009).
- [253] R. Knoche, “Signal Corrections and Calibrations in the LUX Dark Matter Detector,” PhD thesis, 2016.
- [254] M. Szydagis, A. Fyhrie, D. Thorngren, and M. Tripathi, “Enhancement of NEST capabilities for simulating low-energy recoils in liquid xenon,” *Journal of Instrumentation*, vol. 8, C10003, p. C10003, Oct. 2013. DOI: [10.1088/1748-0221/8/10/C10003](https://doi.org/10.1088/1748-0221/8/10/C10003). arXiv: [1307.6601 \[physics.ins-det\]](https://arxiv.org/abs/1307.6601).
- [255] E. Aprile *et al.*, “High speed purification of Xenon and implication for ton scale detectors,” in prep.
- [256] J. F. O’Hanlon, *A User’s Guide to Vacuum Technology*, 3rd. Wiley, 2003.
- [257] D. H. Holkeboer, D. W. Jones, F. Pagano, and D. J. Santeler, “Vacuum technology and space simulation,” Aero. Vac. Corp., Troy, NY, Tech. Rep. 19660026839, Jan. 1966, p. 315. [Online]. Available: <https://ntrs.nasa.gov/search.jsp?R=19660026839>.
- [258] D. G. Bills, “Ultimate Pressure Limitations,” *Journal of Vacuum Science and Technology*, vol. 6, p. 166, Jan. 1969. DOI: [10.1116/1.1492650](https://doi.org/10.1116/1.1492650).
- [259] R. Nuvolone, “Technology of low-pressure systems-establishment of optimum conditions to obtain low degassing rates on 316 L stainless steel by heat treatments,” *Journal of Vacuum Science and Technology*, vol. 14, p. 1210, Sep. 1977. DOI: [10.1116/1.569388](https://doi.org/10.1116/1.569388).

BIBLIOGRAPHY

- [260] C. J. F. Ter Braak, “A Markov Chain Monte Carlo version of the genetic algorithm Differential Evolution: easy Bayesian computing for real parameter spaces,” *Statistics and Computing*, vol. 16, no. 3, pp. 239–249, Sep. 2006, ISSN: 1573-1375. DOI: [10.1007/s11222-006-8769-1](https://doi.org/10.1007/s11222-006-8769-1).
- [261] B. Nelson, E. B. Ford, and M. J. Payne, “RUN DMC: An Efficient, Parallel Code for Analyzing Radial Velocity Observations Using N-body Integrations and Differential Evolution Markov Chain Monte Carlo,” *The Astrophysical Journal Supplemental Series*, vol. 210, 11, p. 11, Jan. 2014. DOI: [10.1088/0067-0049/210/1/11](https://doi.org/10.1088/0067-0049/210/1/11). arXiv: [1311.5229 \[astro-ph.EP\]](https://arxiv.org/abs/1311.5229).
- [262] C. J. F. ter Braak and J. A. Vrugt, “Differential Evolution Markov Chain with snooker updater and fewer chains,” *Statistics and Computing*, vol. 18, no. 4, pp. 435–446, Dec. 2008, ISSN: 1573-1375. DOI: [10.1007/s11222-008-9104-9](https://doi.org/10.1007/s11222-008-9104-9).